AIAA JOURNAL
Vol. 40, No. 11, November 2002

Review of State of Art of Smart Structures and Integrated Systems

Inderjit Chopra
University of Maryland, College Park, Maryland 20742

I. Introduction

A SMART structure involves distributed actuators and sensors and one or more microprocessors that analyze the responses from the sensors and use integrated control theory to command the actuators to apply localized strains/displacements to alter system response. A smart structure has the capability to respond to a changing external environment (such as loads or shape change) as well as to a changing internal environment (such as damage or failure). It incorporates smart material actuators that allow the alteration of system characteristics (such as stiffness or damping) as well as of system response (such as strain or shape) in a controlled manner. Thus, a smart structure involves four key elements: actuators, sensors, control strategies, and power conditioning electronics. Many types of actuators and sensors, such as piezoelectric materials, shape memory alloys, electrostrictive materials, magnetostrictive materials, electro- and magnetorheological fluids and fiber optics, are being considered for various applications. These can be integrated with main load-carrying structures by surface bonding or embedding without causing any significant changes in the mass or structural stiffness of the system.

Numerous applications of smart-structures technology to various physical systems are evolving to actively control vibration, noise, aeroelastic stability, damping, shape change, and stress distribution. Applications range from space systems to fixed-wing and rotary-wing aircraft, automotive, civil structures, machine tools, and medical systems. Much of the early development of smart-structures methodology was driven by space applications such as vibration and shape control of large flexible space structures, but now wider applications are envisaged for aeronautical and other systems. Embedded or surface-bonded smart actuators on an airplane wing or a helicopter blade, for example, can induce airfoil twist/camber change that in turn can cause a variation of lift distribution and can help to control static and dynamic aeroelastic problems.

Applications of smart-structures technology to aerospace and other systems are expanding rapidly. Major barriers include low actuator stroke, lack of reliable smart material characteristics database, unavailability of robust distributed adaptive control strategies, and reliable smart systems mathematical modeling and analysis. The objective of this survey is to review the state of the art of smart actuators, sensors, and integrated systems and point out the needs for future research. These research needs are highlighted under each section and then summarized again in the last section. In this paper six different topics are covered: smart material actuators and sensors and piezoelectrics, modeling of beams with induced strain actuation, modeling of plates with induced strain actuation, shape memory alloys, magnetostrictors and electrostrictors, and smart-structures applications. It is an emerging multidisciplinary field, and associated methodology/technology is in its early development (see related books[1–25] and review papers[26–41]).

II. Smart Material Actuators and Sensors and Piezoelectrics

Piezoelectrics are the most popular smart materials. They undergo deformation (strain) when an electric field is applied across them, and conversely produce voltage when strain is applied, and thus can be used both as actuators and sensors. Under an applied field these materials generate a very low strain but cover a wide range of actuation frequency. Piezoelectric materials are relatively linear (at low fields) and bipolar, but exhibit hysteresis. The most widely used piezoceramics (such as lead zirconate titanate) are in the form of thin

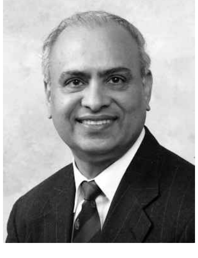

Inderjit Chopra is an Alfred Gessow Professor in Aerospace Engineering and Director of the Alfred Gessow Rotorcraft Center at the University of Maryland. Also, he was the Minta–Martin Research Professor from 1996 to 2000. After receiving his Sc.D. degree from the Massachusetts Institute of Technology in 1977, he joined the NASA Ames/Stanford University Joint Institute of Aeronautics and Acoustics, where he worked for four and half years on the development of aeroelastic analyses and testing of advanced helicopter rotor systems. In 1981, he joined the University Maryland as an Associate Professor, and he got promoted to Full Professor in 1986. He has been working on various fundamental problems related to dynamics of helicopters, including aeromechanics stability, smart structures applications, active vibration control, modeling of composite blades, rotor head health monitoring, aeroelastic optimization, micro air vehicle development, and comprehensive aeromechanics analyses of bearingless, tilt-rotor, servo-flap, teetering, and circulation control rotors. His direct graduate advising resulted in 31 Ph.D. and 55 M.S. degrees. He has been the principal investigator of three major research programs: the Army's University Research Initiative (URI) (1992–1997) on "Smart-Structures Technology: Innovations and Applications to Rotorcraft Systems," the Army's Multidisciplinary University Research Initiative (MURI) (1996–2001) on "Innovative Smart Technologies for Actively Controlled Jet-Smooth Rotorcraft" and Army/NASA's "Rotary-Wing Center of Excellence" (1982–2006). He acted as the Department Chairman from 1988 to 1990. An author of over 130 archival papers, Dr. Chopra has been an Associate Editor of the *Journal of the American Helicopter Society* (1987–1991), *Journal of Aircraft* (1987–), and *Journal of Intelligent Materials and Systems*. (1997–). Also, he has been a member of the editorial advisory board of three journals *VERTICA* (1987–1991), *Smart Materials and Structures* (1994–2000) and *SADHANA* (1991–1995). He was awarded the 1992 UM's Distinguished Research Professorship, 1995 UM's Presidential Award for Outstanding Service to the Schools, 2002 AIAA Structures, Structural Dynamics, and Materials Award, 2002 AHS Grover E. Bell Award, 2001 ASME Adaptive Structures and Material Systems Prize, and 1996 AIAA/ASME Best Paper Award. He is a member of the Army Science Board (1997–). He is a Fellow of the AIAA, a Fellow of the American Helicopter Society, and a Fellow of the Aeronautical Society of India.

Presented at the AIAA/ASME/ASCE/AHS/ASC 42nd Structures, Structural Dynamics, and Materials Conference and Adaptive Structures Forum, 16–19 April 2001; received 18 July 2001; revision received 10 June 2002; accepted for publication 10 June 2002.

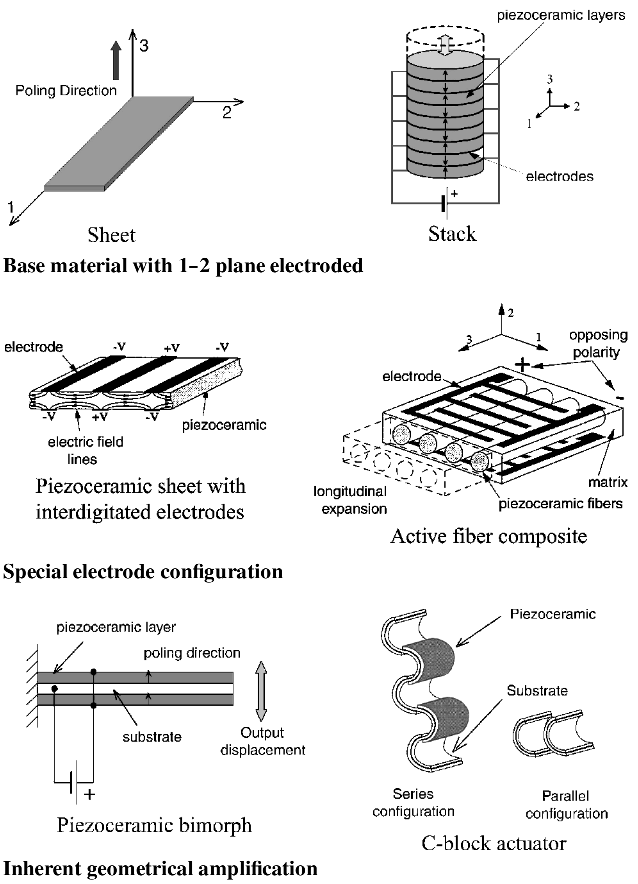

Fig. 1 Different types of actuators.

sheets that can be readily attached or embedded in composite structures or stacked to form discrete piezostack actuators (Fig. 1). These sheets generate isotropic strains on the surface and a non-Poisson strain across the thickness. It is possible however to generate directional in-plane induced strains with piezoceramics using electrode arrangement, specially shaped piezos, bonding arrangement, and embedded fibers (Fig. 1). Piezoelectric and electrostrictive materials are also available in the form of "stacks," where many layers of materials and electrodes are assembled together. These stacks generate large forces but small displacements in the direction normal to the top and bottom surfaces. Bimorphs or bending actuators are also available commercially, where two layers of these materials (piezoceramic) are stacked with a thin shim (typically of brass) between them. If an opposite polarity is applied to two sheets, a bending action is created. Bimorphs cause larger displacement and smaller force as compared to single piezo element.

Among other smart materials, shape memory alloys (SMA) appear attractive as actuators because of the possibility of achieving large excitation forces and displacements. These materials undergo phase transformation at a specific temperature. When plastically deformed at a low temperature, these alloys recover their original undeformed condition if their temperature is raised above the transformation temperature. This process is reversible. A remarkable characteristic of SMA is the large change of modulus of elasticity when heated above phase transition temperature (typically two to four times room temperature value). The most common SMA material is nitinol (nickel titanium alloy), which is available in the form of wires of different diameters. Heating of an SMA can be carried out both internally (electrical resistance) or externally (using coils), but the response is very slow (less than 1 Hz). It is sometime possible to speed up the response through forced convective or conductive cooling of material. Electrostrictive materials are similar to piezoelectric materials, with about the same strain capability. However, they are very sensitive to temperature, have a monopolar, nonlinear relation between the applied field and induced strain, and exhibit negligible hysteresis. Magnetostrictive materials such as Terfenol-D elongate when exposed to a magnetic field. These materials are monopolar and nonlinear and exhibit hysteresis. These materials generate low strains and moderate forces over a wide frequency range. Because of coil and magnetic return path, these actuators are often bulky. Electrorheological (ER) fluid consists of suspensions of fine dielectric particles in an insulating fluid that exhibits controlled rheological behavior in the presence of large applied electric fields (up to 1–4 kV/mm). Application of an electric field results in a significant change of shear loss factor that helps alter damping of the system. Magnetorheological (MR) fluids consist of suspensions of ferrous particles in fluid and exhibit change in shear loss factor caused by magnetic fields (low fields but moderately large currents). MR fluids, like ER fluids, are primarily envisaged to augment damping in a system. Fiber optics is becoming popular as sensors because they can be easily embedded in composite structures with little effect on structural integrity and also have the potential of multiplexing. Discussion on ER and MR fluids and fiber optics is not covered in this paper.

Smart structures are becoming feasible because of the 1) availability of smart materials commercially, 2) ease of embedding devices in laminated structures, 3) exploitation of material couplings such as between mechanical and electrical properties, 4) potential of a substantial increase in performance at a small price (say weight penalty), and 5) advances in microelectronics, information processing, and sensor technology. Key elements in the application of smart structures technology to a system are actuators, sensors, control methodology, and hardware (computer and power electronics).

A. Smart Actuators

Typical actuators consist of piezoceramics, magnetostrictives, electrostrictives, and shape memory alloys. These normally convert electric inputs into actuation strain/displacement that is transmitted to the host structure affecting its mechanical state. Piezoelectrics and electrostrictors are available as ceramics, whereas magnetostrictors and shape memory alloys are available as metal alloys. Piezoelectrics are also available in polymer form as thin soft film. Important performance parameters of actuators include maximum stroke or strain, maximum block force, stiffness, and bandwidth. Somewhat less important parameters include linearity, sensitivity to temperature, brittleness and fracture toughness (fatigue life), repeatability and reliability, weight density, compactness, heat generation, field requirement, and efficiency. The induced strain is often treated like thermal strain. The total strain in the actuator is assumed to be the sum of the mechanical strain caused by the stress plus the induced strain caused by the electric field. The strain in the host structure is obtained by establishing the displacement compatibility between the host material and the actuator. In a piezoelectric material, when an electric field is applied, the dipoles of the material try to orient themselves along the field causing strain in the material. This relation of strain vs voltage is linear in the first order. In an electrostrictive material there is an interaction between the electric field and electric dipoles that is inherently nonlinear. The magnetostrictive response is based on the coupling of magnetic field and magnetic dipoles in the material, a nonlinear effect. Shape memory is a result of phase transformation as a result of temperature change of the material (caused by an thermal field). Phase transformation is very much a nonlinear phenomenon.

A common piezoceramic material is lead zirconate titanate (PZT), and its maximum actuation strain is about 1000 microstrain. Polyvinylidene fluoride (PVDF) is a polymer piezoelectric film, and its maximum actuation strain is about 700 microstrain. A common ceramic electrostrictive material is lead magnesium niobate (PMN), and its maximum actuation strain is about 1000 microstrain. PZT and PMN are available in the form of thin sheets, which can be either bonded or embedded in a structure.

The PZTs require initial polarization (with high electric field), whereas no such polarization is needed for PMNs. Terfenol, a rare Earth magnet-like material, can create a maximum actuation strain of about 2000 microstrain. It needs a large magnetic field to cause this actuation strain. Nitinol (nickel titanium alloy) normally available in the form of wires can create free strain from 20,000 to 60,000 microstrain (2–6%). Table 1 shows comparison of characteristics for

Table 1 Comparison of actuators

Actuators	PZT-5H	PVDF	PMN	Terfernol DZ	Nitinol
Actuation mechanism	Piezoceramic	Piezofilm	Electrostrictive	Magnetostrictive	Shape memory alloy
Free strain Λ, μ strain	1,000	700	1,000	2,000	60,000
Modulus E 10^6 psi	10	0.3	17	7	4 for (martensite) 13 for (austenite)
$\varepsilon_{\max}$ for aluminum beam $t_b/t_c = 10$	350	10	500	580	8,500
Band width	High	High	High	Moderate	Low
Strain-voltage linearity	First-order linear	First-order linear	Nonlinear	Nonlinear	Nonlinear

Table 2 Comparison of strain sensors

Sensor	Resistance gauge 10-V excitation	Semiconductor gauge 10-V excitation	Fiber optics 0.04-in. interferometer gauge length	Piezofilm 0.001-in. thickness	Piezoceramics 0.001-in. thickness
Sensitivity	30 V/ε	1000 V/ε	10^6 deg/ε	10^4 V/ε	2×10^4 V/ε
Localization (inches)	0.008	0.03	0.04	<0.04	<0.04
Bandwidth	0 Hz acoustic	0 Hz acoustic	0 Hz acoustic	0.1 Hz GHZ	0.1 Hz GHZ

different smart actuators. Note t_b is beam thickness, and t_c is actuator thickness. Giurgiutiu et al.[42] compared the characteristics of various commercially available piezoelectric, electrostrictive, and magnetostrictive actuators. The comparison was carried out in terms of output energy density. Typically, the energy density per unit mass was found to be in the range of 0.233–0.900 J/kg. There is a wide variation of performance of actuators from vendor to vendor. Near[43] provided a good overview on the piezoelectric actuator technology.

B. Sensors

Typical sensors consist of strain gauges, accelerometers, fiber optics, piezoelectric films, and piezoceramics. Sensors convert strain or displacement (or their time derivatives) into an electric field. Piezoelectric strain sensors are generally made of polymers such as PVDF and are very flexible (low stiffness). They can be easily formed into very thin sheets (films) and adhered to any surface. Key factors for sensors are their sensitivity to strain or displacement, bandwidth, and size. Other less important factors include temperature sensitivity, linearity, hysteresis, repeatability, electromagnetic compatibility, embeddibility, and associated electronics (size and power requirement). Typically, the sensitivity for resistor gauge is 30 V per strain, for semiconductor gauge is 10^3 V per strain, and for piezoelectric and piezoceramic gauges is 10^4 V per strain. The sensitivity of fiber optics sensors is defined differently and is about 10^6 deg per strain. Associated electronics weigh against fiber optics sensors. Discrete shaped sensors that apply weighting to sensors' output can help increase sensitivity for a specific application. For example, a modal sensor can magnify the strain of a particular mode. Table 2 shows a comparison of characteristics of different sensors.

C. Piezoelectric Actuators

Piezoelectricity means pressure electricity and is a property of certain crystalline materials such as quartz, Rochelle salt, tourmaline, and barium titanate that develop electricity when pressure is applied. This is called the direct effect. Pierre and Jacques Curie discovered piezoelectricity in the 1880s. Soon after this, the converse effect was discovered, that is, these crystals undergo deformation when an electric field is applied. After its discovery, it took several decades before this phenomenon could be used in commercial applications. The first application was perhaps during the World War II in the 1940s as an ultrasonic detector for submarines. With the discovery of piezoceramics, the domain of applications has expanded considerably.

Piezoceramics are polycrystalline in nature and do not have piezoelectric characteristics in their original state. Piezoelectric effects are induced in these materials through simple poling (application of high dc electric field results in polarization). The most commonly used piezoceramic is PZT. These are solid solutions of lead zirconate and lead titanate, often doped with other elements to obtain specific properties. Mixing a powder of lead, zirconium, and titanium oxide and then heating the mixture to around 800–1000°C manufacture these ceramics. It transforms to perovskite PZT powder, which is mixed with binder and sintered into desired shapes. During the cooling process, the material undergoes a paraelectric to ferroelectric phase transformation. An unpoled ceramic consists of many randomly oriented domains with no net polarization.

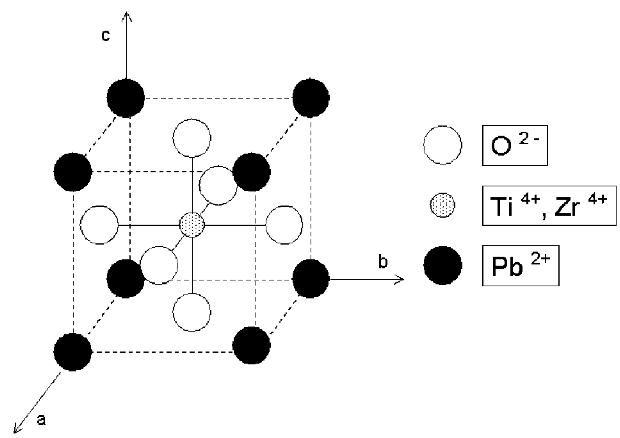

Fig. 2 Typical PZT crystal cell.

Application of high electric field aligns most of the tetragonal domains in such a way that the polar axes (c axes) of unit cells are oriented mostly parallel to the applied field (Fig. 2). This process is called poling, and it imparts a permanent net polarization to the ceramic (analogous to magnetization of a ferrous material with a permanent magnet). This reorientation of domains also causes a permanent mechanical deformation. An electric field as well as mechanical stress can switch the crystal symmetry (that is, polar axes). With an electric field it is possible to depole as well as repole piezoelectric ceramics, whereas mechanical stress only can depole the materials. Poled piezoceramics exhibit both direct and converse piezoelectric effects. The actuation phase (converse effect) consists of three parts. The first one is called intrinsic effect and covers the deformation of aligned domains. The second one is called extrinsic effect and involves the deformation caused by non-180-deg domains. It is believed to be the source of nonlinearity and losses in piezoceramics.[44] The third effect is caused by the electrostriction of materials, and as a result of this effect, the deformation is generally proportional to the square of the electric field. Electrostriction effects are much smaller than the other two effects.

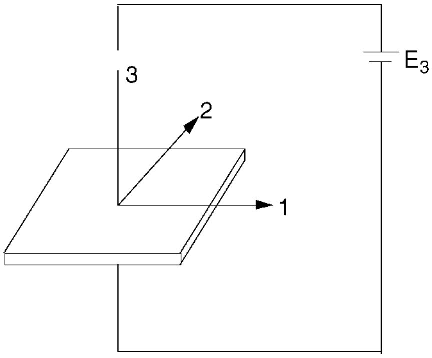

Fig. 3 Piezoelectric sheet with polarization along axis 3.

Piezoceramic materials are relatively well behaved and linear at low electric fields and low mechanical stress levels; they show considerable nonlinearity at high values of electric field and mechanical stress. The actuation strain can be modeled like an equivalent thermal strain. A piezoceramics sheet under surface excitation can be idealized as an orthotropic material (like composite unidirectional laminate). The constitutive relations are based on the assumption that the total strain in the actuator is the sum of the mechanical strain induced by the stress, the thermal strain caused by temperature, and the controllable actuation strain caused by the electric voltage. The axes are identified by numerals: 1 corresponds to the x axis, 2 corresponds to the y axis, and 3 corresponds to the z axis. Axis 3 is assigned to the direction of the initial polarization of the piezoceramic, and 1 and 2 axes lie in the plane perpendicular to 3 axis (Fig. 3).

Coupled electromechanical constitutive relations are as follows.[45]

Direct:

$$D_i = e^{\sigma}_{ij} E_j + d^d_{im}\sigma_m + a_i \Delta T$$

Converse:

$$\varepsilon_k = d^c_{jk} E_j + S^E_{km}\sigma_m + \alpha_k \Delta T$$

where vector D_i of size (3×1) is the dielectric displacement in newtons/millivolts or coulombs/square meter, ε_k is strain vector of size (6×1), E_j is the applied electric field vector of size (3×1) in volts/meter, and σ_m is stress vector of size (6×1) in newtons/square meter. The piezoelectric constants are the piezoelectric coefficients d^d_{im} (3×6) and d^c_{jk} (6×3) in meters/volt or coulombs/newton, the dielectric permittivity e^{σ}_{ij} of size (3×3) in newtons/square volt or farads/meter, and S^E_{km} is the elastic compliance matrix of size (6×6) in square meters/newton. The coefficient α_k is thermal coefficient vector of size (6×1) in 1/degrees Kelvin and a_i is thermal constants vector of size (6×1) in newtons/volt-meter-degrees Kelvin. The superscripts c and d refer to the converse and direct effects, respectively, and the superscripts σ and E indicate that the quantity is measured at constant stress and constant electric field, respectively. The converse equation represents the actuator equation, whereas the direct equation represents the sensor equation. Normally, the converse effect is used to determine piezoelectric coefficients.

Rewriting the converse equation in matrix form:

$$\begin{Bmatrix} \varepsilon_1 \\ \varepsilon_2 \\ \varepsilon_3 \\ \gamma_{23} \\ \gamma_{31} \\ \gamma_{12} \end{Bmatrix} = \begin{bmatrix} S_{11} & S_{12} & S_{13} & 0 & 0 & 0 \\ S_{12} & S_{11} & S_{13} & 0 & 0 & 0 \\ S_{13} & S_{13} & S_{33} & 0 & 0 & 0 \\ 0 & 0 & 0 & S_{44} & 0 & 0 \\ 0 & 0 & 0 & 0 & S_{44} & 0 \\ 0 & & 0 & 0 & 0 & 0_{66} \end{bmatrix} \begin{Bmatrix} \sigma_1 \\ \sigma_2 \\ \sigma_3 \\ \tau_{23} \\ \tau_{31} \\ \tau_{12} \end{Bmatrix}$$

$$+ \begin{bmatrix} 0 & 0 & d_{31} \\ 0 & 0 & d_{31} \\ 0 & 0 & d_{33} \\ 0 & d_{15} & 0 \\ d_{15} & 0 & 0 \\ 0 & 0 & 0 \end{bmatrix} \begin{Bmatrix} E_1 \\ E_2 \\ E_3 \end{Bmatrix} + \begin{Bmatrix} \alpha_1 \\ \alpha_2 \\ \alpha_3 \\ 0 \\ 0 \\ 0 \end{Bmatrix} \Delta T$$

In a plane perpendicular to the piezopolarization, it has isotropic properties, that is, transversely isotropic material in the plane 1-2. Note that, although orthotropic materials do not exhibit thermally induced shear strains, electric field components E_1 and E_2 can generate piezo-induced shear strains.

For piezoceramic materials the actuation strain is given by

$$\Lambda = \begin{bmatrix} 0 & 0 & d_{31} \\ 0 & 0 & d_{31} \\ 0 & 0 & d_{33} \\ 0 & d_{15} & 0 \\ d_{15} & 0 & 0 \\ 0 & 0 & 0 \end{bmatrix} \begin{Bmatrix} E_1 \\ E_2 \\ E_3 \end{Bmatrix}$$

where d_{33}, d_{31}, and d_{15} are called piezoelectric strain coefficients of a piezoelement. The d_{31} characterizes strain in the 1 and 2 directions caused by an electric field E_3 in the 3-direction and d_{33} relates strain in the 3-direction caused by field in the 3-direction. The d_{15} characterizes 2-3 and 3-1 shear strains caused by field E_2 and E_1, respectively. Thus, if an electric field E_3 is applied to a free piezoelement, it causes direct strains ε_1, ε_2, and ε_3. This is very similar to thermal strain. If an electric field E_1 or E_2 is applied, the material reacts with shear strain γ_{31} and γ_{23}, respectively. For orthotropic materials there is no corresponding thermal strain. To overcome this problem, it is better to assume piezoelectric materials as anisotropic.

If a compressive force is applied in the polarization direction (axis 3), or tensile force is applied in the plane perpendicular to polarization direction (axis 2 or 3), it will result in a voltage that has the same polarity as the original poling direction.

For piezoelectric film, PVDF, the induced strain is nonisotropic on the surface of the sheet. The induced strain is expressed as

$$\Lambda = \begin{bmatrix} 0 & 0 & d_{31} \\ 0 & 0 & d_{32} \\ 0 & 0 & d_{33} \\ 0 & d_{25} & 0 \\ d_{15} & 0 & 0 \\ 0 & 0 & 0 \end{bmatrix} \begin{Bmatrix} E_1 \\ E_2 \\ E_3 \end{Bmatrix}$$

For piezofilms the d_{31} is not equal to d_{32}, and d_{25} is not equal to d_{15}.

Piezoceramics are available commercially in the form of thin sheets (say, of thickness 0.254 mm) such as PZT-5H from Margon Matroc, and the manufacturer-supplied characteristics are shown in Table 3 (Ref. 46). Among piezoceramics PZT-5H is most widely used because of its lower electric field requirement than other actuators for the same strain. PZT-8 requires a higher field than PZT-5H but will need less power because of its lower dielectric constant. One major disadvantage of PZT-5H is that its dielectric and piezoelectric constants are very sensitive to temperature, and hence it can be

Table 3 Piezoelectric characteristics[46]

Coefficient	PZT-5H	PZT-8	PVDF
d_{31}	-274×10^{-12} m/V	−97	18–24
d_{32}	-274×10^{-12} m/V	−97	2.5–3
d_{33}	593×10^{-12} m/V	225	−33
d_{15}	741×10^{-12} m/V	330	——
Relative permittivity e_{33}	3400	1000	——
Free-strain range	−250 to +850	$\mu\varepsilon$	——
Poling field dc	12 kV/cm	5.5	——
Depoling field ac	7 kV/cm	15	——
Curie temperature	193°C	300	——
Dielectric breakdown	20 kV/cm	——	——
Density	7500 kg/m^3	7600	——
Open circuit stiffness E_{11}	62 GPa	87	——
Open circuit stiffness E_{33}	48 GPa	74	——
Compressive strength (static)	>517 MPa	>517	——
Compressive depoling limit	30 MPa	150	——
Tensile strength (static)	75.8	75.8	——
Tensile strength (dynamic)	27.6 MPa	34.5	——

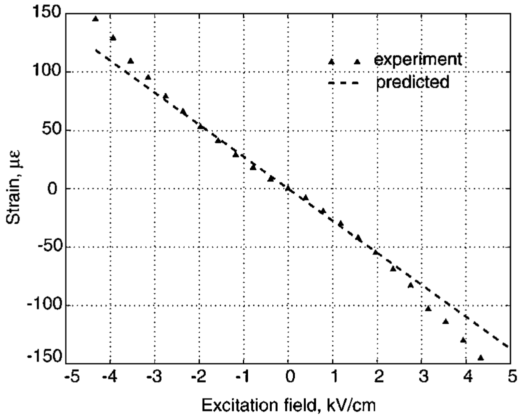

Fig. 4 Static-free strain of a PZT-5H sheet actuator.[48]

susceptible to self-heating problems because of its relatively large dissipation factor.

1. Static Free Strain

Figure 4 shows the transverse free strain (in a plane normal to the polarized direction) vs dc field. To avoid hysteresis and drift from the dc field, it is necessary bring to zero condition after each measurement on an initially dc cycled sheet. The curve is almost linear at low applied electric field levels and becomes nonlinear at high fields, more so for negative fields. The maximum positive field is limited by the breakdown of dielectric, whereas the maximum negative field is limited by the piezoceramic depoling. To obtain high actuation authority, these materials are often operated into nonlinear regimes. To predict actuator performance accurately, it becomes necessary to derive macroscopic models and analyses that are capable of addressing material nonlinearities including depolarization.

2. Effect of External Stress

Compressive stresses tend to align the c axis of the domains perpendicular to the direction of stress. If the stress is acting in the plane of piezosheet (normal to polarization direction), it destroys some of the initial polarization (that is, reduces the net polarization). This changes the piezoelectric coefficients and can cause a permanent degradation especially for soft ceramics like PZT-5H (Ref. 47). However, with applied tensile stress there is a slight increase in free strain. The increase in free strain is of the order of 10% at 3.9 kV/cm under a tensile stress of 2500 psi (about $\frac{1}{5}$th of ultimate stress) (Fig. 5).[48] A compressive stress along poling axis shows a slight increase in free strain and then levels off at high stress values.

3. Hysteresis and Drift

The steady strain response exhibits bias, and it takes about three cycles to stabilize it. There is a significant hysteresis for steady field, and the aspect ratio (lateral width) of the hysteresis increases with the field. Also, the hysteresis curve is asymmetric with respect to zero strain axes. The drift phenomenon is a slow increase of the free strain with time after the application of the dc field. After the application of the dc field, the strain jumps to a certain value and then increases slowly with time. When the field is switched off, the strain falls back to some value and then slowly decreases until some residual value is reached. This behavior of slow increase or slow decrease can be represented by a logarithmic expression,

$$\Delta\varepsilon = \Delta\varepsilon_0[1 + \gamma\,\ln(t/0.1)]$$

where $\Delta\varepsilon_0$ is the strain 0.1 s after the application of field and γ is a factor that depends on the material. The test data show that the percentage of drift is about same regardless of excitation field.[48] This drift can be as high as 15% for moderately high fields. The reason for this creep appears to be a gradual change in permanent polarization of the crystal (intrinsic effect). A superimposed small ac field (dither field) appears to show a small change in the drift phenomenon.

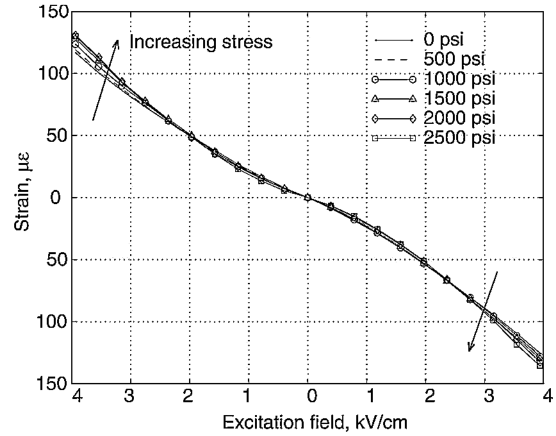

Fig. 5 Static strain of PZT-5H with transverse tensile stress.[48]

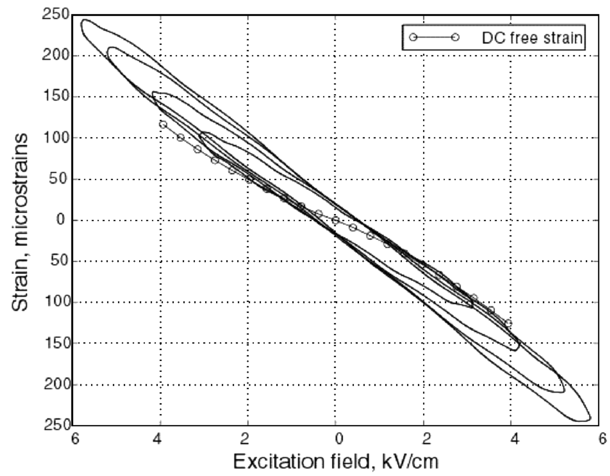

Effect of field at 5 Hz

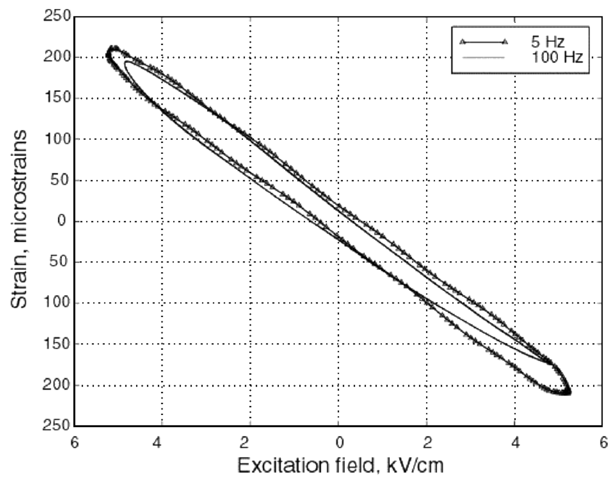

Effect of frequency

Fig. 6 Variation of strain hystereis with field and frequency for a free PZT-5H actuator.[48]

4. Dynamic Behavior

Figure 6 shows strain-field hysteresis loops with excitation frequency and field level. With an increasing field the overall shape of hysteresis is only slightly changed, but the mean slope increases with higher field. The area under the high frequency excitation is slightly less than the area under the low frequency showing more energy losses at low frequencies. A dc bias field increases the value of d_{31} as a result of pinning of the domains (domains better aligned) and also reduces the losses.

For a free piezoceramic the strain almost remains constant with frequency except at high frequencies and high fields, and the strain

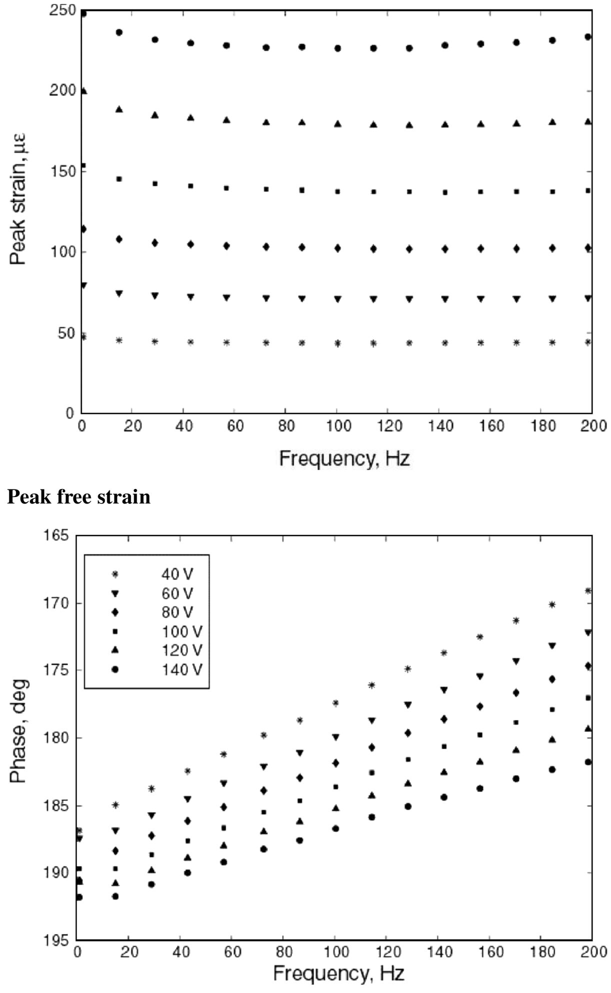

Fig. 7 Response of a free PZT-5H actuator.[48]

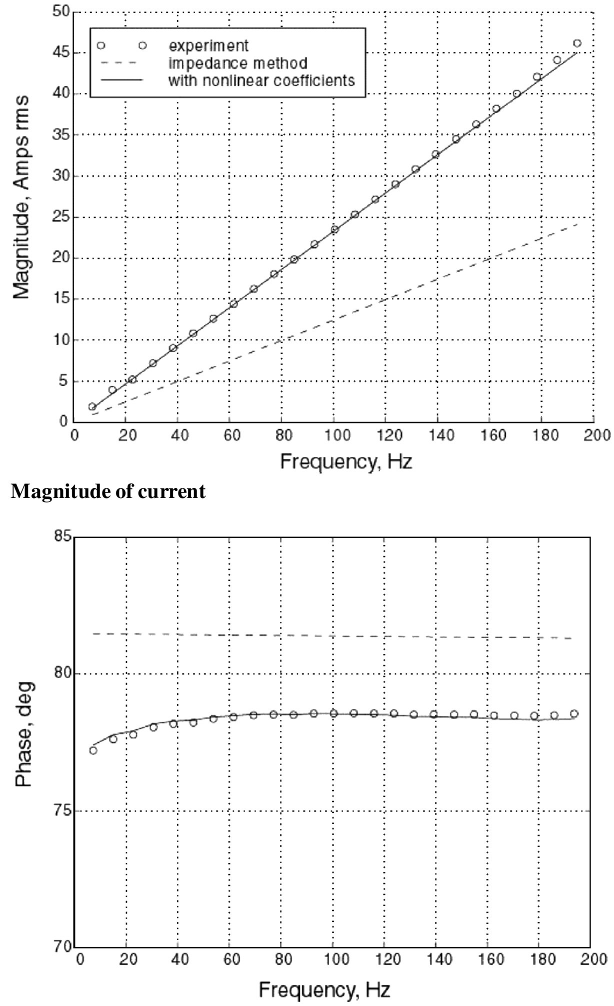

Fig. 8 Current consumption for a pair of actuators surface bonded to an aluminum beam with 3 kV_{rms}/cm excitation.[48]

increases by about 15% as a result of nonlinear effects, whereas the phase changes considerably with the excitation frequency and field strength (Fig. 7). For actuators bonded to a structure (say, to an isotropic beam), the strain increases with frequency; however, the change of phase with field strength is small. This shows that the total impedance of the actuator-beam system is more capacitive in nature. It is possible to predict the power consumption of free and surface-bonded actuators satisfactorily using the impedance method, given the variation of the dielectric permittivity and dissipation factor with field for a free actuator (Fig. 8). Generally, the accuracy of prediction deteriorates at high field (above 4.8 kV_{rms}/cm) and frequency (above 100 Hz).

5. Depoling Behavior

When the piezoelement is exposed to a high electric field opposite to the poling direction, it loses its piezoelectric property, accompanied by more dielectric losses and lower efficiency. This is called depoling of piezoelectric and results in a permanent deformation. For PZT-5H the dc depoling field is approximately 5.5 kV/cm. Under an ac excitation the depoling field of the actuator becomes lower than the dc value (Fig. 9). Figure 10 shows the effect of depoling on the actuator response. Once at or above the depoling field, it takes a few seconds to depole, and the strain-field hysteresis loop transforms into a "butterfly loop." It is accompanied by a rapid increase in current drawn (more energy loss). If a much higher negative field is kept for a long time, the material gets polarized along the new poling direction. Thus, it is possible to repole the piezoelectric specimen by means of exciting it with ac field or dc field. Although repoling actuators bonded to the surface of a beam is possible, a tensile stress is induced in the actuator, which might cause it to

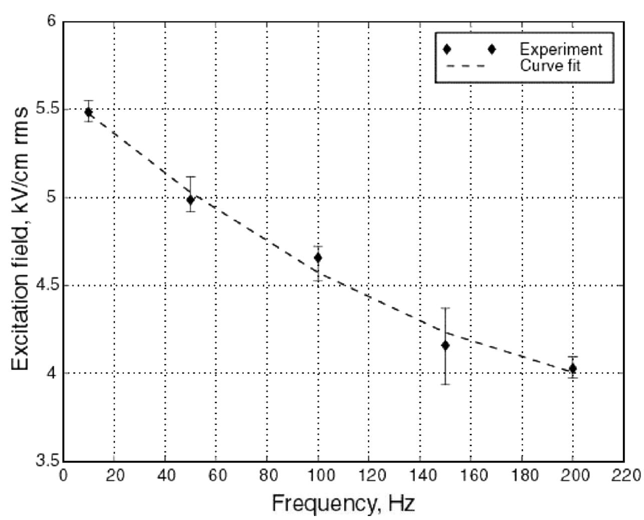

Fig. 9 Variation of depoling field with frequency.[48]

crack. If the piezoelectric element is repoled with an ac field, it is recommended to apply a dc bias field. This will ensure that the electric field in the poling direction exceeds the poling threshold, while keeping the negative field below the depoling limit. To improve the repeatable performance data of a piezoelectric element, it is recommended to apply cyclic treatment. The process involves application of slightly higher field (dc or ac) than needed and then shutting off the field. The process is repeated several times until the residual

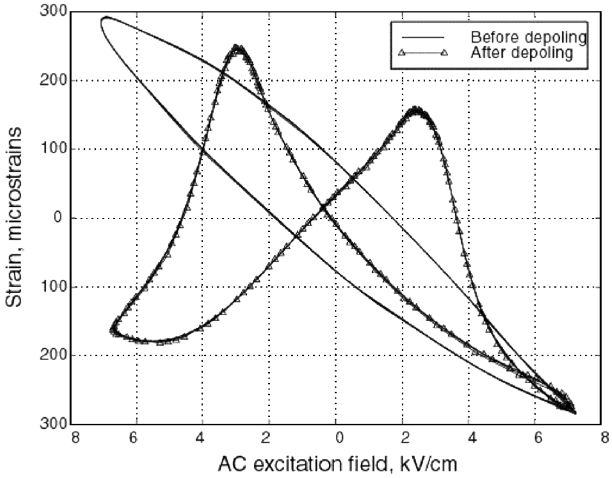

Comparison of depoled response

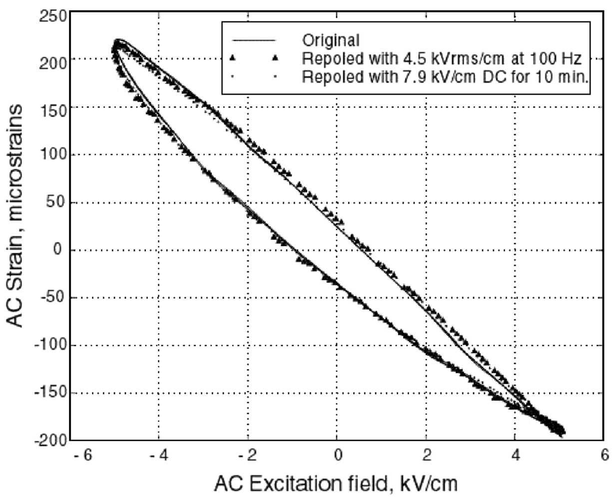

Repoling effectiveness

Fig. 10 Depoling strain behavior.[48]

strain gets stabilized. Depoling is also possible if the temperature exceeds the Curie temperature or if a large stress is applied. At Curie temperature the ferroelectric material undergoes phase transition to paraelectric material and suddenly loses its characteristic behavior. At high frequencies, energy from mechanical losses can generate enough self-heating that can severely affect the performance of the actuator. Ghandi and Hagood[49] developed nonlinear modeling and characterization techniques for phase transitions in electromechanically coupled materials. This is especially suited to repolarization in ferroelectrics (PZTs). Blocks of PZT were tested under multiaxial electrical and mechanical loading conditions, and required parameters for modeling were determined. Lynch[50] developed multiaxial phenomenological-based constitutive relations (at macroscale) for ferroelectric ceramics that included hysteresis, rate dependence, and saturation. It might be important to validate these with test data for a range of test conditions.

6. *Manufacturing Issues*

There are several issues concerning building of smart structures. These are the following:

1) Electrical contact on both sides of piezo is required. One way to overcome this problem is to use an oversize thin conductor sheet between actuator and substrate with one surface insulated; the second way is to drill a hole in the substructure and use nonconducting epoxy.

2) For proper transfer of induced strain to main structure, the bond layer thickness needs to be thin, sufficiently stiff, and uniform. For this, pressure is applied during curing.

Embedding vs surface-mounting. With surface-mounted actuators there is a better access for fabrication, an easier access for inspection, and less maintenance cost. Because of exposure, actuators are more susceptible to damage. Also, the functioning of actuators is dependent on structural surface. Embedded actuators become inaccessible for inspection. The devices, however, are better protected, and interconnections with other devices become easy. Also with embedding, the piezoelectric must have an elastic modulus comparable to the host structure in order to avoid structural discontinuity, and the Curie temperature should be higher than the curing temperature of composites. Further, piezodevices must be electrically insulated from the host structure. This means that the piezoelements can be directly embedded in glass/epoxy laminas but need an insulating layer with graphite/epoxy laminas. However, an insulating layer can reduce the effectiveness of the actuator. It appears appropriate to wrap the piezodevice in a 0.05-mm-thick Kapton film (Dupont) and use acrylic epoxy to reduce slippage between piezo and insulating layer. Overall, there are many issues related to integration of piezoceramic elements in composite structure for various applications.[51]

Embedding electronics. To embed integrated circuits in a host structure, it is essential to insulate them electrically, ventilate thermally, and isolate them mechanically from load paths.[52] For a minimal degradation of structure, it is important to have a minimum ply interruption.

Current piezoceramic materials have a maximum free strain of the order of 1000 microstrain and stiffness of the order of 50–90 GPa. Careful configurations of the actuator geometry in conjunction with amplification/rectification mechanisms are needed to increase the performance of an actuator for a specific application. PZT actuators are available in the form of thin sheets, and their d_{31} effect is used for actuation. Typical free strains are of the order of $+250$ to -1000 microstrain (limited by depoling and dielectric breakdown, respectively).

Thus, there is a need to undertake extensive testing of engineering specimens (macrolevel) to represent most of the operating conditions such as stress, strain, temperature, and voltage. Building smart structures encompasses new fabrication methods that require experience and expertise in fabricating complex systems with embedded or surface-mounted smart actuators and sensors. Sheet actuators are convenient for surface bonding or embedding in a laminated structure. The bond layer between PZT and the host structure has a major impact on the strain transfer to the host structure and the local stress distribution. Piezoelectric actuators are also available in specialized configurations such as RAINBOW, THUNDER, and the C-block actuators. To increase transverse actuation of piezoceramic wafers, interdigitated electrode piezoelectric fiber composites are developed where alternating electrodes are subjected to positive and negative voltages.[53,54] As a result, d_{33} effect is used in actuation. This active fiber composite (AFC) utilizes interdigitated electrode poling and piezoelectric fibers embedded in an epoxy matrix, resulting in a high-performance actuator laminate. The disadvantages of this actuator are cost, difficulty of processing and handling during fabrication, and high voltage requirement. Recently, patch actuators with interdigitated electrodes, which use the d_{33} effect, have become available commercially.[55] Also recently, low-cost microfiber composite (MFC) are becoming available for various applications.[56] To increase the actuation force, multilayered stack actuators are used. In spite of using the d_{33} effect, the total displacement is quite small. Because of laminated structure with alternating bond and piezolayers, stacks typically operate only under compressive loads.

Piezoceramics are widely used as actuators and sensors for active vibration control of beams and plates.[57–59] To increase their strain output, these are often operated under high electric fields, which results in a significant nonlinear behavior of their characteristics. Mukherjee et al.,[60] Yang et al.,[61] and Ren et al.[62] carried out testing of piezoceramic sheet actuators under a range of temperature, frequency, electric field, dc bias, and applied stress for both soft (EC-65, EC-76) and hard (EC-64, EC-69) PZTs (manufactured by EDO Ceramics). These measured results showed the need of including nonlinear dependence of piezoelectric constants on applied field and stress.

As mentioned earlier, the characteristics of piezoelectric materials change under mechanical stress.[47,61,62] Piezoceramics are normally brittle, and, therefore, the effect of dynamic stress on their characteristics is a major concern. Recently, there have been some limited focused efforts to evaluated their fatigue characteristics and dynamic conditions.[63–66]

Most actuators utilize direct piezoelectric effects (d_{31} and d_{33}). There have been some selected attempts to build torsional actuators using shear piezoelectric effect (d_{51}) (Refs. 67 and 68). Bonding together segmented piezoceramic bars that are poled in axial direction and arranging in opposite poling direction form a cylindrical actuator. A major drawback is very field requirement (in several kilovolts) to achieve desired torsional deflection.

At this time, a reliable detailed database of piezoelectric characteristics for a range operating conditions such as electric field, stress/strain level, and temperature is not readily available. It might require extensive testing of standardized piezoelectric elements at macrolevel under controlled environment in specialized test machines. Simplified constitutive relations for nonlinear high field conditions need to be developed. Depolarization caused by alternating field in terms of performance degradation needs to be examined. For most applications electromechanical fatigue characteristics become important and need to be investigated systematically. Complex geometries, which result in nonuniform fields and stress distributions, should be examined systematically through detailed modeling and refined testing techniques. Modeling issues related to interdigitated electrode piezoelectric fiber composites need carefully scrutiny and validations.

D. Piezoelectric Sensors

The direct piezoelectric effect is the electric displacement that is generated when a piezoelectric material is mechanically stressed and can be used to sense structural deformation. Most applications rely on either the voltage or rate of change of voltage generated by the sensor or the frequency spectrum of the signal generated by the sensor. A major advantage of using piezoelectric sensors as opposed to conventional foil strain gauges is their superior signal-to-noise ratio and high-frequency noise rejection. In applications involving low strain levels, one requires much less signal conditioning with piezoelectric sensors, and, as such, they are less sensitive to noise. Other advantages are their compactness and sensitivity over a large strain bandwidth and ease of embeddability. Most commonly used sensors are piezofilm (PVDF) because of its low stiffness. Sometimes, piezoceramic (PZT) sensors are used for specific applications. For example, it might be possible to use piezoceramics for both sensing and actuation especially for collocated control strategies.[69–73] The PZT sensors exhibit high Young's modulus, brittleness, and low tensile strength. Also, they suffer from creep with dc field, depolarization under high stress conditions, and linearity at high strains. In spite of these problems, some researchers have used piezoceramic sheet sensors in controllable structural systems[74,75] and in health monitoring applications.[76] Giurgiutiu and Zagrai[77] carried out a comparative evaluation of different PZT sheet sensors. Because of the way the material is stretched during manufacturing, the PVDF behaves as piezoelectrically orthotropic but mechanically isotropic for small strains.

The direct effect equations are

$$\begin{Bmatrix} D_1 \\ D_2 \\ D_3 \end{Bmatrix} = \begin{bmatrix} 0 & 0 & 0 & 0 & d_{15} & 0 \\ 0 & 0 & 0 & d_{25} & 0 & 0 \\ d_{31} & d_{32} & d_{33} & 0 & 0 & 0 \end{bmatrix} \begin{Bmatrix} \sigma_1 \\ \sigma_2 \\ \sigma_3 \\ \tau_{23} \\ \tau_{31} \\ \tau_{12} \end{Bmatrix} + \begin{bmatrix} e^{\sigma}_{11} & 0 & 0 \\ 0 & e^{\sigma}_{22} & 0 \\ 0 & 0 & e^{\sigma}_{33} \end{bmatrix} \begin{Bmatrix} E_1 \\ E_2 \\ E_3 \end{Bmatrix} + \begin{bmatrix} a_1 \\ a_2 \\ a_3 \end{bmatrix} \Delta T$$

The sensor equations are based on direct effect. The sensor is exposed to a stress field, which in turn generates an electric field. Monolithic PZT sensors are transversely isotropic, and as a result $d_{31} = d_{32}$ and $d_{15} = d_{25}$. Consider a case where electric field is zero and there is no thermal strain:

$$\begin{Bmatrix} D_1 \\ D_2 \\ D_3 \end{Bmatrix} = \begin{bmatrix} 0 & 0 & 0 & 0 & d_{15} & 0 \\ 0 & 0 & 0 & d_{25} & 0 & 0 \\ d_{31} & d_{32} & d_{33} & 0 & 0 & 0 \end{bmatrix} \begin{Bmatrix} \sigma_1 \\ \sigma_2 \\ \sigma_3 \\ \tau_{23} \\ \tau_{31} \\ \tau_{12} \end{Bmatrix}$$

A stress field causes an electric displacement, which in turn is related to the charge generated:

$$q = \iint [D_1 \quad D_2 \quad D_3] \begin{bmatrix} \mathrm{d}A_1 \\ \mathrm{d}A_2 \\ \mathrm{d}A_3 \end{bmatrix}$$

where $\mathrm{d}A_1$, $\mathrm{d}A_2$, and $\mathrm{d}A_3$ are, respectively, the differential electrode areas in the 2-3, 1-3, and 1-2 planes. The charge q and voltage V_c are related by the capacitance of the sensor C_p as

$$V_c = q/C_p$$

Knowing the voltage, it is thus possible to measure the stress and hence the strain. Consider a sheet sensor with two faces coated with thin electrode layers. In case of uniaxial stress field (in direction 1), the capacitance is given as

$$C_p = e^{\sigma}_{33} l_c b_c / t_c$$

where l_c, b_c, and t_c are length, width, and thickness of the sensor, respectively. Assuming strain along the 1-direction, it follows that

$$V_c = \frac{d_{31} Y_c b_c}{C_p} \int_{l_c} \varepsilon_1 \, \mathrm{d}x$$

where Y_c is Young's modulus of the sensor and ε_1 is averaged over the gauge length. The strain is calculated as

$$\varepsilon_1 = \frac{V_c C_p}{d_{31} Y_c l_c b_c}$$

For this relation it is assumed that only the strain in the 1-direction exists, and there is no loss of strain in the bond layer. With the including of Poisson's effect, this relation reduces to

$$\varepsilon_1 = \frac{V_c C_p}{d_{31}[1 - \nu(d_{32}/d_{31})] Y_c l_c b_c}$$

where ν is Poisson's ratio. For conventional foil gauges the transverse sensitivity is close to zero and normally neglected. In a general situation it is not possible to separate out the principal strains using one piezoelectric sensor. Unless the transverse strain is known a priori, it is not possible to obtain longitudinal strain using one sensor.

The effect of bond layer is determined assuming a uniform stain beam theory. As a result of shear lag effect in the bond layer, the effective length and width of sensor get reduced:

$$\varepsilon_1 = \frac{V_c C_p}{d_{31}[1 - \nu(d_{32}/d_{31})] Y_c l_{c_{\mathrm{eff}}} b_{c_{\mathrm{eff}}}}$$

The effective length and width of a sensor are function of sensor and bond-layer characteristics. Reference 78 presents a procedure to determine these values. Because of lower thickness and stiffness of a typical PVDF sensor, it shows a much lower shear lag loss than a PZT sensor.

1. Signal Conditioning

To measure accurately the output of piezoelectric sensor, it needs to be passed through some signal conditioning system. Typically, the output impedance of piezoelectric sensor is very high while the measuring device such as a voltmeter has comparatively low input impedance (order of 1 MΩ). The objective of signal conditioning systems is to provide a signal with low output impedance while maintaining high input impedance to the sensor. One way is to short the electrodes of the sensor with a suitable resistor and then measure the current passing through this resistor using an amplifier. The second way is to use a charge amplifier to measure charge generated by the sensor, as shown in Fig. 11. In this circuit C_p is capacitance of sensor, C_c represents capacitance of cables, and C_F is feedback capacitance. The value of time constant as given by $R_F C_F$ can be selected to achieve the desired frequency range.

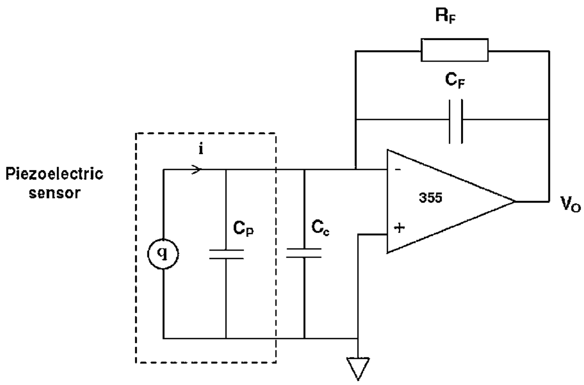

Fig. 11 Charge amplifier circuit to measure strain with piezoelectric sensor.

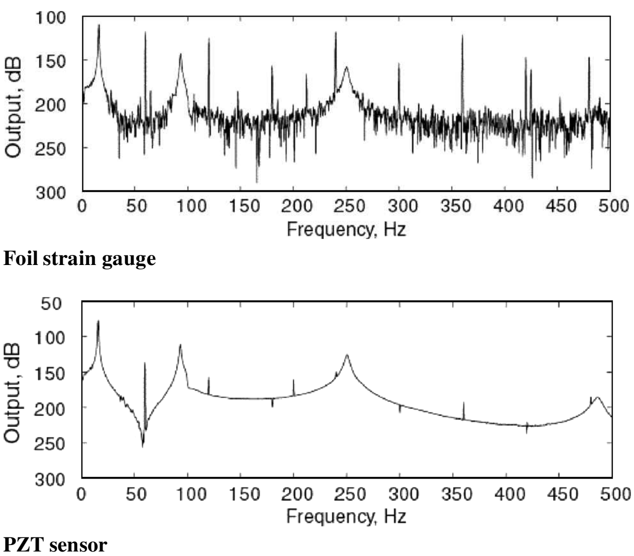

Fig. 12 Foil strain gauge and PZT sensor impulsive response in frequency domain.[78]

The sensitivity of piezoelectric sensor is far superior than that of conventional foil type strain gauges, with much less signal conditioning required, especially for applications involving low strains and high noise levels. Figure 12 shows impulsive unfiltered response from both a conventional foil strain gauge and a PZT strain sensor, taken simultaneously after the cantilevered beam was impacted at its tip. There is significant background noise in the foil gauge output as compared to the PZT output. The spikes in PZT output are the overtones of the ac power-line frequency.

It is not advisable to use these sensors to measure strain above 150–200 microstrains because of increasing nonlinear piezobehavior. The output of the PZT sensor requires no temperature correction over a moderate range of operating temperatures (say less than 40°C). Figure 13 shows measured strain results from strain gauge, PZT sensor, and PVDF sensor of size $7.1 \times 3.6 \times 0.056$ mm attached at the root of a cantilevered aluminum beam. Correlation is generally quite satisfactory. For a constant gauge length sensitivity increases with increasing sensor area. Also, as the size of sensor increases the shear lag losses as a result of bond layer decrease, and there is a better transfer of strain from the surface of the structure to the sensor. However, the larger sensor measures average strain over a larger area instead of local strain and also can add stiffness to the baseline structure, especially with PZT sensors. Even though the piezoelectric properties (dielectric permittivity and piezoelectric coefficients) change with temperature, the overall effect on the calibration of PZT sensors is small away from Curie's limit. On the other hand, PVDF exhibits a significant change of pyroelectric properties with temperature in addition to change in piezoelectric properties. Hence, PVDF sensors are relatively sensitive to temperature, and suitable temperature compensation must be included in measurements. For some specific measurements specially shaped distributed PVDF sensors can increase the performance significantly.[79,80] Piezoelectric strain sensors are simple, easy to use, and a reliable alternative to conventional resistance-based foil strain gauges.

There have been limited attempts to validate systematically the calibration factor for piezoelectric sensors for a wide range of frequencies and strain levels. Doubtless, the sensitivity of sensor depends upon strain distribution (baseline structural configuration and loading), sensor size, temperature, and fabrication techniques (bond layer thickness). There is a need to establish guidelines to optimize the sensitivity of piezoelectric sensor under different operating conditions. It is equally important to develop signal-conditioning circuitry to cover a wide range of frequencies.

III. Modeling: Beam with Induced Strain Actuation

A one-dimensional beam with surface-bonded or embedded induced strain actuators represents a basic and important element of

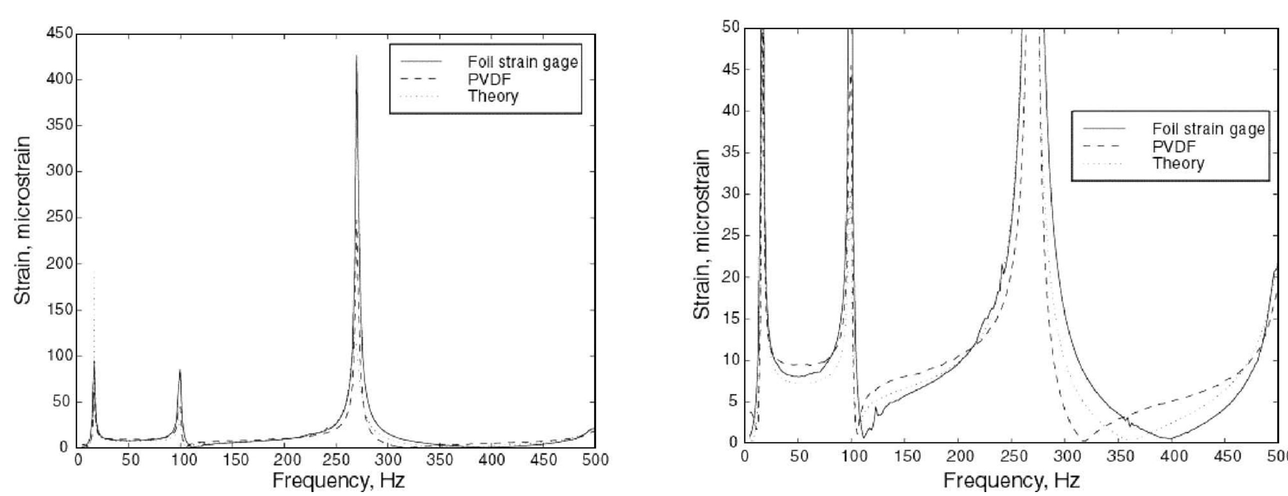

Fig. 13 Correlation of measured foil strain gauge strain and PVDF sensor strain and theoretical predictions.[78]

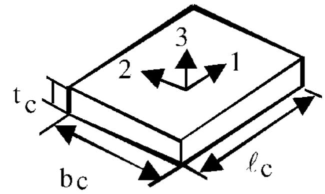

Fig. 14 Piezoelectric element.

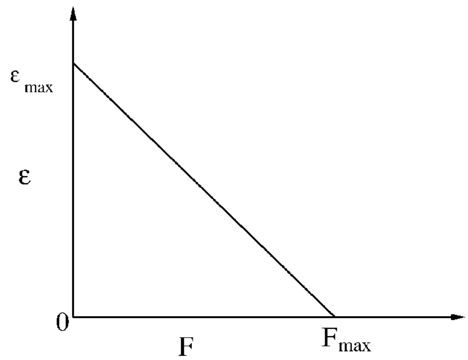

Fig. 15 Force-strain characteristic of a piezoelement.

an adaptive structure. Many structural systems such as helicopter blades, airplane wings, turbo-machine blades, missiles, space structures, and civil structures are routinely represented as slender beams. With induced strain actuation it might be possible to actively control aerodynamic shape for vibration suppression, stability augmentation, and noise reduction. Several beam theories have been developed to predict flexural response of isotropic and anisotropic beams with surface-bonded and embedded induced strain actuation that range from simplified models to detailed models involving uniform, linear, and nonlinear displacement distribution through the thickness.

An induced strain actuator such as a piezeceramic sheet actuator is defined using two key parameters: free strain and block force. Let us consider a piezoelectric actuator of length ℓ_c, width b_c, and thickness t_c (Fig. 14), the maximum free strain Λ for an electric field V (voltage) is

$$\varepsilon_{\max} = \Lambda = d_{31}(V/t_c)$$

where d_{31} is piezoelectric constant (m/V). The maximum block force (zero strain condition) is

$$F_{\mathrm{bl}} = d_{31} E_c b_c V$$

where E_c is the Young modulus of elasticity of piezo actuator.

Let us imagine that an extensional free strain Λ is produced in longitudinal direction (axis 1) caused by an electric field V applied in the polarized direction (axis 3). Now if a compressive force F is applied to the piezo in longitudinal direction, the net strain will be

$$\varepsilon = \Lambda - F/F_{\mathrm{bl}}$$

The strain at any compressive force F is plotted in Fig. 15.

Two identical actuators mounted on the surface of a beam, one on either surface, can produce pure bending or pure extension (Figs. 16a and 16b). For pure bending an equal but opposite potential is applied to top and bottom piezos, whereas for pure extension the same potential is applied to both piezos. Piezos experience equilibrating stresses. For example, for pure extensional case both piezos experience compressive stress.

To model one-dimensional structures such as slender beams, let us first start with simple beam models and then discuss refined models. Among the simple models, popular ones are block force model, uniform strain model, and Euler–Bernoulli model.

A. Block-Force Beam Model

This is the most simple beam model, where each piezoactuator is represented in terms of its block force and free strain. The

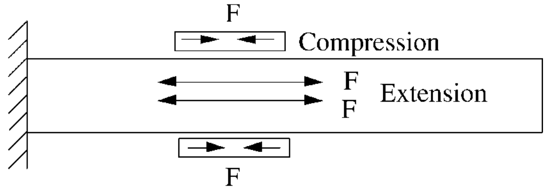

Fig. 16a Pure extension (same voltage to top and bottom piezos).

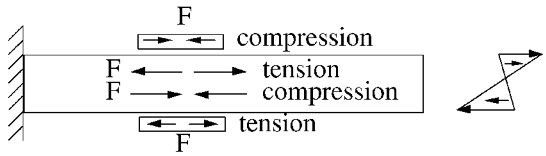

Fig. 16b Pure bending (equal but opposite voltage to top and bottom piezos).

piezo introduces a local strain to substrate and in turn experiences an equilibrating force. Let us consider a case of beam with two identical actuators respectively surface bonded to top and bottom surfaces.

For a pure extension case the same potential is applied to top and bottom actuators. The induced force is

$$F = F_{\mathrm{bl}} \frac{EA_b}{EA_b + EA_c}$$

where F_{bl} is a block force of each piezoelement. The extensional stiffness of beam and actuators are defined as

$$EA_b = E_b b_b t_b, \qquad EA_c = 2E_c b_c t_c$$

If actuator stiffness $EA_c \gg EA_b$ (beam stiffness), the actuation force tends to zero although the actuation strain equals free strain. On the other hand, if the actuator stiffness $EA_c \ll EA_b$ the actuation strain becomes zero although actuation force equals block force.

For a pure bending case an equal and opposite potential is applied to top and bottom actuators, and the induced bending moment is

$$M = M_{\mathrm{bl}}\left(\frac{EI_b}{EI_b + EI_c}\right)$$

where M_{bl} is block moment and is equal to $F_{\mathrm{bl}} t_b$. The bending stiffness of beam and actuators are defined as

$$(EI)_b = E_b I_b = \tfrac{1}{12} E_b b_b t_b^3, \qquad (EI)_c = 2(b_c t_c)(t_b/2)^2 E_c$$

Again, if $EI_c \gg EI_b$ actuation moment becomes zero, and on the other hand, if $EI_c \ll EI_b$, actuation strain becomes zero. This method is quite insightful and is used for design studies.

B. Uniform-Strain Beam Model

This model helps to understand and substantiate the effect of bond layer. Let us consider two identical strain-induced actuators that are bonded to an isotropic beam, one to the top surface and the second to the bottom surface of the beam (Fig. 17). Between the actuator and the beam surface, there is a finite thickness elastic bond. The bond layer is assumed to undergo pure shear strain. Each actuator is assumed to induce a uniform strain across its thickness. For pure bending a linear distribution of strain is assumed in the host structure.

The surface strain on beam substructure and actuator strain are derived as

$$\frac{\varepsilon_b^s}{\Lambda} = \frac{\alpha}{\alpha + \Psi}\left[1 - \frac{\cosh(\Gamma\bar{x})}{\cosh\Gamma}\right]$$

$$\frac{\varepsilon_c}{\Lambda} = \frac{\alpha}{\alpha + \Psi}\left[1 + \frac{\Psi}{\alpha}\frac{\cosh(\Gamma\bar{x})}{\cosh\Gamma}\right]$$

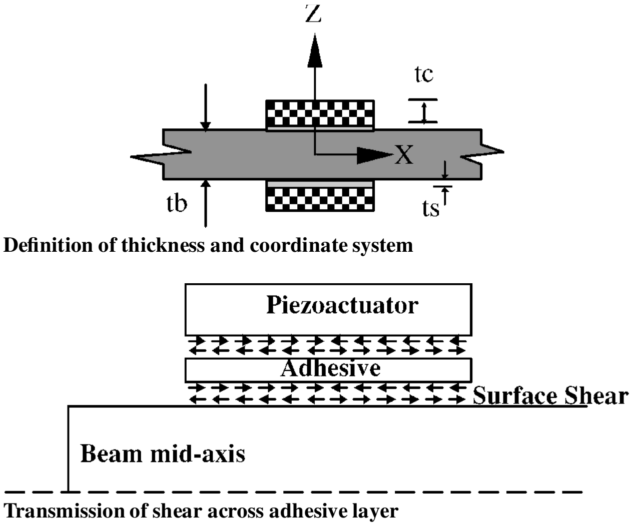

Fig. 17 Diagram of beam mounted with symmetric actuators.

where $\alpha = 2$ is for pure extension and $\alpha = 6$ is for pure bending. Other constants are defined as

$$\bar{x} = \frac{x}{\ell_c/2}, \qquad \Gamma^2 = \frac{G_s}{t_s E_c}\left(\frac{1}{t_c} + \frac{E_c \alpha}{E_b t_b}\right)\frac{\ell_c^2}{4}$$

$$\psi = \frac{(EA)_b}{E_c A_c} = \frac{E_b t_b}{E_c t_c}$$

where t_s is the thickness and G_s is the shear stiffness of the adhesive. The parameter Γ is the shear lag parameter, and the larger the value, the lower the actuation loss through the bond layer (for example, as a result of a thin bond line or high adhesive shear stiffness).

A very thin bond ($\Gamma > 30$) approximately represents a perfect bond condition, and strain distributions reduce to

$$\varepsilon_b^s \big/ \Lambda = \varepsilon_c/\Lambda = \alpha/(\alpha + \Psi)$$

This means that the induced strain on the surface of a host structure is equal to the actuator strain, and it is proportional to the product of the actuation free strain Λ and the reciprocal of one plus the stiffness ratio (beam stiffness/actuator stiffness). The second term is as a result of the impedance matching. The higher the stiffness of the actuator, the more effective is the strain transfer.

C. Bernoulli–Euler Beam Model

The Bernoulli–Euler model is a consistent strain model and assumes the beam, adhesive, and actuator as a continuous structure and follows the Bernoulli's assumption. This means that a plane section normal to the beam axis remains plane and normal to the beam axis after bending. It is assumed that there is a linear distribution of strain in the actuator and host structure and that shearing effects are negligible.

The strain distribution is

$$\varepsilon(z) = \varepsilon_0 - z\kappa$$

where κ is bending curvature $= -w_{,xx}$. The net strain is

$$\varepsilon_{\text{net}} = \varepsilon(z) - \Lambda(z)$$

The force and moment expressions can be written as

$$\begin{Bmatrix} F + F_\Lambda \\ M + M_\Lambda \end{Bmatrix} = \begin{bmatrix} (EA)_{\text{tot}} & (ES)_{\text{tot}} \\ (ES)_{\text{tot}} & (EI)_{\text{tot}} \end{bmatrix} \begin{Bmatrix} \varepsilon_0 \\ w'' \end{Bmatrix}$$

where

$$(EA)_{\text{tot}} = \int_{-h/2}^{h/2} b(z)E(z)\,\mathrm{d}z \qquad \text{extensional stiffness}$$

$$(ES)_{\text{tot}} = \int_{-h/2}^{h/2} b(z)E(z)z\,\mathrm{d}z \qquad \text{coupling stiffness}$$

$$(EI)_{\text{tot}} = \int_{-h/2}^{h/2} b(z)E(z)z^2\,\mathrm{d}z \qquad \text{bending stiffness}$$

$$F_\Lambda = \int_{-h/2}^{h/2} b(z)E(z)\Lambda(z)\,\mathrm{d}z \qquad \text{induced force}$$

$$M_\Lambda = \int_{-h/2}^{h/2} b(z)E(z)\Lambda(z)z\,\mathrm{d}z \qquad \text{induced moment}$$

where F_Λ and M_Λ are respectively axial force and bending moment as a result of induced strain. $(ES)_{\text{tot}}$ is equivalent to a coupling term. If the placement of actuators is symmetric, this term will be zero. If an actuator is attached only on one side, this term will be nonzero (extension-bending coupling).

For an isotropic beam with pure bending actuation,

$$M_\Lambda = E_c b \Lambda t_c (t_b + t_c)$$

$$(EI)_{\text{tot}} = E_c t_c b\left(\frac{2}{3}t_c^2 + t_b t_c + \frac{t_b^2}{2}\right) + \frac{E_b b t_b^3}{12}$$

$$M_\Lambda = (EI)_{\text{tot}} w'', \qquad F_\Lambda = 0$$

$$\varepsilon = z\frac{M_\Lambda}{(EI)_{\text{tot}}} = \frac{6(1 + 1/T)(2/t_s)\Lambda}{(\Psi + 6) + 12/T + 8/T^2}z$$

The thickness ratio T $(= t_b/t_c)$ determines whether the strain variation across the piezoelement affects the analysis. Figure 18 shows the variation of the normalized curvature with the thickness ratio. For a case with piezo stretched across the beam width, and with a thickness ratio of 5, there is a 2.7% difference between the predictions caused by the uniform strain model and the Bernoulli–Euler model. For thin beams, the uniform strain model overpredicts strain (curvature). For large thickness ratios the predicted induced bending curvatures are identical using both methods. For thickness ratios of one or less, neither of these methods works well. More details about these beam models can be obtained from Refs. 81–84. Banks and Zhang[85] developed a curved beam analysis for a pair of surface-attached piezoelectric patches based on the Donnell–Mushtari theory for shell models and B-spline basis elements. They successfully reduced the analysis to straight beams without any locking problem.

Assume two identical actuators are embedded in an isotropic beam at an equal distance from midplane of the beam resulting in a symmetric configuration (Fig. 19). For a very thin bond layer between the actuators and the beam, a perfect bond assumption appears valid. An equal voltage applied to both actuators results in pure extension, whereas an equal but opposite voltage applied to both actuators causes pure bending of the beam.

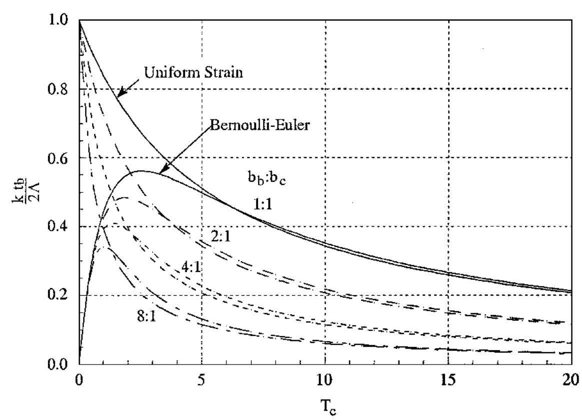

Fig. 18 Single actuator normalized curvature comparison for a perfect bond condition.[83]

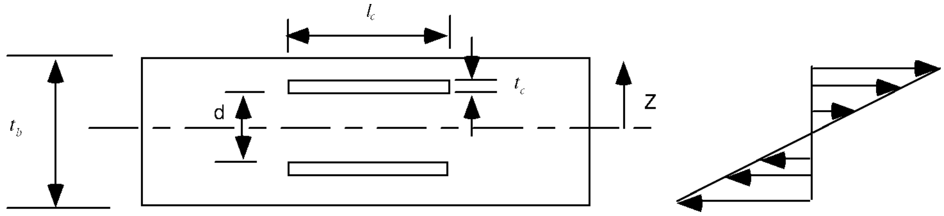

Fig. 19 Beam with embedded piezoelements.

Combine bending-extension relations into the matrix

$$\begin{Bmatrix} F + F_\Lambda \\ M + M_\Lambda \end{Bmatrix} = \begin{bmatrix} EA_{\text{total}} & ES_{\text{total}} \\ ES_{\text{total}} & EI_{\text{total}} \end{bmatrix} \begin{Bmatrix} \varepsilon_0 \\ \dfrac{d^2 w}{dx^2} \end{Bmatrix}$$

where the stiffness terms gets modified. The matrix form of these governing equations is similar to that for surface-bonded actuators, except that the stiffness terms need to be modified to account for the embedded location for the actuators.

Ghiringhelli et al.[86] developed a semianalytical formulation for an arbitrary cross-section beam with embedded piezoelectric elements and showed good agreement of their predicted results with three-dimensional model results.

D. Energy Formulation

Using the same basic assumptions as used in the force equilibrium formulation, the principle of virtual work can provide the governing equations and boundary conditions that can be easily adapted to dynamic systems. Assuming that the only allowable modes of deformation are actuator extension, adhesive shear, and beam bending and extension, the strain energy relations can be directly written.

Beam extension:

$$U_b^0 = \frac{1}{2}\int_{-l_c/2}^{l_c/2} E_b A_b \left(\frac{\partial u_b^0}{\partial x}\right)^2 dx$$

Beam bending:

$$U_b^\kappa = \frac{1}{2}\int_{-l_c/2}^{l_c/2} E_b I_b \left(\frac{\partial^2 w}{\partial x^2}\right)^2 dx$$

Substrate shear:

$$U_s = \frac{1}{2}\int_{-\ell_c/2}^{\ell_c/2} G_s A_s (\gamma_s)^2\, dx$$

Actuator extension:

$$U_c = \frac{1}{2}\int_{-\ell_c/2}^{\ell_c/2} E_c A_c \left(\frac{\partial u_c}{\partial x} - \Lambda\right)^2 dx$$

Define

$$I_b = \frac{1}{12} A_b t_b^2, \qquad U_b^\kappa = \frac{1}{2}\int_{-l_c/2}^{l_c/2} \frac{E_b A_b}{3}\left(\varepsilon_b^s - \varepsilon_b^0\right)^2 dx$$

$$U_s = \frac{1}{2}\int_{-\ell_c/2}^{\ell_c/2} \frac{G_s A_s}{t_s^2}\left(u_c - u_b^s\right)^2 dx$$

The principle of virtual work for static behavior is mathematically stated as

$$\delta W_E = -\delta U$$

It will result in governing equations and boundary conditions, as obtained directly with the uniform-strain model.[83]

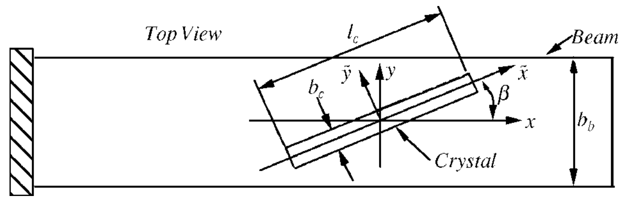

Fig. 20 Piezoaxis offset from the beam axis.

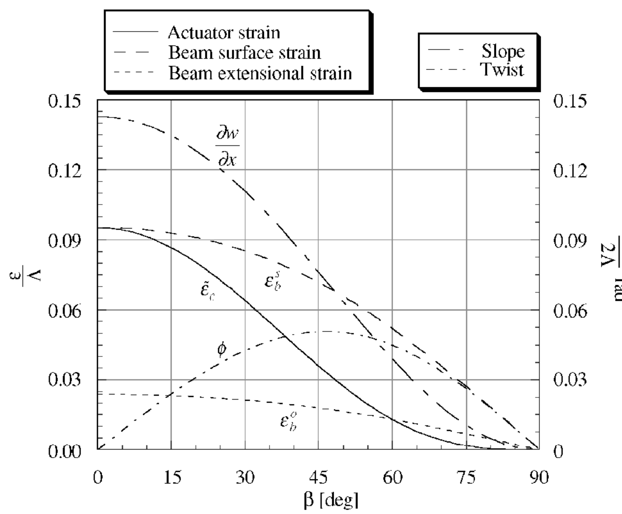

Fig. 21 Analytical strains and deflections (ψ_b = 38) (Ref. 83).

E. Extension-Bending-Torsion Model (Skewed Piezo)

If a slender actuator is oriented at an angle with respect to the beam axes (Fig. 20), it results in a coupled extensional, bending, and torsion response. Despite two-dimensional local induced strain distribution, the large-aspect-ratio actuator primarily acts along its major axis because of dominant shear lag effects in the lateral direction. If two identical actuators are oriented at $\pm\beta$ deg at the top and bottom surfaces, respectively, the same potential will induce pure twisting, whereas an opposite potential will cause pure bending. For the maximum induced twist the piezos should be oriented at ± 45 deg, respectively, on the top and bottom surfaces. Park et al.[83] and Park and Chopra[84] developed uniform-strain and Bernoulli–Euler beam models for an isotropic beam with a surface-bonded single piezoceramic actuator at an arbitrary orientation with respect to the beam axis. The shear lag effects as a result of a finite thickness of adhesive layer were included. The actuator was assumed to be a line element and only permitted to induce strain in its lengthwise direction.

Using the uniform-strain theory, an expression for beam twist ϕ with a single actuator oriented at angle β is obtained as[83]

$$\frac{\phi}{\Lambda}(\bar{x}) = \frac{3}{4}\frac{l_c}{t_b}\frac{E_b}{G_b}\frac{\cos(\beta)\sin(\beta)}{\psi + \alpha\cos^3(\beta)}\left[\frac{\sinh(\Gamma\bar{x}) + \sinh(\Gamma)}{\Gamma\cosh(\Gamma)} - (\bar{x} + 1)\right]$$

where G_b is the shear modulus of beam. Figure 21 shows variation of strains with skew angle. The maximum twist that occurs for β equals 45 deg.

F. Shear-Based (d_{15}) Piezoelectric Actuation

There have been a few selected works on shear actuation, where piezoelectric actuators are normally poled in longitudinal direction and subjected to transverse electric field. As a result, the actuator undergoes shear deformation through d_{15} effect. Theoretical analyses of beams with surface-bonded shear actuators have been developed by Trindade et al.,[87] Benjeddou et al.,[88,89] Zhang and Sun,[90] and Cai and Gao.[91] It appears that the shear actuation mechanism is better suited for active damping control.

G. Validation of Beam Theories

Experimentation was performed on rectangular aluminum beams with surface-bonded G-1195 piezoceramic actuators to validate the beam theories.[81,83,84] Crawley and de Luis[81] previously correlated the analysis for a pair of piezoelements surface bonded to an aluminum beam. In Ref. 83 static tests were performed to validate bending results for a pair of piezos with different width ratios, a single piezo aligned with the beam axis, and a single piezo not aligned with the beam axis. A necessary ingredient for the analysis is the free piezostrain as a function of the applied electric field (see Fig. 22 for G-1195 material). Strain data for an unconstrained piezoceramic element were obtained vs applied voltage and zeroed for each data point. This was done in order to minimize the effects of hysteresis and creep.

The test specimens were $\frac{1}{16}$ and $\frac{1}{32}$ in. thick 2×16 in. aluminum beams (1 in. = 25.4 mm) with 9.5 mil G-1195 piezoceramic elements. Configurations included actuators that spanned the full width and half-width of the beam. The piezoceramics were bonded to the specimens using a cynoacrylate adhesive to minimize the bond layer effects. Bending slope and twist data were obtained by measuring the relative horizontal travel of a laser beam reflected off a mirror at the tip of the beam. Predictions for bending slope show good agreement with test data in Fig. 23.

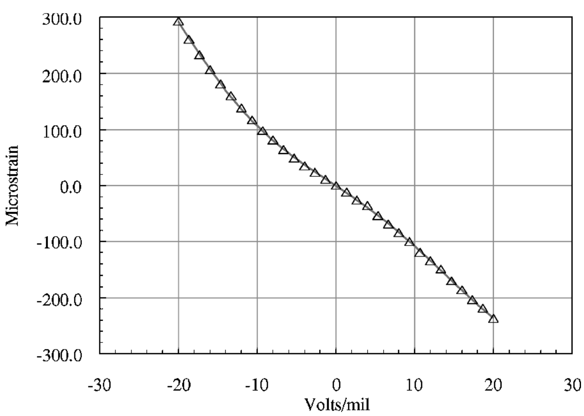

Fig. 22 G-1195 piezoceramic element free behavior.[83]

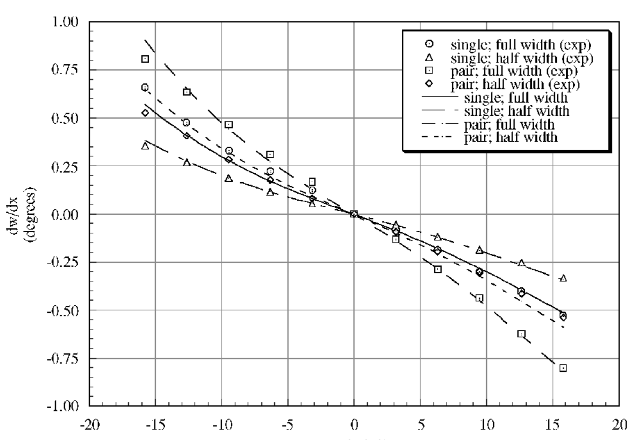

Fig. 23 Bending slope test data and predictions for $\frac{1}{32}$-in. (0.79-mm)-thick aluminum beam.[83]

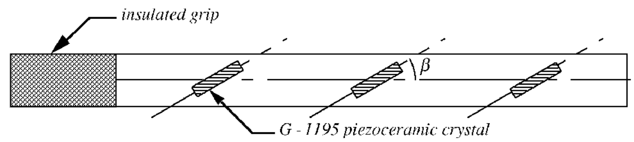

Fig. 24 Typical torsion test specimen.

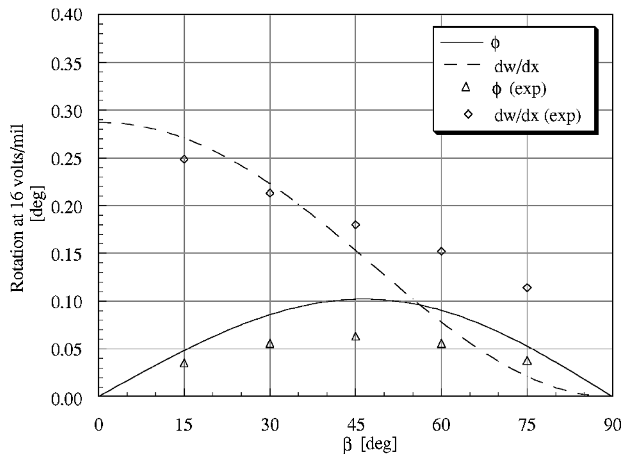

Fig. 25 Effects of actuator orientation on beam bending slope and twist angle ψ_b = 38; ψ_s = 0.0020 (Ref. 82).

Experimental torsion and bending results for cantilevered beams with actuators bonded to one surface and oriented with an angle β relative to the beam axis (Fig. 24) were compared with analytical predictions from the combined extension-bending-torsion uniform strain model.[84] The test specimens were for $\frac{1}{32}$-in. thick aluminum beams with three 2 in. $\times$ $\frac{1}{4}$ in. $\times$ 7.5 mil G-1195 piezoceramic elements distributed along the 16-in. beam in 4-in. intervals. Because actuators of aspect ratio eight were used to approximate the theoretical line element assumption, three piezos were required to obtain measurable deflections using optical measurement system. Superposition of the analytical results is assumed for comparison with the experiment and independently verified for the piezospacing.

As shown in Fig. 25, the bending slope predictions are within 20% of the experimental values up to $\beta = 45$ deg. Beyond this point the theory significantly diverges from the test results. The torsion analytical results follow the experimental trend over the full range of β but overpredict the experimental magnitude by 35–100% in the midrange ($15 < \beta < 75$). Beam torsion and bending are adequately modeled one-dimensionally, but the mechanism that produces twist in this system is inherently two-dimensional. The primary source of discrepancy can be attributed to the one-dimensional approximation of the strain state. Effects of chordwise and lateral bending have been neglected and might constitute significant error depending upon the beam cross-section aspect ratio. Overall, the results indicate that a one-dimensional model is not satisfactory to predict combined torsion, bending, and extension of beams with surface bonded induced strain actuators.

To assess the effect of bond thickness on actuator performance, simple beam specimens were built and tested under a static field.[92] The bond thickness was varied from 0.0025 in. (close to perfect bond condition) to 0.02 in. (not too abnormal), and the orientation of actuators was varied from 0 (aligned with beam axis) to 65 deg. Also, uniform-strain beam theory for embedded skewed actuators including effect of bond layer was developed and compared with test data. The effect of reducing the bond thickness can be seen in Fig. 26. The maximal torsional and bending deflections increased by 60 and 90% respectively when the bond thickness was reduced from 0.020 to 0.0025 in. A minimal bond layer thickness results in the most efficient shear transfer, which in turn results in maximum torsional and bending response. An optimum blade twist actuation will result for perfectly bonded actuators oriented at skew angles of ± 45 deg.

Table 4 Comparison of smart beam models

Modeling type	Actuator	Piezoelectric coupling	Beam type	Validation	Reference
Block force	Surface and embedded	Uncoupled	Isotropic	——	——
Euler–Bernoulli	Surface and embedded Straight patches	Uncoupled	Isotropic	Cantilevered aluminum	Crawley and de Luis[81] Park et al.[83]
	Skewed patches		Isotropic	Cantilevered aluminum	Park et al.[83] Park and Chopra[84]
Uniform strain	Surface and embedded Straight patches	Uncoupled	Isotropic	Cantilevered aluminum	Crawley and de Luis[81] Park et al.[83]
	Skewed patches		Isotropic	Cantilevered aluminum	Park et al.[83] Park and Chopra[84]
Timoshenko (FSDT)	Surface and embedded	Uncoupled	Isotropic	——	Shen[108]
Vlasov with chordwise bend and Shear	Surface-bonded Straight patched	Uncoupled	Isotropic and composite	Cantilevered composite coupled	Chandra and Chopra[102] Bernhard and Chopra[106]
Euler–Bernoulli coupled	Surface	Coupled	Isotropic	Cantilevered aluminum	Hagood et al.[94]
LWSD theory	Surface	Coupled	Isotropic and composite	——	Robbins and Reddy[110] Saravanos and Heyliger[111]

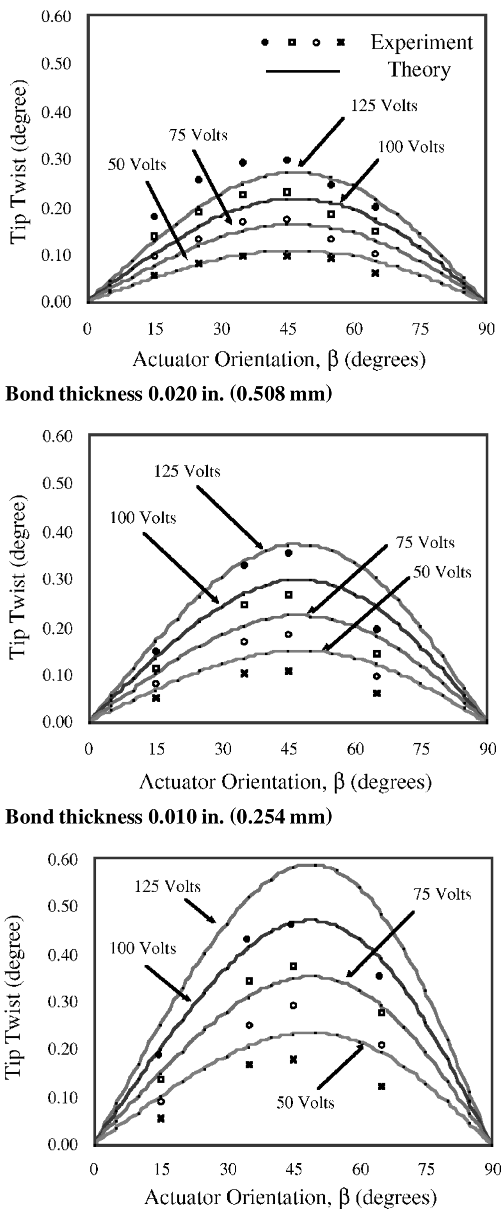

Fig. 26 Effect of bond thickness and actuator orientation on cantilevered beam tip twist.[92]

The preceding subsections examined several one-dimensional structural models that can predict the behavior of different beam configurations with induced strain actuators. Modeling of shear lag effects of the finite bond layer appears important especially for beams with thick and/or soft bond layer. The single actuator uniform-strain model governing equations can be also formulated using an energy approach that can be easily adapted to dynamic systems. A one-dimensional treatment of a strain actuated beam in coupled extension, bending, and torsion was shown to be inadequate to predict its structural behavior. Because the torsion trend is predicted, analytical accuracy can be improved by integrating a local two-dimensional model of the actuation mechanism with a global one-dimensional system model.

H. Assessment of Beam Theories

Table 4 lists different smart beam models. Crawley and de Luis[81] formulated the uniform-strain model for a beam with surface-bonded piezoceramic actuators (patched and aligned with beam axis). The model calculated flexural response including shear lag effects of the adhesive layer between the piezoceramic and the beam. It was shown that the strain transfer from the piezoelectric to the substructure takes place over a small zone near the ends of actuator and there is maximum shear stress in this region. As the adhesive layer becomes thinner and/or stiffer (shear modulus), it approaches a perfect bond condition (shear concentrated at two ends of actuator). The dynamic model was experimentally verified for the first two bending modes of a cantilevered aluminum beam. They also presented a uniform-strain model for an isotropic beam with embedded actuators and satisfactorily validated the dynamic response at resonance for aluminum, glass-epoxy and graphite-epoxy beams. Im and Atluri[93] developed a nonlinear analysis of a piezoactuated beam with finite thickness bond layer including the effects of transverse shear and axial forces in addition to the bending moment on the beam. Again, it was shown that the maximum shear stress occurs near the two ends of the piezoelectric element and is also a function of externally applied axial and shears forces. Crawley and Anderson[82] formulated the Euler–Bernoulli model for a beam with surface-bonded or embedded induced strain actuators (symmetric actuation) and compared it with a uniform-strain model, a finite element model, and an experiment. For the uniform beam theory a uniform shear stress is assumed through the thickness of the adhesive, and a uniform axial stress is assumed though the thickness of the actuator. In spite of these gross assumptions, the uniform strain model was generally found satisfactory except for low beam-to-actuator-thickness ratios (<4). The Bernoulli–Euler model was quite satisfactory to predict bending and extensional response even for low thickness ratios. There is no doubt that for thickness ratio of one or less (such as the case with bimorphs) a refined model including three-dimensional effects might be needed. The linear model (using linear piezoelectric characteristics) is accurate only for small strains. To predict reliable flexural results with high field conditions, nonlinear field-strains relations should be included. The preceding analyses neglected the coupling of piezoelectrics on mechanical properties (uncoupled analyses). Hagood et al.[94] formulated a completely coupled piezoelectric-mechanical model for a beam with surface-bonded actuators. Predicted dynamics were found to be in good agreement with experimental data obtained with a cantilevered aluminum beam. Park et al.[83] developed coupled bending and extension analysis for an isotropic beam with isolated surface bonded actuator. A finite thickness adhesive layer between actuator and beam was included. The convergence point of the Bernoulli–Euler and uniform-strain predictions was shown to be a function of beam-to-actuator-width ratio in addition to thickness ratio. Satisfactory validation of predicted bending slope with measured values was carried out for several different aluminum beams. Benjeddou et al.[88] developed a unified beam finite element model for extension and shear piezoelectric actuation mechanism. This is especially suitable for sandwiched beams. The model used Bernoulli–Euler theory for the surface layers and Timoshenko beam theory for the core. It was shown that the predicted induced deformation was lower with the shear-actuated beam theory.

Park and Chopra[84] developed coupled extension, bending, and torsion analysis for an isotropic beam with surface-bonded actuators at an arbitrary orientation with respect to the beam axis. Piezoceramic actuators were represented as line actuators. Systematic experimental tests with cantilevered aluminum beams were carried out for induced bending and twist at different orientation angles to check the accuracy and limitation of models. Comparison of predicted results with test data showed that the models were satisfactory in predicting trends for bending slope and twist with different orientation angle. The predicted bending slope deviated significantly from measured value for orientation angles greater than 45 deg (Fig. 25), more so for piezoceramics with moderate aspect ratios. Detailed strain measurements showed that the local strains are quite two-dimensional. Therefore, the inclusion of effects of transverse actuation might be necessary to refine the analysis.

Jung et al.[95,96] made an assessment of the state of the art in modeling of thin- and thick-walled composite beams with a view to emphasize the special characteristics of composite materials. The review encompasses modeling nonclassical effects such as out-of-plane warping, warping restraints, and transverse shear. Composite beam modeling ranges from simple analytical models to detailed finite element models and has been validated using limited test data from simple tailored specimen.[97–101] The anisotropic nature of composite materials makes the structural properties direction dependent. Using special ply layup, structural couplings such as bending-torsion and extension-torsion can be introduced. These couplings can be exploited with induced strain actuation to actively control aerodynamic shape such as in helicopter blades or an airplane. In modeling of a composite beam with induced stain actuation as a one-dimensional structure, it is important to encompass all of the important effects caused by bending and shear deflections and twist of reference axis of the beam and warping deformations of the cross section. Normally, the warping deformations are much smaller than the flexural deformations. This helps to simplify the complexity of inherently three-dimensional problem into two parts: a two-dimensional local deformation field of the cross section that is used to calculate the section properties and a one-dimensional global deformation field to predict the response of the beam. The first level of idealization of the global deformation includes the Bernoulli–Euler model for bending and the St. Venant model for torsion. In the next levels torsion-related warping, transverse shear strain, and cross-section deformation (in-plane warping) effects are included. For composite thin-walled beams it is possible to model the shell wall either as a membrane or as a thick laminate including the effect of transverse shear as well as bending distribution. Chandra and Chopra[102] developed a formulation for coupled composite thin-walled open- and closed-section beams with distributed induced strain actuation (surface-mounted or embedded) and then validated the analysis with experimental data. Beam modeling was based on Vlasov theory, where two-dimensional stress and strain distributions associated with any local plate (shell) element of the beam are reduced to one-dimensional generalized forces and moments. Effects of transverse shear and warping restraints were included. Comparison with experimental data from bending-twist and extension-twist coupled graphite-epoxy composite solid beams with surface-mounted piezoceramic actuators showed that the inclusion of chordwise (lateral) bending is essential to predict a beam's coupled response accurately. Also, Kaiser[103] carried out a similar type of study with thin-walled, open- and closed-section, coupled composite beams with piezoelectric actuation. Cesnik and Shin[104] developed a refined multicell composite beam analysis for active twist rotor with embedded AFC actuators. The approach is based on a two-step asymptotic solution: a linear two-dimensional cross-sectional analysis and a global nonlinear one-dimensional analysis. Subsequently, the analysis was successfully validated with test data for different blade configurations and load conditions.[105] Ghiringhelli et al.[86] developed a refined finite element analysis for anisotropic beam with embedded piezoelectric actuators and successfully compared their results with three-dimensional results. As a part of smart-tip rotor development, Bernhard and Chopra[106] developed Vlasov-type beam analysis for a tailored composite coupled beam with induced strain actuation. It consisted of a number of spanwise segments with reversed bending-twist couplings for each successive segment. Each segment acts like a bimorph, and the polarity of successive surface-bonded piezoceramics is reversed. Because of the flip-flopping excitation, the beam deflects into a sinusoidal bending wave, whereas the induced twist is additive spanwise. Predictions were validated satisfactorily with test data for several different beam configurations. For accurate predictions it became necessary to include nonlinear measured characteristics of piezoceramics and modeling of chordwise bending. It is now well established that effects of transverse shear can be very important at both local and global level for the response of composite beams because of low values of shear modulus G compared with the direct modulus E (G/E ratio). A first-order shear deformation method is Timoshenko's model, which assumes a constant shear stress across the cross section. This is called first-order shear deformation theory (FSDT).[107,108] This model, however, violates the traction-free boundary condition on the top and bottom surfaces. To compensate this anomaly, a shear correction factor is applied. To capture the nonlinear distribution of transverse shear strain across the cross section, higher-order shear deformation theories (HSDT) are used. These theories however are unable to capture accurately a dramatic change of properties at a local ply level. A further refinement to HSDT is to use layer-wise shear deformation theory (LWSDT),[109] which models shear distribution for each layer separately. Robbins and Reddy[110] carried out static and dynamic analysis of piezoelectrically actuated beams using LWSDT. Saravanos and Heyliger[111] developed coupled layer-wise analysis of composite beams with embedded piezoelectric actuators and sensors. It was shown that consistent and more detailed stress distributions especially near the end of the actuator are obtained with layer-wise theory. For prediction of higher modes of vibration and/or thicker composite structures, it might be more appropriate to use layer-wise theory.

It is clear from testing of simple isotropic beams with surface-attached piezoelectric elements that the local strain distribution (at or near the actuator) is two-dimensional,[84] and, therefore, beam modeling with induced strain actuation should reflect such a distribution. Simple beam theories often give erroneous results for beams with low actuator-to-beam-thickness ratio (such as the case with piezo-bimorphs). Detailed three-dimensional models [say, finite element method (FEM) models] should be used to establish the strain actuation mechanism. Most beam theories have either neglected the shearing effect of bond layer (by assuming perfect bond condition) or have incorporated a highly approximate shear model (for example, uniform shear stress within bond thickness); however, test results[92] showed that the bond thickness has a dominant effect on the induced strain transfer from the actuator to beam. It should be important to examine systematically the shearing effect of bond layer using a higher-order shear deformation theory such as LWSDT and establish the limits of simple beam models (uniform-strain and Bernoulli–Euler models). There have been only limited studies on the validation of predictions for composite coupled beams with surface-attached or embedded piezoceramics; these should be expanded to cover more beam configurations and tailored couplings for static and dynamic loads. Such studies can be very important for shape control of aerospace systems. Most predictions have incorporated linear piezoelectric characteristics that are strictly true for low field conditions. To cover moderate to high electric fields, it is worthwhile to include nonlinear characteristics of piezoelectrics. It will be important to examine systematically the effect of piezoelectric-mechanical couplings on actuation strain for a range of isotropic and laminated beams.

IV. Modeling: Plate with Induced Strain Actuation

One of the basic elements of adaptive structures is a thin composite plate with surface-induced or embedded sheet actuators. With a tailored laminated plate, induced strain actuation can control its extension, bending, and twisting. Plates with distributed induced strain actuators can be used to control pointing of precision instruments in space; to control structural borne noise; and to change aerodynamic shape for vibration reduction, flutter suppression, and gust alleviation.

Several plate theories have been developed to predict flexural response of laminated plates with surface-bonded or embedded induced strain actuators that include classical laminated plate theory (CLPT), FSDT, HSDT, and LWSDT. All of these theories assume that the actuators and substrate are integrated as plies of a laminated plate undergoing consistent deformation. They, however, differ from each other in terms of displacement distribution through the thickness of plate (modeling of transverse shear).

Among these plate theories, the CLPT is most widely used. It is based on the Kirchoff–Love hypothesis that is quite similar to the Bernoulli–Euler beam theory. It assumes a linear variation of bending strain across thickness, and the effects of transverse shear are neglected. (A line originally normal to midplane of plate remains normal to midplane after bending deformation.) It implies a perfect bonded condition between actuators and substrate. This theory is truly applicable for thin plates (length/thickness > 30), where transverse shear effects are negligible.

The constitutive relation for any ply of a laminated plate is

$$\boldsymbol{\sigma} = \bar{Q}(\varepsilon - \Lambda)$$

where stress vector

$$\boldsymbol{\sigma} = \begin{Bmatrix} \sigma_x \\ \sigma_y \\ \tau_{xy} \end{Bmatrix}$$

For a generic coupled laminated plate with surface-bonded or embedded induced strain actuators (piezoceramic sheets) placed at arbitrary locations, the strain distribution is expressed as

$$\epsilon = \epsilon^0 + z\kappa$$

where ϵ^0 is the midplane strain and κ is the bending curvature. Coordinates x and y are in the in-plane directions, and z represents the out-of-plane direction (Fig. 27). The u, v, and w are displacements

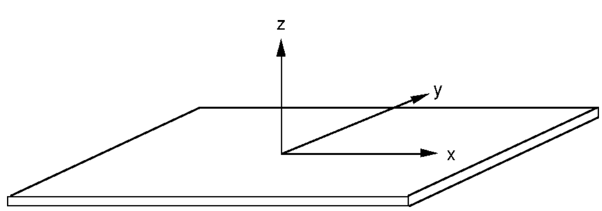

Fig. 27 Plate coordinate system.

in the x, y, and z directions. The strains are defined as

$$\varepsilon^0 = \begin{Bmatrix} \varepsilon_x^0 \\ \varepsilon_y^0 \\ \varepsilon_{xy}^0 \end{Bmatrix} = \begin{Bmatrix} \dfrac{\partial u}{\partial x} \\ \dfrac{\partial v}{\partial y} \\ \dfrac{\partial u}{\partial y} + \dfrac{\partial v}{\partial x} \end{Bmatrix}$$

$$\boldsymbol{\kappa} = \begin{Bmatrix} \kappa_x \\ \kappa_y \\ \kappa_{xy} \end{Bmatrix} = \begin{Bmatrix} \dfrac{-\partial^2 w}{\partial x^2} \\ \dfrac{-\partial^2 w}{\partial y^2} \\ -2\dfrac{\partial^2 w}{\partial x \partial y} \end{Bmatrix}$$

and actuation strain vector

$$\boldsymbol{\Lambda} = \begin{Bmatrix} \Lambda_x \\ \Lambda_y \\ \Lambda_{xy} \end{Bmatrix}$$

Matrix $\bar{Q}$ is the transformed reduced stiffness of the plate. By substituting the assumed deformation into the stress strain equations and integrating through the thickness t of plate with N plies for net forces and moments,

$$\begin{Bmatrix} N_x \\ N_y \\ N_{xy} \\ M_x \\ M_y \\ M_{xy} \end{Bmatrix} = \begin{bmatrix} \begin{bmatrix} A_{11} & A_{12} & A_{16} \\ A_{12} & A_{22} & A_{26} \\ A_{16} & A_{26} & A_{66} \end{bmatrix} & \begin{bmatrix} B_{11} & B_{12} & B_{16} \\ B_{12} & B_{22} & B_{26} \\ B_{16} & B_{26} & B_{66} \end{bmatrix} \\ \begin{bmatrix} B_{11} & B_{12} & B_{16} \\ B_{12} & B_{22} & B_{26} \\ B_{16} & B_{26} & B_{66} \end{bmatrix} & \begin{bmatrix} D_{11} & D_{12} & D_{16} \\ D_{12} & D_{22} & D_{26} \\ D_{16} & D_{26} & D_{66} \end{bmatrix} \end{bmatrix}$$

$$\times \begin{Bmatrix} \varepsilon_x^0 \\ \varepsilon_y^0 \\ \gamma_{xy}^0 \\ \kappa_x \\ \kappa_y \\ \kappa_{xy} \end{Bmatrix} - \begin{Bmatrix} N_{x_\Lambda} \\ N_{y_\Lambda} \\ N_{xy_\Lambda} \\ M_{x_\Lambda} \\ M_{y_\Lambda} \\ M_{xy_\Lambda} \end{Bmatrix}$$

where extensional stiffness

$$A = \int_t \bar{Q}\,\mathrm{d}z, \qquad A_{ij} = \sum_{k=1}^{N} (\bar{Q}_{ij})_k (h_k - h_{k-1})$$

coupling stiffness

$$B = \int_t \bar{Q}z\,\mathrm{d}z, \qquad B_{ij} = \sum_{k=1}^{N} (\bar{Q}_{ij})_k \left(\frac{h_k^2 - h_{k-1}^2}{2} \right)$$

bending stiffness

$$D = \int \bar{Q}z^2\,\mathrm{d}z, \qquad D_{ij} = \sum_{k=1}^{N} (\bar{Q}_{ij})_k \left(\frac{h_k^3 - h_{k-1}^3}{3} \right)$$

actuator forces and moments

$$N_\Lambda = \int_t Q\Lambda\,\mathrm{d}z, \qquad M_\Lambda = \int_t Q\Lambda z\,\mathrm{d}z$$

A. Symmetric Laminates

These are laminates with ply layups that are symmetric with respect to the midplane. Coupling stiffness terms B_{ij} become identically zero, and bending and actuation equations become uncoupled.

Extensional actuation is

$$\begin{bmatrix} A_{11} & A_{12} & A_{16} \\ A_{12} & A_{22} & A_{26} \\ A_{16} & A_{26} & A_{66} \end{bmatrix} \begin{Bmatrix} \varepsilon_x^0 \\ \varepsilon_y^0 \\ \gamma_{xy}^0 \end{Bmatrix} = \begin{Bmatrix} N_{x_\Lambda} \\ N_{y_\Lambda} \\ N_{xy_\Lambda} \end{Bmatrix}$$

where

$$\begin{Bmatrix} N_{x_\Lambda} \\ N_{y_\Lambda} \\ N_{xy_\Lambda} \end{Bmatrix} = \frac{2E_c t_c \Lambda}{1-\nu} \begin{Bmatrix} 1 \\ 1 \\ 0 \end{Bmatrix}$$

There is no induced shearing strain.

Bending actuation is

$$\begin{bmatrix} D_{11} & D_{12} & D_{16} \\ D_{12} & D_{22} & D_{26} \\ D_{16} & D_{26} & D_{66} \end{bmatrix} \begin{Bmatrix} \kappa_x \\ \kappa_y \\ \kappa_{xy} \end{Bmatrix} = \begin{Bmatrix} M_{x_\Lambda} \\ M_{y_\Lambda} \\ M_{xy_\Lambda} \end{Bmatrix}$$

where

$$\begin{Bmatrix} M_{x_\Lambda} \\ M_{y_\Lambda} \\ M_{xy_\Lambda} \end{Bmatrix} = \frac{E_c t_c (t_b + t_c)\Lambda}{1-\nu} \begin{Bmatrix} 1 \\ 1 \\ 0 \end{Bmatrix}$$

There is no direct twisting moment with piezos. There are however extension-shear and bending-twist couplings with symmetric laminates.

B. Antisymmetric Laminates

These are laminates with ply layups that are antisymmetric with respect to midplane. Behavior of such laminates can be significantly different from that of symmetric laminates. For an antisymmetric laminate, the extensional-shear couplings and bending-twist couplings are zero. There are, however, extension-twist couplings and bending-shear coupling with antisymmetric laminates.

Extensional actuation is

$$\begin{bmatrix} A_{11} & A_{12} & 0 \\ A_{12} & A_{22} & 0 \\ 0 & 0 & A_{66} \end{bmatrix} \begin{Bmatrix} \varepsilon_x^0 \\ \varepsilon_y^0 \\ \gamma_{xy}^0 \end{Bmatrix} + \begin{bmatrix} 0 & 0 & B_{16} \\ 0 & 0 & B_{26} \\ B_{16} & B_{26} & 0 \end{bmatrix} \begin{Bmatrix} \kappa_x \\ \kappa_y \\ \kappa_{xy} \end{Bmatrix} = \begin{Bmatrix} N_{x_\Lambda} \\ N_{y_\Lambda} \\ N_{xy_\Lambda} \end{Bmatrix}$$

Bending actuation is

$$\begin{bmatrix} 0 & 0 & B_{16} \\ 0 & 0 & B_{26} \\ B_{16} & B_{26} & 0 \end{bmatrix} \begin{Bmatrix} \varepsilon_x^0 \\ \varepsilon_y^0 \\ \gamma_{xy}^0 \end{Bmatrix} + \begin{bmatrix} D_{11} & D_{12} & 0 \\ D_{12} & D_{22} & 0 \\ 0 & 0 & D_{66} \end{bmatrix} \begin{Bmatrix} \kappa_x \\ \kappa_y \\ \kappa_{xy} \end{Bmatrix} = \begin{Bmatrix} M_{x_\Lambda} \\ M_{y_\Lambda} \\ M_{xy_\Lambda} \end{Bmatrix}$$

C. Approximate Solution (Energy Approach)

For many problems it is not possible to obtain an exact solution. Thus, it becomes necessary to obtain an approximate solution using an energy approach such as the Rayleigh–Ritz method. The strain energy of the system is

$$U = \frac{1}{2}\iint_A \begin{Bmatrix} \varepsilon^{0^T} & \kappa^T \end{Bmatrix} \begin{bmatrix} A & B \\ B & D \end{bmatrix} \begin{Bmatrix} \varepsilon^0 \\ \kappa \end{Bmatrix} \mathrm{d}A - \iint_A [N_\Lambda M_\Lambda] \begin{Bmatrix} \varepsilon^0 \\ \kappa \end{Bmatrix} \mathrm{d}A$$

where

$$\begin{Bmatrix} \varepsilon^0 \\ \kappa \end{Bmatrix} = [\boldsymbol{D}] \begin{Bmatrix} u \\ \sim \end{Bmatrix} = \begin{bmatrix} \frac{\partial}{\partial x} & 0 & 0 \\ 0 & \frac{\partial}{\partial y} & 0 \\ \frac{\partial}{\partial y} & \frac{\partial}{\partial x} & 0 \\ 0 & 0 & -\frac{\partial^2}{\partial x^2} \\ 0 & 0 & -\frac{\partial^2}{\partial y^2} \\ 0 & 0 & -\frac{2\partial^2}{\partial x \partial y} \end{bmatrix} \begin{Bmatrix} u \\ v \\ w \end{Bmatrix}$$

The Rayleigh–Ritz approximate solution is

$$u = \sum_{i=1}^{M} \phi_{u_i} q_i, \qquad v = \sum_{j=1}^{N} \phi_{v_j} q_{j+M}$$

$$w = \sum_{k=1}^{P} \phi_{w_k} q_{k+M+N}, \qquad \begin{bmatrix} u \\ v \\ w \end{bmatrix} = [H]q$$

where

$$H = \begin{bmatrix} [\phi_{u_1}, \phi_{u_2} - \phi_{u_M}] & [0] & [0] \\ [0] & [\phi_{v_1}, \phi_{v_2} - \phi_{v_N}] & [0] \\ [0] & [0] & [\phi_{w_1}, \phi_{w_2} - \phi_{w_P}] \end{bmatrix}_{3\times r}$$

where

$$r = M + N + P, \qquad \begin{bmatrix} \varepsilon^0 \\ \kappa \end{bmatrix} = [\boldsymbol{D}][H]q$$

Substitution in strain energy reduces to

$$U = \tfrac{1}{2} q^T K q - Q_\Lambda q K q = Q_\Lambda$$

where

$$K = \iint_A (DH)^T \begin{bmatrix} A & B \\ B & D \end{bmatrix} (DH)\,\mathrm{d}A$$

$$Q_\Lambda = \iint_A (DH)^T \begin{Bmatrix} N_\Lambda \\ M_\Lambda \end{Bmatrix} \mathrm{d}A$$

The matrix K is of size $r \times r$, and the actuation-forcing matrix Q_Λ is of size $r \times 1$.

Applying Lagrange's equation, it is possible to solve for modal amplitudes:

$$Kq = Q_\Lambda$$

For more details, see Refs. 112 and 113.

Let us consider a cantilevered rectangular composite plate (length L and chord c) with two surface-mounted piezoceramic sheets. Assume a simple three-term solution:

$$u = (x/L)q_1, \qquad v = 0, \qquad w = (x/L)^2 q_2 + (x/L)(y/c)q_3$$

This results in

$$\begin{bmatrix} A_{11} & -\frac{2}{L}B_{11} & -\frac{2}{c}B_{16} \\ -\frac{2}{L}B_{11} & \frac{4}{L^2}D_{11} & \frac{4}{cL}D_{16} \\ -\frac{2}{c}B_{16} & \frac{4}{cL}D_{16} & \frac{4}{c^2}D_{66} \end{bmatrix} \begin{Bmatrix} q_1 \\ q_2 \\ q_3 \end{Bmatrix} = \begin{Bmatrix} N_{x_\Lambda} L \\ -2M_{x_\Lambda} \\ 0 \end{Bmatrix}$$

Table 5 Comparison of smart plate models

Plate theory	Actuators	Piezoelectric coupling	Plate type	Validation with test data	References
CLPT	Surface-bonded full surface	Uncoupled	Composite, nonlinear piezochar.	Cantilevered aluminum and composite	Crawley and Lazarus[112]
	Surface-bonded patches	Uncoupled	Composite, linear piezochar.	Cantilevered composite	Lee[114]
Modified CLPT with transverse shear	Surface and embedded Dicrete patches	Uncoupled	Composite, nonlinear piezochar.	Cantilevered composite	Hong and Chopra[113]
Reissner–Mindlin FSDT	Surface and embedded Dicrete patches	Coupled	Nonlinear Karman analysis, thick isotropic	——	Carrera[124]
LWSD theory	Surface and embedded Piezoply	Coupled	Isotropic and composite	——	Mitchell and Reddy[129] Robbins and Reddy[130] Chattopadhyay et al.[131] Zhou et al.[132]
Higher-order (kth-order) three-dimensional thick plate theory	Surface and embedded Piezoply	Coupled	Isotropic, thick	——	Sun and Whitney[128] Batra and Vidoli[135] Ha et al.[136]

For a symmetric plate with bending-torsion coupling ($B_{11} = B_{16} = 0$),

$$q_3 = \frac{cL}{2}\frac{D_{16}}{D_{11}D_{66} - D_{16}^2}\frac{2D_{16}}{cL}M_{x_\Lambda}$$

This shows that induced twist is caused by bending actuation (opposite field on top and bottom piezos), and it depends on the ratio of the coupling stiffness D_{16} to the bending stiffness D_{66} times D_{11}.

Bending-twist coupling $\psi_T = D_{16}/\sqrt{(D_{11}D_{16})}$. For an antisymmetric composite plate with extension-torsion coupling ($B_{11} = 0$ and $D_{16} = 0$),

$$q_3 = \frac{1}{2}cL\left[\frac{B_{16}}{A_{11}D_{66} - B_{16}^2}\right]N_{x_\Lambda}L$$

This shows that induced twist in an antisymmetric plate is caused by extensional actuation (same field on top and bottom piezos), and it depends on the ratio of coupling stiffness B_{16} to the extensional stiffness A_{11} times torsional stiffness D_{66}. The extension-twist coupling parameter is

$$\psi_B = \frac{B_{16}}{\sqrt{A_{11}D_{66}}}$$

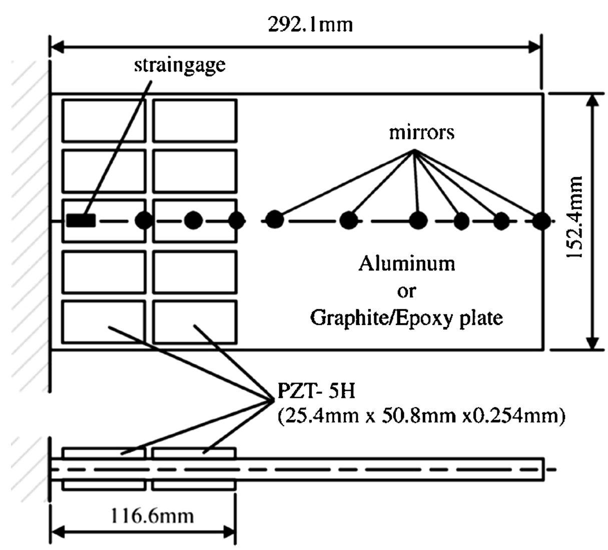

Fig. 28 Cantilevered plate with surface-mounted piezoceramics.[113]

D. Review of Plate Modeling

Table 5 lists different smart plate models. Crawley and Lazarus[112] systematically developed the CLPT formulation and a Rayleigh–Ritz analysis for anisotropic plates and validated it with test data obtained by testing cantilevered aluminum and composite plates with surface-bonded piezoceramic actuators (attached at top and bottom surfaces fully). Nonlinear piezo characteristics (d_{31} with field) were measured experimentally and included in analysis using an iterative approach. Results demonstrated the validity of analysis for selected plate configurations and showed the potential for shape control with induced strain actuation. Also, Lee[114,115] developed a CLPT formulation for a composite plate using linear actuation characteristics of piezoelectric laminas. A limited validation study was carried out with test data obtained from a thin composite plate actuated with piezoelectric polymer film (PVDF and PVF2). Wang and Rogers[116] applied CLPT to determine the equivalent force and moment induced by finite-length surface-attached piezoelectric actuator to a laminate. They used linear characteristics of piezoelectrics and developed a simplified analysis to calculate bending and extension of the plate. Hong and Chopra[113] developed a consistent finite element formulation for coupled composite plates including modeling of transverse shear and nonlinear piezoelectric characteristics. The analysis is applicable to a generic anisotropic plate with a number of piezoactuators of arbitrary size, surface bonded or embedded at arbitrary locations. Composite cantilevered plates with extension-twist and bending-twist couplings with two rows of surface-bonded piezoceramics on both top and bottom surfaces were tested extensively, and data were used to validate analysis (Fig. 28). Predictions agreed satisfactorily with test data for most configurations, the exception being strongly bending-twist coupled plates, where the predicted induced twist caused by bending was underestimated by 20% (Figs. 29 and 30). The use of an iterative procedure with the incorporation of nonlinear piezoelectric characteristics (as suggested by other researchers) was found to be unnecessary. Heyliger[117] obtained exact solutions for some idealized plate configurations.

For CLPT formulation the transverse shear stiffness of plate is assumed to be infinite. As a result, there is a zero transverse shear strain across the complete thickness. For CLPT the in-plane displacements are caused by rotation of midplane normal. However, with the presence of transverse shear strains the in-plane displacements will get modified as a result of rotations of cross-sectional planes relative to midplanes. For refined plate models different levels of shear modeling are introduced. A generic displacement distribution is

$$u(x, y, z) = u_0(x, y) + z\phi_x(x, y) + z^2\varsigma_x(x, y) + z^3\varphi_x(x, y)$$

$$v(x, y, z) = v_0(x, y) + z\phi_y(x, y) + z^2\varsigma_y(x, y) + z^3\varphi_y(x, y)$$

$$w(x, y, z) = w_0(x, y)$$

where ϕ_x, ϕ_y represent rotations of the cross section and $\varsigma_x, \varsigma_y, \varphi_x, \varphi_y$ correspond to higher-order terms in the Taylor-series

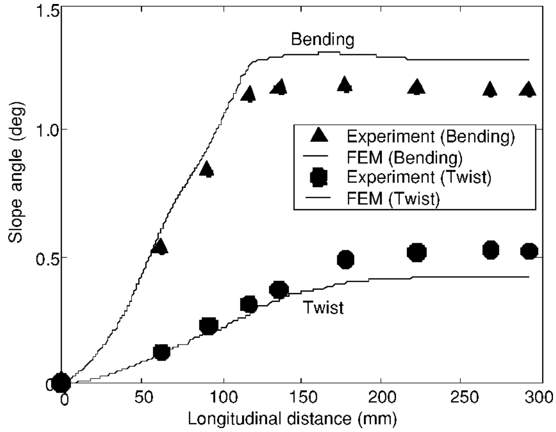

Fig. 29 Longitudinal bending and twist distribution at midchord of a bending-twist coupled $[+30_2/0]_s$ graphite/epoxy plate caused by piezobending excitation at 100 V.[113]

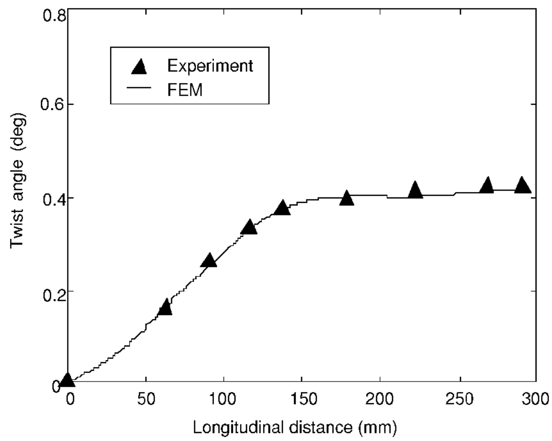

Fig. 30 Twist distribution at midchord of an extension-twist coupled $[+45_3/-45_3]$ graphite/epoxy plate caused by piezoexcitation at 100 V (same voltages to top and bottom piezos).[113]

expansion. The u_0, v_0, and w_0 are midplane displacements. For the CLPT ς_x, ς_y, φ_x, φ_y are assumed to be zero, and ϕ_x, ϕ_y are gradients of out-of-plane displacements. References 118–121 reviewed different plate theories for induced strain actuation. First-order shear deformable-plate theory (FSDT) is based on the Reissner–Mindlin plate model and is quite similar to Timoshenko's beam theory. It relaxes the assumption of the normality of the cross-section plane after deformation. Transverse shear strains are assumed uniform through the thickness of the plate. It fails to account for changes in shear strains caused by the variation of material properties of each layer. For FSDT, ς_x, ς_y, φ_x, φ_y are assumed to be zero, and ϕ_x, ϕ_y are assumed constant through thickness (independent of w_0). This theory estimates lower flexural stiffness than that from the CLPT theory. Another anomaly with this theory is that there is nonzero shear strain at top and bottom free surfaces which violates the physical boundary condition. Normally, a shear correction factor is applied to compensate for nonzero shear strain at free lateral surfaces. Bisegna and Maceri[122] and Bisegna and Carusa[123] developed a Reissner–Mindlin type finite element formulation (locking-free quadrangular elements) for the analysis of a plate with surface-bonded thin piezoelectric sheet actuators. It was shown to be suitable and effective for some vibration-control analyses. Carrera[124] extended the Reissner–Mindlin plate model to the multilayered structures through the inclusion of both the zigzag in-plane displacements and the interlamina equilibrium of transverse shear stresses. The theory is normally denoted by the acronym RMZC (Reissner–Mindlin zigzag continuity). For the calculation of results, a quadratic distribution of the voltage field along the thickness direction and von Kármán-type nonlinear plate analysis were used including the effect of electromechanical coupling. It was shown that RMZC effects become important for thick anisotropic plates, especially in the evaluation of transverse shear stresses.

A higher shear deformable theory (HSDT) developed by Reddy[125] models a general distribution of transverse shear strain through the laminate thickness. For HSDT ς_x, ς_y, φ_x, φ_y are assumed nonzero. This represents a cubic variation of displacements (u, v) through the thickness resulting in a quadratic variation of shear strain. This distribution satisfies the traction-free boundary condition on top and bottom surfaces but lacks accurate representation of layer-wise variation of shear strain caused by different material properties of laminas. In general, it is expected that the HSDT should give a better prediction of flexural stiffness than that with FSDT, but it is not ensured for all plate configurations.[126] To model the variations of material stiffness from layer to layer, it appears appropriate to use layerwise shear deformable theory (LWSDT) attributed to Reddy[127] as well as Sun and Whitney.[128] For this theory the laminate is divided into a number of sublayers that are perfectly bonded, and in each layer the in-plane displacement is assumed piecewise linearly along the z direction. There is a significant increase in degrees of freedom of the model:

$$u^{(k)}(x, y, z) = u_0(x, y) + z\phi_x^{(k)}(x, y)$$
$$v^{(k)}(x, y, z) = v_0(x, y) + z\phi_y^{(k)}(x, y)$$
$$w^{(k)}(x, y, z) = w_0(x, y)$$

where $\phi_x^{(k)}$, $\phi_y^{(k)}$ represent rotations of the cross section of the kth layer. For a case of single layer, LWSDT reduces to FSDT. Even though the shear strain is assumed uniform in each layer, there is a variation from layer to layer. Mitchell and Reddy[129] used LWSDT to model smart composite laminates with embedded piezoelectric sheets using linear piezoelectric characteristics. Also, this model included the coupling between mechanical deformation and electrostatic charge equations. Robbins and Reddy[130] formulated a linear global-local analysis based on layer-wise shear deformation theory to determine local shear fields and global response in surface-mounted piezoelectric actuated plates. Using a variable-order finite element discretization, interlaminar stresses in the adhesive layer were determined. It was shown that the highest transverse normal stress occurs at the interphase between bond layer and beam near the free edges that can be the likely source of debonding. Chattopadhyay et al.[131] and Zhou et al.[132] used LWSDT to calculate static and dynamic response of composite plates with surface-bonded piezoelectric actuators using a completely coupled thermo-piezoelectric-mechanical model. Most researchers have neglected these coupling effects. They have shown that to model the behavior of smart composite laminates accurately, it is important to model transverse shear of each layer using LWSDT and incorporate piezoelectric-mechanical biway coupling effects. Vel and Batra[133] developed a three-dimensional analytical solution using Eshelby–Stroh formalism to calculate static response of thick multilayered piezoelectric plates. Only linear piezoelectric characteristics are incorporated. Using a three-dimensional mixed variational principle,[134] Batra and Vidoli[135] derived higher-order (kth order) anisotropic homogeneous piezoelectric plate theory. The electric potential, mechanical displacement, and in-plane stresses were expressed as a finite series of order k in the thickness coordinate using Legendre polynomials as the basis functions. The boundary conditions on the top and bottom surfaces were exactly satisfied. Results were obtained for bending of cantilevered thick plate with surface-bonded PZT sheets. It was shown that the seventh-order plate theory captured well the boundary-layer effects near the free and clamped edges. Ha et al.[136] used a three-dimensional composite brick element to analyze static and dynamic response of a laminated plate with distributed piezoceramic actuators. Even though such an analysis can increase the computational involvement enormously, it has the flexibility to analyze generic plate configurations including thick plates with surface-bonded or embedded patched actuators.

Most current plate analyses assume a perfect bond condition between actuator and bond surface (that is, neglected shearing effect of adhesive). This assumption is too restrictive and therefore should be examined systematically especially for discrete actuators. Simple plate theories such as CLPT are routinely used to analyze plate structures. It might be important to examine its limits for different plate configurations and actuation fields with the help of either higher order shear deformation theories (such as LWSDT) or detailed FEMs (such as three-dimensional solid elements). There have been limited studies to validate predictions with experimental test data for coupled composite plates with surface-bonded or embedded piezoelectric elements. These should be expanded to cover a range of plate configurations including strongly coupled bending-torsion coupled plates.

V. Shape Memory Alloys

Shape-memory-alloy (SMA) actuators are finding increasing applications in aerospace, civil, mechanical, medical, and other systems. They have a special characteristic of "memorizing" a certain stretched or bent shape and recovering that shape at a higher temperature. Buehler et al.[137] discovered a nickel-titanium alloy in 1961 called NITINOL that exhibited much higher shape memory effects than previous materials. This alloy demonstrates 100% recovery of strain up to a maximum of 8% extensional prestrain, which makes it attractive for use in low-frequency (less than 1 Hz) actuators. SMA actuators have high work density ratios, very high strokes, direct actuation capabilities, and embeddable characteristics. Another interesting feature is a two- to fourfold increase in Young's modulus above the critical phase transition temperature. The phase change is also accompanied by a large change in resistivity and release (or absorption) of latent heat. Restraining the recovering strain results in large recovery stress (several times more than the initial stress required to prestrain at room temperature). These characteristics are exploited to tune the properties of structures for various applications. Figure 31 explains the shape memory effect schematically.

The shape that an SMA memorizes can be assigned or reassigned through an annealing (say, above 500°C). At room temperature the SMA is generally in martensite phase, and its undeformed crystal structure is twinned (less symmetric). In this phase it is easy to move twin boundaries in the direction of applied stress, and thus the material modulus of elasticity and yield stress are very low. Application of extensional stress to the material above its yield stress causes detwinning (change orientation of crystal twins) and hence a plastic deformation. Through an application of heat to this material, the plastic prestrain can be completely recovered. At a high temperature the material is in austenite phase (parent phase), and its crystals result in a right-angle ordered lattice. In the austenite phase it is more difficult to deform the twin boundaries than martensite phase, resulting in a higher yield stress and modulus of elasticity. Figure 32 sketches the shape memory process. Typically, a plastic strain of more than 8% at low temperature (fully detwinned martensite phase) can introduce permanent or irrecoverable plastic strain as a result of the formation of dislocations. If an SMA is constrained with a spring (such as the case with embedding in a host structure), the alloy is prevented from returning to the original shape upon heat activation. This results in the generation of a large recovery stress. On the other hand, if SMA is not constrained there will be no recovery stress (free recovery). For an SMA embedded in a host structure, the recovery stress will decrease on cooling, and if this stress is still higher than martensite

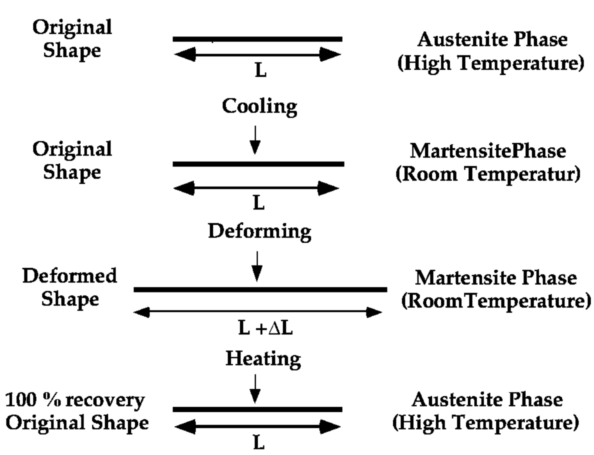

Fig. 31 Schematic of shape memory effect in stretching.

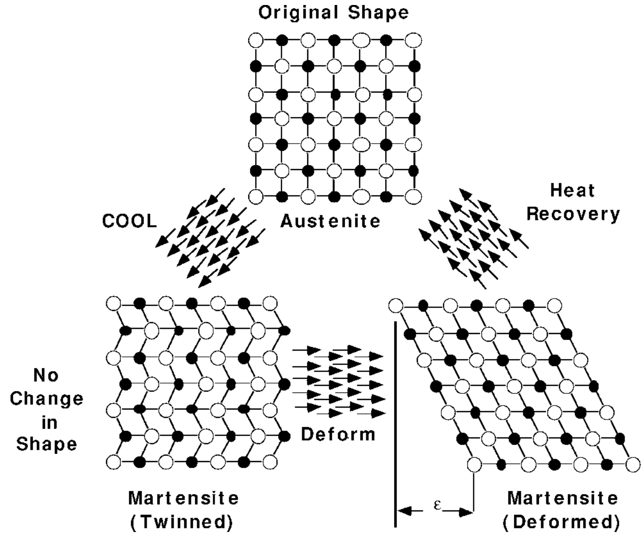

Fig. 32 Process of shape memory effect.

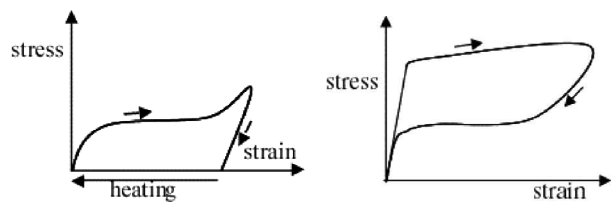

a) Shape memory effect **b) Pseudoelasticity effect**

Fig. 33 Stress-strain behavior of SMA.

yield stress, it will again result in a plastic strain (two-way motion actuator).

The thermomechanical behavior of SMA material depends on temperature, stress, and history of the material. In the heating cycle for temperatures below A_s (austenite start temperature), the material is in the 100% martensite phase, whereas for temperatures above A_f (austenite finish temperature), the material is in the 100% austenite phase. Higher stress increases A_s because more energy is needed to move the lattice structure under imposed stress. In the cooling cycle for temperatures above M_s (martensite start temperature), the material is in 100% austenite phase, whereas for temperature below M_f (martensite finish temperature), the material is in 100% martensite phase. Under an imposed stress the material will start to transition to martensite phase at a higher temperature. Hysteresis can be viewed as the friction associated with the movement of twin boundaries. At any other temperature between A_f and M_f, the material can be partly in the martensite phase and partly in the austenite phase. At temperature below A_s application of stress causes a transformation from "twinned" martensite to the stress-preferred or "detwinned" martensite, resulting in a large strain at a nearly constant stress. On the removal of stress, a significant amount of strain stays, which can be completely recovered by heating the material above A_f. This is called the shape memory effect (SME) (Fig. 33a). The ability of the shape memory alloys to recover large strains comes from the reversible phase transformation characteristics.

At a temperature above A_f, the application of stress causes a transformation from austenite to the stress-preferred martensite state. On the removal of stress, the strain is completely recovered and is called pseudoelasticity (Fig. 33b).

The state of the material is characterized by the volume fraction of the martensite phase ξ. Figure 34 schematically illustrates the change in martensite volume fraction with temperature. For a mixed state the value of ξ varies between 0 and 1.

A. Constitutive Models

Many constitutive models have been developed to describe the thermomechanical behavior of SMA materials. Some models are based primarily on thermomechanics, and others are based on a combination of thermomechanics and SMA phenomenology

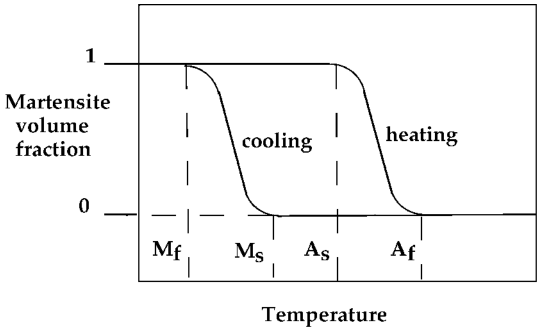

Fig. 34 Schematic of phase transformation.

and/or statistical mechanics. Most of these constitutive models are phenomenological-based macroscale models that are developed for quasi-static loading only. One of the most popular one-dimensional models is Tanaka's model[138] and is based on thermomechanics. In this model the second law of thermodynamics is written in terms of the Helmholtz free energy, followed by derivation of the rate form. It is assumed that the uniaxial strain, temperature, and martensite volume fraction ξ are the only state variables. An exponential expression of ξ is developed in terms of stress and temperature. Liang and Rogers[139] presented a model, which is based on the rate form of the constitutive equation developed by Tanaka. In their model, a cosine representation was used to describe the martensite volume fraction. A major drawback of these two models is that they only describe the stress-induced martensite transformation and do not consider strain-induced martensite transformation (shape memory effect). Hence, they cannot be applied to model the detwinning of martensite that is responsible for the SME at low temperatures. To overcome this deficiency, Brinson[140] developed a constitutive model that separates out the martensite volume fraction into two parts: stress-induced martensite and temperature-induced martensite. The first part describes the amount of detwinned or stress-preferred variant of martensite present, and the second part describes the fraction of martensite caused by the reversible phase transformation from austenite phase.

To cover both the shape memory and pseudoelasticity effects, the coefficients of the constitution equation are assumed to be non-constants. Another constitutive model is the thermodynamic model by Boyd and Lagoudas,[141,142] which is based on free energy and dissipation potential. This model is derived from the Gibbs free energy instead of the Helmholtz free energy used in Tanaka's model. This model can cover three-dimensional states and nonproportional loading. Another model that uses a thermodynamic formulation is by Ivshin and Pence.[143] There are other models that are not based on these two approaches. For example, Graesser and Cozzarelli[144] developed a three-dimensional model based on evolutionary plasticity. Sun and Hwang[145] derived a micromechanical model taking into account thermodynamics, microstructure, and micromechanics and covering both SME and pseudoelasticity. Matsuzaki et al.[146] developed a general one-dimensional thermomechanical model taking into account effects of energy dissipation, latent heat, and heat transfer during phase transformation. They introduced a general form of phase interaction energy function that was determined form quasisteady experimental stress-strain data. The model showed good agreement with test data at different strain rates. Barrett[147] developed a one-dimensional constitutive model for SMA that includes phase change hardening, hysteresis with partial transformation, and tension-compression transformations. The model however differentiates between stress-induced and temperature-induced martensite volume fractions.

The first four models are described in more detail. Tanaka[138] assumed that strain ϵ, temperature T, and martensite volume fraction ξ, are the state variables to describe one-dimensional behavior of the shape memory alloys (such as SMA wires). The constitutive equation is as follows:

$$(\sigma - \sigma_0) = E(\xi)(\varepsilon - \varepsilon_0) + \Theta(T - T_0) + \Omega(\xi)(\xi - \xi_0)$$

where subscript 0 represents the initial condition of SMA. This equation shows that the stress consists of three parts: the mechanical stress, the thermoelastic stress, and the stress caused by phase transformation. Note that the Young's modulus E and the phase transformation coefficient Ω are functions of the martensite volume fraction. These are normally expressed as

$$E(\xi) = E_A + \xi(E_M - E_A), \qquad \Omega(\xi) = -\varepsilon_L E(\xi)$$

where ε_L is the maximum recoverable strain. The E_A and E_M respectively represent Young's modulus at austenite and martensite states. Tanaka developed an evolutionary equation for the martensite volume fraction. The evolutionary equation determined from dissipation potential was resolved to have the following form:

$$\xi = \Xi(\sigma, T)$$

This equation implies that the martensite volume fraction ξ is a function of stress and temperature. Tanaka models ξ as an exponential function. During the $M \leftarrow A$ transformation, the martensite volume fraction is

$$\xi = 1 - \exp\{a_M(M_s - T) + b_M\sigma\}$$

and during the $M \rightarrow A$ transformation it is defined as

$$\xi = \exp[a_A(A_s - T) + b_A\sigma]$$

where the material constants are defined as

$$a_A = \frac{\ln(0.01)}{(A_s - A_f)}, \qquad b_A = \frac{a_A}{C_A}$$

$$a_M = \frac{\ln(0.01)}{(M_s - M_f)}, \qquad b_M = \frac{a_M}{C_M}$$

The coefficients used in the preceding constitutive relations, E, Θ, and Ω, and the parameters M_s, M_f, A_s, A_f, C_A, and C_M are determined normally through testing of the SMA wires (Table 6). Note that the transformation temperatures M_s, M_f, A_s, and A_f are determined in a stress-free condition. The stress influence coefficients C_A and C_M are the slope of the critical stress-temperature plots for the austenite and martensite transformation boundaries, respectively.

Liang and Rogers[139] utilized the same constitutive relation but developed a new form of the evolutionary equation for the martensite volume fraction. The difference between the two models arises in the modeling of the martensite volume fraction. In this model ξ is modeled as a cosine function. Both models however lack proper representation of shape memory effect (detwinning at room temperature). Both models describe transformation from martensite to austenite and vice versa. They are, however, valid only for fully detwinned martensite state.

Unlike the preceding two models, Brinson's model[140] represents the transformation from the detwinned martensite to the stress-preferred variant, which leads to a description of shape memory effect below A_s. This model uses a similar representation for constitutive equation with some modifications. The modified relation is as follows:

$$\sigma - \sigma_0 = E(\xi)\varepsilon - E(\xi_0)\varepsilon_0 + \Omega(\xi)\xi_s - \Omega(\xi_0)\xi_{s0} + \Theta(T - T_0)$$

In this model the martensite volume fraction is divided into two parts:

$$\xi = \xi_S + \xi_T$$

where ξ_S is the portion of the detwinned (or stress preferred) martensite present at low temperature and ξ_T is the portion of twinned (or

Table 6 Thermomechanical properties of SMA wires tested (Dynalloy 15 mil NiTi binary alloy)[158]

Coefficient/ property	Unit	Value	Coefficient/ property	Unit	Value
σ_{cr}^s	Pa	1.38e+6	A_s	°C	52
σ_{cr}^f	Pa	1.72e+6	A_f	°C	65
C_A	Pa/°C	8e+6	$M_{s(\mathrm{Tanaka})}$	°C	43.5
C_M	Pa/°C	12e+6	$M_{f(\mathrm{Tanaka})}$	°C	40.7
E_A	Pa	45e+9	$M_{s(\mathrm{Brinson})}$	°C	55
E_M	Pa	20.3e+9	$M_{f(\mathrm{Brinson})}$	°C	42

randomly oriented) martensite that comes from reversible thermal phase transformation from austenite. Also, a modified cosine representation for the martensite volume fraction is used.

The fourth model by Boyd and Logoudas[141,142] is a more general three-dimensional model. In this model the total specific Gibbs free energy is determined by summing the free energy of each phase of shape memory materials plus the free energy of mixing. A constitutive relation satisfying the second law of thermodynamics is developed. The total strain consists of two parts: the mechanical strain ε_{ij} and the transformation strain $\varepsilon_{ij}^{\mathrm{tr}}$, which is a function of the martensite volume fraction:

$$\sigma_{ij} = C_{ijkl}\left[\varepsilon_{kl} - \varepsilon_{kl}^{\mathrm{tr}} - \alpha_{kl}(T - T_0)\right]$$

An evolutionary equation for the martensite volume fraction is derived from the dissipation potential:

$$\sigma_{ij}^{\mathrm{eff}} + d^1 T - \rho b_1 \xi = Y^{**} + d_{ijkl}^3 \sigma_{ij}\sigma_{kl} + d_{ij}^4 \sigma_{ij}\Delta T$$

where Y^{**} is the threshold stress value, $d^1 T$ is related to the entropy reference state, d_{ijkl}^3 and d_{ij}^4 are parameters that are related to changing elastic moduli, ρ is the mass density, b_1 is a material constant, and ΔT is the temperature difference. Brinson and Huang[148] showed that this model reduced to one-dimensional format becomes identical to Tanaka's model. There is, however, one exception, that unlike Tanaka's model this model is applicable to represent the martensite transformation from twinned to detwinned state at a low temperature.

Another model developed by Ivshin and Pence[143] was derived from a thermodynamic consideration of the kinetic relations for the hysteresis of the phase fraction. Instead of using the martensite volume fraction ξ as the primary variable, they used the austenite volume fraction α

$$\alpha = 1 - \xi$$

Total strain is

$$\varepsilon = (1 - \alpha)\varepsilon_m + \alpha\varepsilon_a$$

where ε_m and ε_a are strains in martensite and austenite regions.

Since the formulation of the original Tanaka model,[138] it has been updated to cover the influence of the SME.[149–154] The primary update of the model has been carried out through the introduction of new effect called the rhombohedral-phase transformation (RPT). The RPT is a thermally reversible transformation that takes place at low strains and low temperatures, much like martensite detwinning. At low temperatures (below A_s) RPT takes place followed by regular martensite transformation. In repeated stress-strain cycling at room temperature (strain > 1%), the RPT is noticeable only in the first cycle and disappears thereafter. This is attributed to two-way shape memory effect observed through heating and cooling of the specimen. At high temperatures (between A_s and A_f) the RPT is noticeable in the form of small nonlinearity of the linear region of the pseudoelastic curve. The RPT or R-phase effect is represented by a volume fraction coefficient η. Assuming the first cycle under zero stress/strain condition ($\eta = 0$, $\xi = 0$), an application of strain below 1% results in R-phase transformation ($\eta = 1$, $\xi = 0$). On heat activation we recover R-phase. In all other cases we do not recover R-phase. Using this concept, the authors were able to correlate predictions with test data especially at low temperatures. Naito et al.[154] and Sittner et al.[153] represented the RPT and martensite transformation in a unified way using energy function, with appropriate "switching functions" to handle different transformations.

Using the constitutive models in conjunction with the models for the martensite volume fraction develops stress-strain curves. Because ξ is a function of stress in all models, an iterative method such as the Newton–Raphson method is used to solve for the stress.

B. Critical Transformation Regions

For constitutive models the required constants are obtained from the critical stress-temperature diagram. Figure 35 is a plot that delineates the regions of transformation. The regions marked with arrows are those in which the material exists in pure form. All other regions could have a mixture of phases, and the exact content of

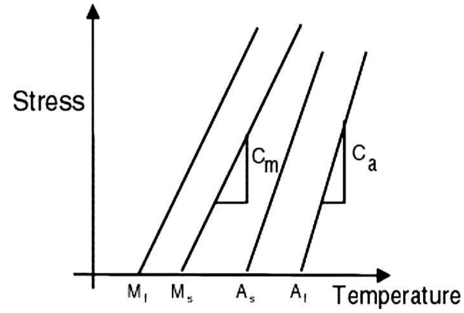

a) Original Tanaka model

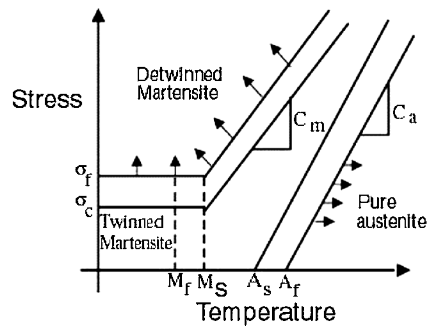

b) Brinson model

Fig. 35 Critical stress-temperature profiles in constitutive models.

the mixture depends on the thermomechanical history of the material. There are, however, differences in the definition of the material constants in different models. Both the Tanaka model and Liang and Rogers model assume a straight-line stress-temperature relationship, and M_s and M_f correspond to zero stress condition. The stress-temperature relationship is somewhat different for Brinson's model; the critical stresses divide the transformation regions. The M_s and M_f are defined as the temperature above which the application of stress does not cause a pure transformation from twinned to detwinned martensite.

Because of these differences, the interpretation of the transformation temperatures in the two types of models differs from each other. In Brinson's model the parameters M_s and M_f are defined as the temperature above which the martensite transformation stresses are a linear function of temperature, as shown in the Fig. 35b. In the Tanaka and Liang and Rogers models, however, these parameters are defined at zero stress and are the temperatures for martensite start and finish obtained by cooling from austenite without the application of stress (Fig. 35a). Therefore, when calculating these constants from the experimental critical points, the numerical values used for Tanaka and Liang and Rogers model for M_s and M_f are obtained from extrapolating the martensite start and finish lines to zero stress, whereas those used by Brinson model are obtained at the critical stresses σ_{cr}^s and σ_{cr}^f. These different values for the models must be used in order to obtain a fair comparison between these models and to match them to experimental observations.

Prahlad and Chopra[155] presented critical stress-temperature data from different tests on the same curve and demonstrated the linear variation of the critical stresses with temperature that is assumed in all of the models (Fig. 36). Data corresponded to three different tests that, respectively, used heat flow measurements with differential scanning calorimeter (DSC), constant temperature, and constant strain (constrained recovery) conditions. All of these tests were carried out at a very low heat rate and as such represented quasistatic conditions. Tests at constant strain and constant temperature were carried out using MTS 810 tensile test machine with a controllable thermal chamber (environment heating). Two separate thermocouples were used to monitor temperature, one in the thermal chamber and another K-type thermocouple directly mounted on the wire. The recovery stress data points lie in the transformation region between the austenite start and finish states for heating phase and martensite start and finish states for cooling phase. Thus the two straight lines represent martensite start and help determining M_s and A_s. The

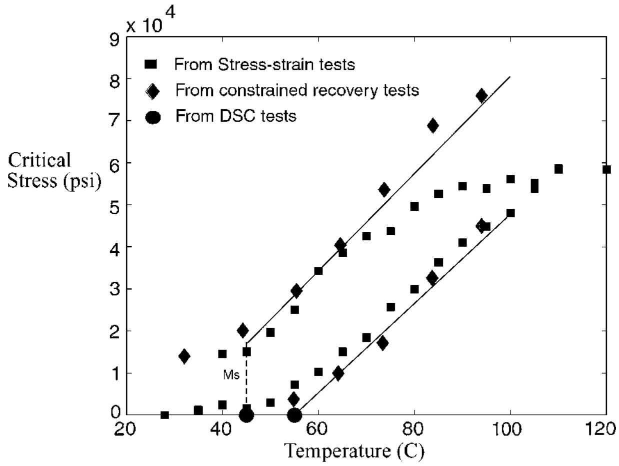

a) Environmental heating

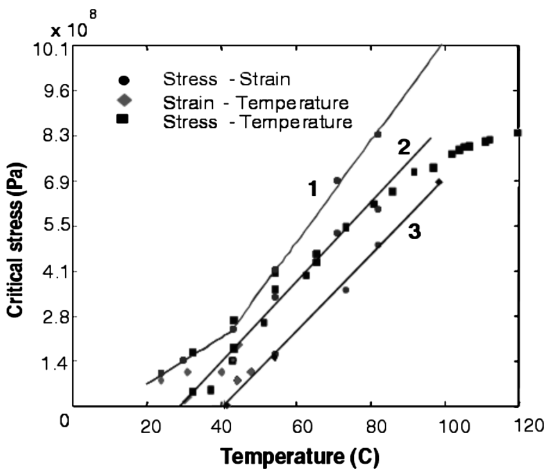

b) Resistive heating

Fig. 36 Experimental critical stress-temperature plot.[155]

martensite finish and austenite finish follow nearly the same slopes and help determine M_f and A_f. The critical stress σ_{cr}^s is the stress at which the transformation from twinned to detwinned martensite starts, and the critical stress σ_{cr}^f represents the stress where this transformation is nearly complete. These critical stresses are determined for a temperature below M_s. As shown in Fig. 35b, the region above σ_{cr}^f line represents pure detwinned martensite state, and the region below σ_{cr}^s line is a twinned state. The interpretation of M_s and M_f can be different by two approaches. Strain at which detwinning gets completed is referred to as ε_l. The parameters C_A and C_M are the slopes of these two curves. It is assumed that below M_s the critical stresses σ_{cr}^s and σ_{cr}^f associated with the detwinning are independent of temperature (a small anomaly from test data). The critical stress-temperature data obtained at low stresses and temperatures were found to be more sensitive to test conditions and in fact were more difficult to obtain. To determine the transformation temperatures (M_s, M_f, A_s, and A_f) of the SMA wire under no stress condition, Perkin–Elmer DSC is normally used. This instrument uses the change in heat capacity of the material to determine the start and finish transformation temperatures. When the material undergoes phase transformation, it absorbs (or emits) large amount of heat with a relatively small change of temperature, and the DSC captures such a change. Two different temperature control methods are used; the first involves the use of a thermal chamber (environmental heating), and the second involves internal heating (resistive heating). Even though similar trends are observed with both methods of heating, transformation stresses differ as a result of small variations in temperature. For example, the transformation from martensite to austenite state takes place at lower temperatures in the case of resistive heating.

To stabilize the SMA for a repeatable behavior, it becomes necessary to "cycle" the material mechanically. One approach is to stretch the wire (to, say, 4% strain with a strain rate of 0.0005/s) at a constant temperature (well above A_f) and then release to zero stress condition. After 20–30 cycles the pseudoelastic behavior of the wire gets stabilized.[156] In the second approach the SMA wire is mechanically strained at room temperature (in martensite phase) followed by a thermal cycle under no stress condition by heating the wire above A_f and then cooling down below M_f. Again, it requires about 20–30 cycles to stabilize the material.[156,157] Both methods are equally effective to stabilize the material, except the first method is simple because it does not require thermal cycling.

C. Comparison of Stress-Strain Results

The stress-strain plots at constant temperature show shape memory effect at low temperatures and pseudoelasticity at high temperatures (Fig. 37). At low temperature (say 35°C, below A_s) the material is in martensite state. Once critical stress σ_{cr}^s is reached, the transformation to stress-preferred variant starts. The Tanaka model and the Liang and Rogers model are not valid for temperatures below A_s, whereas the Brinson model is applicable. The points 1 represent the start of transformation to detwinned martensite and points 2 represent the start of transformation to austenite phase and points 3 show the finish of transformation to austenite phase. Figure 38 shows a good comparison of the Brinson model with test data. At high temperature (say 85°C, above A_f) the material is fully austenitic to start with and gets transformed to the stress-preferred martensite variant at critical stress. This transformation gets reversed on unloading, causing a complete pseudoelastic recovery. For temperatures above A_s, all three models are applicable. Because both the Brinson and the Liang and Rogers models use a cosine formulation to describe the martensitic volume fraction, they yield nearly identical predictions

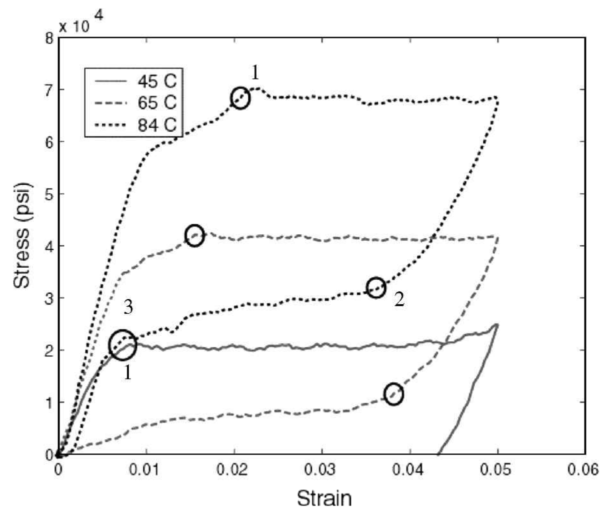

Fig. 37 Stress-strain plots.[158]

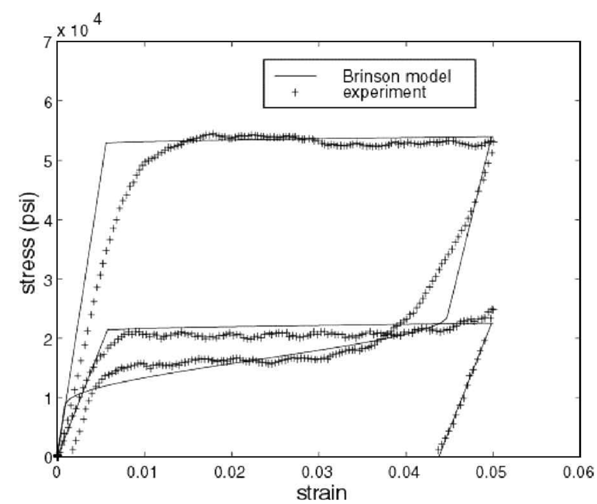

Fig. 38 Comparison of models with test data.[158]

in this regime. It is clear that as long as coefficients of models are identified properly from test data all constitutive models can predict stress-strain behavior satisfactorily at high temperatures (above A_s).[158] Note that the Tanaka model uses exponential representation for martensite volume fraction, which can lead to numerical convergence problem during the iterative solution process.

D. Resistive Heating vs Internal Heating

During the phase transformation of SMA, there is a large variation of internal resistance of material.[159] As a result of this, it is quite difficult to hold constant temperature with resistive heating especially during phase transformations. It is however possible to achieve a temperature control of the order of 2–3°C by very slow heat activation of wire. Figure 36a shows the critical stress-temperature plot from experimental data points obtained using environmental heating. Figure 36b shows the corresponding critical stress plot for resistive heating. By comparing the two, it appears that the entire plot appears shifted towards lower temperatures in case of resistive heating. However, the slopes of critical stresses seem to remain unchanged. In a polycrystal structure involving different phases, the resistance level can be quite different in each phase. Passing the current through the wire can result in a differential heating of material (surface temperature different from internal temperature). As a result, it might not be prudent to mix two sets of data. It might be important to use different values of M_s and M_f for modeling two cases of heat activation.

E. Constrained Recovery Behavior

Large recovery stresses are developed when the SMA wire is constrained during the heating process. Figure 39a shows the complete constrained stresses developed at different temperatures for different prestrains. The final constrained stress is independent of prestrain as long as it is above a threshold value of 2%. Below about 2% prestrain, the stress path followed, and the final stresses are dependent on prestrain. Most of the models satisfactorily predict the constrained recovery stress, as long as the values are low (less than plastic yield stress). Lower prestrains offer the advantage of less permanent plastic deformation and fatigue with repeated cycles.[159,160] Figure 39b shows the stress history of SMA wire in repetitive cycles. After three cycles the material is stabilized, and the following cycle repeats the results of previous cycle. This clearly shows that the SMAs can be used as active force generators under repetitive loading.

F. Nonquasistatic Loading

If the material is strained at a faster rate, the material does not have time to relax and as a result attains a higher stress value. The rise in stresses might be a result of local temperature changes that occur immediately if the wire undergoes nonquasistatic loading. After a high strain rate, if the material is relaxed it returns to its quasistatic stress value. (Local temperatures might settle down to equilibrium values.) This is called stress relaxation phenomenon.[159–162] Shaw[163] pointed out that some of the self-heating effect arises from the origination of local nucleation sites with temperature differences along the wire. It has been shown that the transformation stresses increase significantly as a function of strain rates (Fig. 40). If the loading is noncontinuous, the SMA appears to fall back into its thermodynamic equilibrium state (stress relaxation). This phenomenon also manifests itself as a dependence of the material behavior on the loading pattern (Fig. 41). For dynamic loading it is necessary to develop

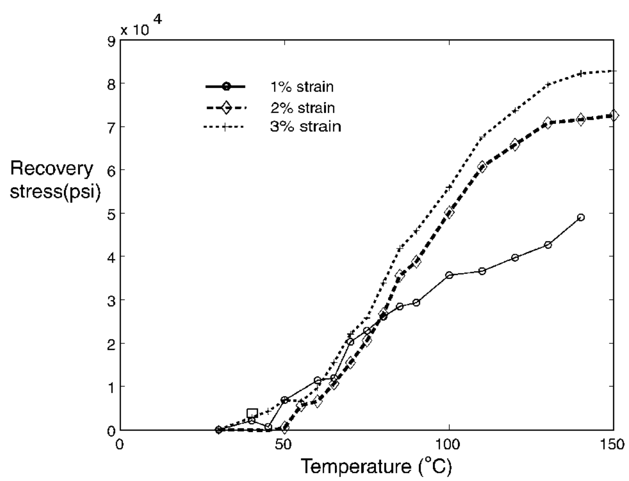

a)

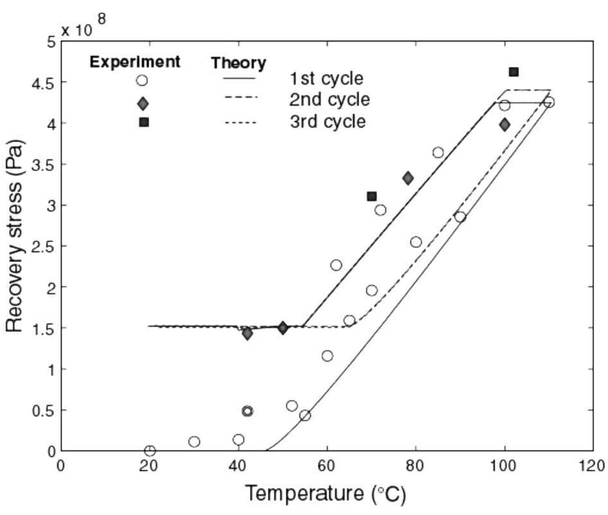

b)

Fig. 39 Restrained recovery behavior with prestrain.[155]

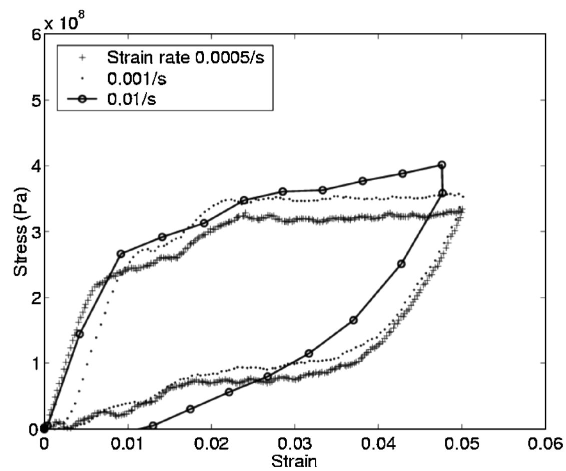

Fig. 40 Effect of loading rates on stress-strain loading pattern on stress-strain behavior.[155]

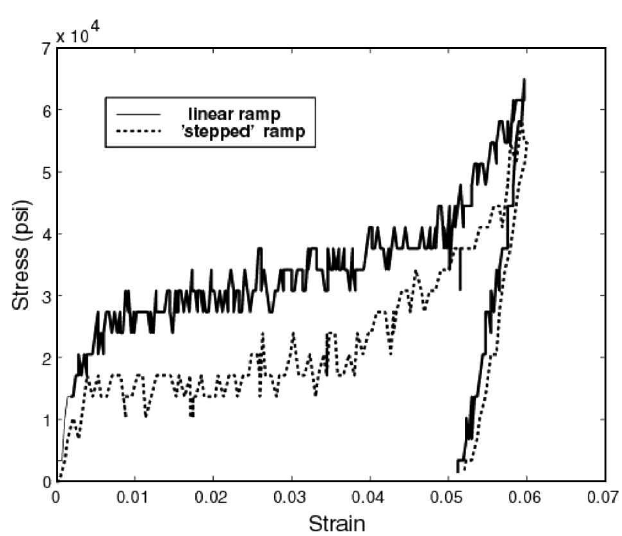

Fig. 41 Effect of loading pattern on stress-strain behavior.[155]

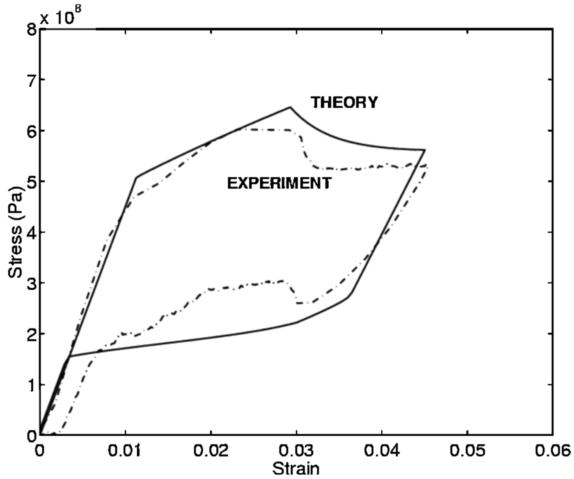

Stress profiles

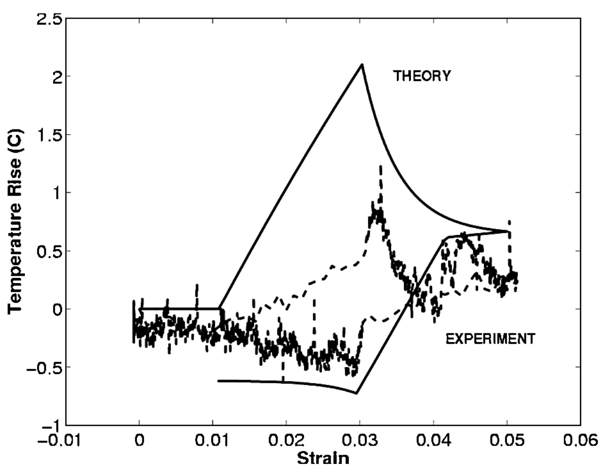

Temperature profiles

Fig. 42 Comparison of nonquasisteady model prediction with experimental data; strain stepped from 0.01/s to 0.0005/s at 3% strain.[162]

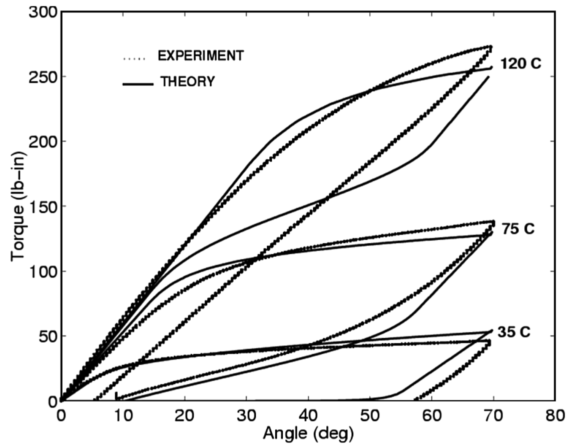

a) Constant temperature predictions

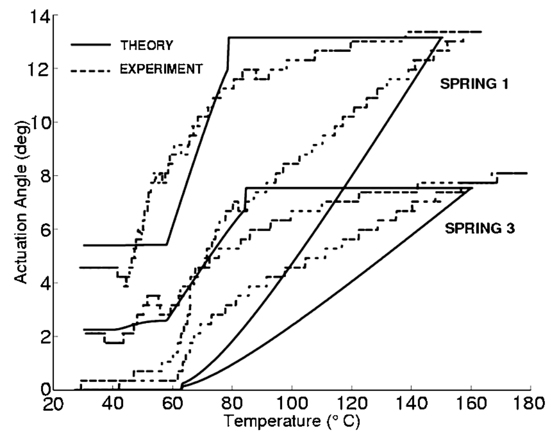

b) Actuation against torsional springs

Fig. 43 Comparison of torsional model prediction with experimental data.[162]

suitable constitutive models. Lexcellent and Rejzner[164] determined the change in temperature caused by strain rate through the integration of heat equation. Predicted results agreed satisfactorily with test data. Prahlad and Chopra[162] used the rate form of the Brinson equation coupled with an energy equilibrium analysis to obtain simultaneously both temperature and stress as a function of strain for a given strain rate. The predictions showed good qualitative agreement for both stress and temperature evolution under loading involving an instantaneous change in the strain rate during the loading cycle (Fig. 42). However, more careful temperature measurements are required to validate the model quantitatively. Potapov and Silva[165] developed a simple time response model of Ni-Ti alloys, which takes into account latent heat and thermal hysteresis of transformation under conditions of free and forced air convection. The actuation frequency of shape memory actuators was seen to be controlled primarily by the cooling time while increasing the input power can reduce the heating time. The calculated time response showed good agreement with test data.

G. Torsional Characteristics of SMA Rods and Tubes

In addition to the use of SMA wires under uniaxial loading as actuation elements, SMA rods and tubes have also been used for twist actuation. The principle of operation is the same as in the case of SMA wires—the rod (or tube) is first pretwisted and then tends to recover its original, untwisted state when heat activated. One of the first torsional models was proposed by Davidson et al.[166] for the torsional actuation of SMA rods uses the Liang and Rogers constitutive model in conjunction with standard relationships for pure shear deformations. The model parameters were obtained by curve fitting the parameters required for Liang and Rogers model to the torsional experimental data. Keefe and Carman[167] proposed an exponential model for the relationship between shear stresses and strains in the SMA alloy. However, this relies more on fitting the model parameters to torsional data over a prescribed range of thermomechanical data and does not include the modeling of the SMA phenomenology over the entire thermomechanical range. Prahlad and Chopra[168] proposed a torsional model based on the Brinson model for the SMA constitutive behavior. The model parameters were obtained in extensional testing and then applied to the torsional case. Good overall agreement was obtained both in the constant temperature (Fig. 43a) case and while actuating a torsional spring (Fig. 43b). In contrast to these models that model only shear deformations of the SMA, there are several models that are fully three-dimensional and therefore theoretically capable of handling loading in any arbitrary direction (including combined tension-torsion loading). An example of these models is the Boyd and Lagoudas[141,142] model. However, the identification of model parameters and implementation for these models are complex.

H. Damping Characteristics

Above a critical temperature, the shape memory alloys exhibit pseudoelastic stress-strain hysteresis over a large range of strain (6–8%). Cyclic variation in stress and strain can result in a large dissipation of strain energy that translates into damping augmentation.[169] Wolons et al.[170] carried out experimental investigation to determine damping characteristics of NiTi alloy wires under uniaxial loading and systematically examined the effects of cycling, frequency of oscillation, strain amplitude, temperature, and static-strain offset on damping. It was shown that the shape of the hysteresis loop changes significantly with frequency; the energy dissipation decreases with frequency and reaches a saturation value at about 10 Hz. Also, the energy dissipation decreases with higher temperature (say, above 90°F) and increases with lower static strain offset.[171] Also, Lammering and Schmidt[172] examined damping capacity of NiTi in the pseudoelastic range and showed that the area of hysteresis loop decreases with increasing strain rate. Ju and Shimamoto[173] developed composite beam with embedded SMA fibers to augment its damping. Damping was shown to be a function of both temperature and current.

I. Composite Beams with Embedded SMA Wires

SMA wires were used to alter the natural frequencies of composite beams. Rogers and Barker[174] showed an increase in the natural frequencies of a composite beam because of the activation of SMA wires embedded directly in the structure. In this experimental study, the beam and SMA wires were independently clamped. When the SMA wires were heated, the beam was subjected to an axial force caused by the shape memory effect. They demonstrated a 200% increase in the natural frequency of graphite-epoxy beams by using a 15% volume fraction of SMA wires. Correlation of experimental results with predictions was not carried out. Baz et al.[175] conducted a study on the active vibration control of flexible beams. Experiments were conducted on flexible beams with SMA wires mechanically constrained on the exterior of the structure. The recovery force caused by mechanically constrained, prestrained SMA wires at higher temperatures was used to demonstrate active vibration control of flexible beams. In such an application, external access to the substructure becomes essential in order to clamp SMA wires to an independent support. For many aerospace structures like rotor blades or airplane wings, it might not be possible to follow this scheme. In another study Baz et al.[176] inserted SMA wires into flexible beams with sleeves to control their buckling and vibration behavior. They used a finite element method to correlate with their experimental results. Overall, predictions correlated satisfactorily with test data. They showed that the buckling load of a flexible fiberglass composite beam could be increased three times when compared to the buckling load of an uncontrolled beam.

Using a single surface-attached SMA wire, an active control of beam deflection with temperature activation was investigated by Brinson et al.[177] Also, predictions were successfully compared with test data. The potential of shape control with SMA wires was pointed out. Lagoudas et al.[178] used a layer-wise shear deformation theory to show the shape control of plate structures with embedded SMA strips using thermal activation. Turner[179] developed a finite element formulation for predicting the thermomechanical response of SMA hybrid composite structures with constrained or free boundary conditions. The model captures the material nonlinearity with temperature for composites with embedded SMA actuators.

Building composite structures with embedded SMA wires is a challenging task. First, the surface of wires needs to be treated to achieve a good bond condition. Second, the loss of prestrain during the curing process needs to be prevented. There are three possible approaches to overcome this problem. One approach is to use special reinforced composite plies (Hercules) that cure at room temperature. The second approach is to clamp each one of the SMA wires separately during the formal curing process in an autoclave. The third approach is to use fused silica tubes filled with "dummy" steel wires during curing process. Once the curing process is complete, the steel wires are replaced with prestrained SMA wires. To ensure a good bond between the silica tubes and the graphite-epoxy material, a film adhesive is used. Figure 44 shows a fabricated composite beam with three SMA wires in sleeves.

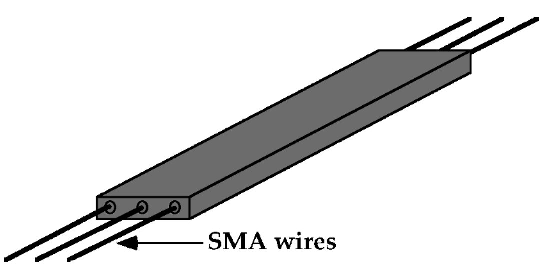

Fig. 44 Graphite-epoxy beam with SMA wires.

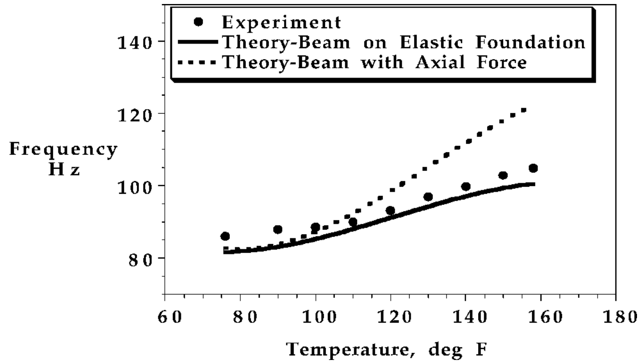

Fig. 45 Fundamental frequency of clamped-clamped graphite-epoxy beam activated by one 20-mil-diam SMA wire. Beam dimensions: length = 18 in. (45.72 cm), width = 0.25 in. (6.35 mm), thickness = 0.068 in. (0.173 mm).[180]

Epps and Chandra[180] tested graphite-epoxy solid beams with sleeve-inserted SMA wires for their bending frequencies under clamped boundary conditions. The natural frequencies of this composite beam depend not only on the beam properties but also on SMA characteristics. An important SMA-related characteristic is the recovery force in wires, which in turn depends on prestrain, mechanical properties of SMA and temperature. Figure 45 shows the first bending frequency of a graphite-epoxy composite beam activated by one 20-mil-diam SMA wire. It shows a 22% increase in the first bending frequency with an SMA volume fraction of 2%. For analysis, the SMA wires were treated as an elastic foundation for the composite beam, and the stiffness of foundation depended on the constraint recovery force. Good correlation between theory and experiment was achieved.

Furuya[181] discussed design and material evaluation for the development of shape memory composites. Two types of concepts were proposed: TiNi fiber/aluminum matrix and TiNi fibers and particles/plaster matrix. The first composite showed increase of tensile strength (yield stress) and fatigue resistance, and the second showed increase of fracture resistance and vibration damping. Birman[182] presented micromechanics analysis of composite structure with embedded SMA wires. Most analyses are in early stage of development and require systematic validations under a wide range of load conditions.

Shape memory alloys such as nitinol have large force and stroke and therefore have enormous potential for low frequency (steady) applications. The materials are highly nonlinear function of temperature, stress, and strain history, and it requires a fine tuning (say, using an adaptive feedback controller) to achieve the desired state. Also, incorporating a locking mechanism to maintain the desired state of the actuator becomes important. Most of the constitutive models are developed for quasistatic loading, and these should be expanded to cover low-frequency dynamics. There has been good success to validate constitutive models for nitinol wires (isolated) in extensional loading with test data. To cover expanding applications, the material constitutive models should be validated for other load conditions such as torsional loading. In the next phase it might be important to validate predictive models with test data for simple composite beams and plates with directly embedded SMA wires. For such structures local stress/strain distributions using either detailed finite element analysis (such as three-dimensional solid elements) or higher-order shear deformation theory might reveal the mechanism of actuation as well as help to establish the integrity of structure.

VI. Magnetostrictives and Electrostrictives

A. Magnetostrictives

Magnetostrictive materials consist of alloys of iron and rare Earth elements such as terbium and dysprosium, which undergo deformation when exposed to magnetic field. The commercial magnetostrictive material is Terfenol-D (Terbium-Ferrous-Naval Ordnance Laboratory-Dysprosium) and is normally available in the form of rods of different diameters. With no magnetic field oblong magnetic domains in the material are randomly oriented (mostly perpendicular to rod's longitudinal axis). With the application of compressive stress, most of the domains get oriented normal to rod's axis. In the presence of a magnetic field along the longitudinal axis, these domains rotate and become mostly parallel to this longitudinal axis causing an induced strain. As the intensity of the magnetic field increases, more domains rotate, and longitudinal strain increases and finally saturates (at about 0.2%) at high field levels. Because magnetostriction is a molecular action, the mechanical response is very fast (kHz). The magnetic field is produced either by a permanent magnet or by a magnetic coil surrounding the rod. Normally, a permanent magnet is used to create a steady bias field, and an ac current in the surrounding coil is used to control the time-varying magnetic field and, in turn, the nonsteady induced strain in the Terfenol-D rod. An extensional strain is induced in the direction of magnetic field. If the field is reversed, the domains reverse direction, but again induce an extensional strain. On the macroscopic level a magnetostrictive material conserves volume, and as a result the diameter shrinks as a result of Poisson's effect. For Terfenol-D, Curie temperature is above 380°C. At high operating regimes hysteresis and nonlinearities are intrinsic to magnetostrictive behavior.

James Joule discovered the magnetostrictive effect first in nickel in 1840. Later, cobalt, iron, and their alloys were shown to have significant magnetostrictive effects like nickel. The maximum strains were of the order of 50 ppm (parts per million, 0.005%). In early 1970s Arthur Clark and his research group at Naval Ordnance Lab (later known as NSWC) discovered Terfenol-D, which produced a significantly larger magnetostriction resulting in a maximum strain of the order 2000 ppm. This is almost twice the maximum strain produced by piezoceramics. The strains and forces produced by Terfenol-D are more than those generated by piezoelectric and electrostrictive materials. Magnetostrictives find applications in machine tools, servo-valves, hybrid motors, sonar and tomography, automotive brake systems, micropetitioners, and particulate-actuators and sensors. As a result of the Joule effect, an application of the magnetic field results in longitudinal extensional strain accompanied by transverse compressive strain. The reciprocal effect is called Villari effect, where an application of stress (that is, strain) results in a change in its magnetic field. The Joule effect is used in actuators, whereas the Villari effect is used in sensors. The Joule effect transfers magnetic energy to mechanical energy, whereas the Villari effect transforms mechanical energy to magnetic energy. Using a helical magnetic field around the magnetostrictive material, a twisting action is produced, which is called the Wiedemann effect. The inverse effect in which application of torque results in a change of magnetization is called the Matteusi effect. The manufacturing of Terfenol-D is carried out by melting the material and then casting and directionally solidifying to provide the crystalline microstructure needed to produce large strains. Magnetostrictive materials are available in the form of rods, thin films, and powder. Normally, to produce magnetic field a wound wire solenoid that converts electric energy to magnetic energy is used. As per Maxwell's equation, the intensity of magnetic field is proportion to the current in solenoid.

The strain increases quadratically with magnetic field intensity H (Fig. 46). There is no hysteresis because only a static condition

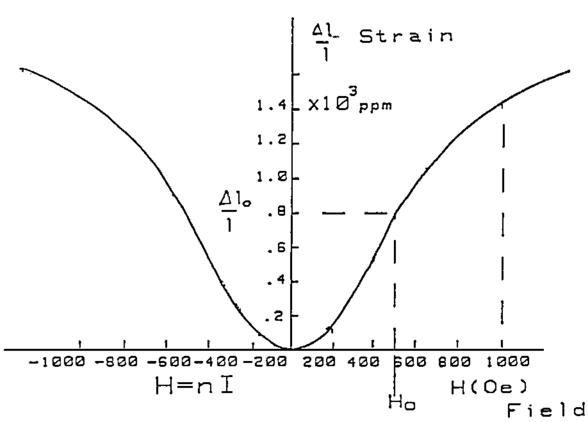

Fig. 46 Strain for a Terfenol-D rod.

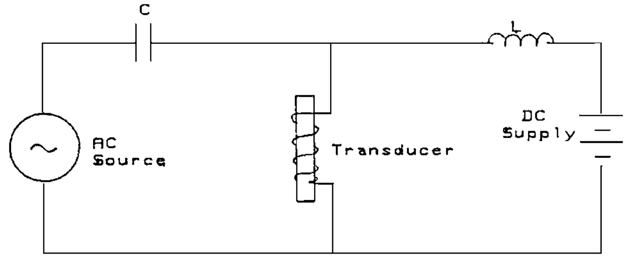

Fig. 47 dc bias circuit for magnetostrictive transducers.

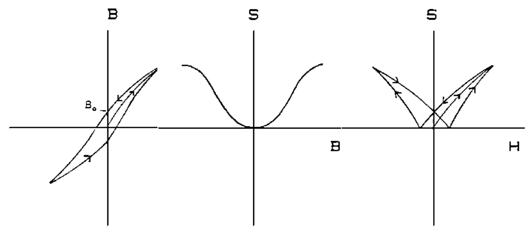

a) B-H b) S or ε-B c) S or ε-H

Fig. 48 Hysteretic behaviors for magnetostriction.

is considered:

$$\text{Magnetic intensity } H = nI \text{ (A/m or Oe)}$$

where I is the current though the surrounding coil of length L and N turns and n is the number of turns per unit length,

$$n = N/L$$

The magnetic field H can be expressed either in electromagnetic units (emu) or in MKS units. In magnetic units it is expressed as Oe (oersted), whereas in MKS units it is defined as A/m (amperes per meter):

$$1(\text{A/m}) = \frac{4\Pi}{1000}\text{ Oe } = 79.58\text{Oe}$$

The dynamic strain amplitude is limited by the maximum available strain. To create oscillating strain, a bias dc field is applied. Figure 47 shows a possible circuit to create an oscillatory strain. The capacitor C is used to block the dc supply from entering ac power source, and inductance L is selected to be large enough to prevent the ac current from entering the dc power supply. Typically, the impedance of additional inductance L is larger than that of the actuator, which in turn is larger than that of the capacitor. For dynamic condition there is hysteresis between magnetic field and strain produced. Figure 48a illustrates magnetic flux density B (internal) vs magnetic field intensity H (external), and there is hysteresis. Figure 48b shows strain ε vs internal flux density B, and there is no hysteresis. Figure 48c is obtained combining these two graphs, and a butterfly curve is obtained between strain and magnetic intensity H. For ETREMA Terfenol-D, this hysteresis effect is small and is often ignored for large strains. Similar to electrostrictives, Terfenol-D has a very low hysteresis.

Magnetostrictives are capable of providing both actuation and sensing capabilities. This reciprocal magnetomechanical transduction is often referred to as bidirectional energy exchange between the magnetic and elastic regimes.

Constitutive relations are as follows.

Strain:

$$\varepsilon = S^H\sigma + dH$$

Flux:

$$B = d\sigma + \mu^\sigma H$$

where d is the magnetostrictive constant (magneto-mechanical cross-coupling coefficient) that corresponds to the slope of linear part of $\varepsilon - H$ curve and μ^σ is the free permeability (at constant stress) that corresponds to the slope of the $B - H$ curve in the first quadrant. S^H is the compliance of the rod at nominal operating field (bias field). The first equation shows that the strain of a magnetostrictive element is function of mechanical stress and applied magnetic field. The second equation shows that the magnetic induction B varies with stress and applied field. This model appears a generalization of two phenomenological relations: linear Hook's law ($\varepsilon = S\sigma$) and magnetic constitutive law ($B = \mu H$). Thus the total strain consists of two parts: mechanical strain and magnetostrictive strain. In a similar way, the magnetic induction consists of two parts: constant-stress magnetic component and magnetoelastic interaction component. The magnetic and structural regimes are coupled through magnetization as a result of both externally applied magnetic field and stress-induced field. This linear model provides adequate characterization of magnetostrictive material at the low operating regime. Note that at high operating regimes hysteresis and nonlinearities become important.

For an unloaded rod, strain and flux are as follows.

Strain:

$$\varepsilon = dH$$

Flux:

$$B = \mu^T H$$

For longitudinal induced strain

$$d_{33} = \left(\frac{\mathrm{d}\varepsilon_{33}}{\mathrm{d}H_3}\right)_\sigma = \left(\frac{\mathrm{d}B_3}{\mathrm{d}\sigma_3}\right)_H, \qquad S_{33} = \left(\frac{\mathrm{d}\varepsilon_3}{\mathrm{d}\sigma_3}\right)_H = \frac{1}{Y_3^H}$$

$$\mu_{33}^\sigma = \left(\frac{\mathrm{d}B_3}{\mathrm{d}H_3}\right)_\sigma$$

The elastic modulus Y_3^H and magnetomechanical coefficients d_{33} vary from material to material and often with operating conditions.

For ETREMA Terfenol-D rods

$$\mu_{33}^\sigma = 9.2 \text{ (emu)}$$

$$= 11.56 \times 10^{-6} \text{(MKS units)}$$

$$d_{33} = 1.6 \times 10^{-6} \text{ Oe}^{-6}$$

$$= 20 \times 10^{-9} \text{ m/A}$$

The nominal open circuit Young's modulus is

$$Y_3^H = 2.65 \times 10^{10} \text{ N/m}^2$$

$$S_{33}^H = 1\big/Y_3^H = 0.377 \times 10^{-10} \text{ m}^2\text{/N}$$

The properties of a magnetostrictive element depend on level of stress, magnetization, and temperature distribution. Butler[183] and Butler et al.[184] provided a comprehensive introduction to the magnetostrictive materials and especially to the ETREMA's Terfenol-D. Engdahl and Svensson[185] presented a simple, uncoupled finite difference analysis to predict steady response of magnetostrictive rod as a result of applied sinusoidal magnetic field using linear material characteristics. Kvarnsjo and Engdahl[186] developed a two-dimensional finite difference transient analysis caused by magnetic field using nonlinear material characteristics. The finite difference methods are less versatile to deal with structures constituting dissimilar materials such as the case with smart structures. Claeyssen et al.[187] developed a three-dimensional, coupled, linear finite element analysis to establish the effective dynamic coupling constants of a magnetostrictive actuator. They used an empirical representation of material characteristics. Carman and Mitrovic[188] formulated a coupled one-dimensional nonlinear finite element analysis incorporating a phenomenological constitutive model for magnetostrictive actuator. The model showed good agreement with test data at high preloads. However this model is unable to represent saturation effects. Following the work of Hom and Shanker,[189] Duenas et al.[190] developed a more comprehensive constitutive model of magnetostrictive material that includes magnetization saturation and thermal effects. Dapino et al.[191] developed a coupled nonlinear and hysteretic magnetomechanical model for magnetostrictives. The magnetostrictive effect is modeled by taking into account the Jiles–Atherton model of ferromagnetic hysteresis in combination with quartic magnetostriction law. This model provides a representation of the bidirectional coupling between the magnetic and elastic states. The model appears to represent accurately the magnetic hysteresis in the material. Anjanappa and Bi[192] and Anjanappa and Wu[193] presented a simple one-dimensional model to simulate the quasistatic response of a magnetostrictive miniactuator (they developed) as a result of the applied magnetic field. Also, Wu and Anjanappa[194] and Krishnamurthy et al.[195] developed a simple rule-of-mixture model to calculate the response of magnetostrictive particulate composite. Flatau et al.[196] discussed magnetostrictive particle composites in terms of underlying physical processes that occur during fabrication, material characterization, design considerations, and structural health sensing.

Kannan[197] provided a continuum level quasistatic, three-dimensional finite element analysis using nonlinear behavior of bulk magnetostrictive materials and particulate magnetostrictive composites. Two alternate possibilities for a nonlinear incremental constitutive model are explored: characterization in terms of magnetic field (normally used) or in terms of magnetization. The analysis was validated with available experimental data on structures incorporating Terfenol-D. To model particulate magnetostrictive composites, interactions between particles are captured by combining a numerical micromechanical analysis with the Mori–Tanaka homogenization approach. Pradhan et al.[198] developed first-order shear deformation theory (FSDT) to study vibration control of laminated composite plate with embedded magnetostrictive layers. The effects of material properties and placement of magnetostrictive layers on vibration suppression were examined. It was found that the maximum suppression is obtained when the magnetostrictive layers were relatively thin and placed far away from the neutral axis.

Calkins et al.[199] and Dapino et al.[200] provided an overview of magnetostrictive sensor technology. Magnetostrictive sensors take advantage of the coupling between the elastic and magnetic states of a material to measure motion, stress, and magnetic field. Sensors are classified into three categories: passive, active, and hybrid. Passive sensors are based on Villari effect and measure change in magnet flux in a coil surrounding the sensor caused by an externally imposed stress. Active sensors use an internal excitation of the material (such as with coil) to facilitate the measurement of permeability (often with another coil) caused by an external forcing. Hybrid or combined sensors rely on the use of magnetostrictive element to actively excite another material (say, fiber optic) that allows measurement of change in its properties as a result of external change. Many different sensors based on their applications are discussed and contrasted with conventional sensors in terms of sensitivity and implementation issues. Flatau et al.[201] developed a high-bandwidth-tuned vibration absorber using Terfenol-D actuator and showed a significant change of modulus from demagnetized state to magnetic saturation.[202] Simple experiments were conducted to demonstrate proof of concept. Kellogg and Flatau[203] developed an analysis of the noncontact nature of sensing using magnetostrictives. Kellogg and Flatau carried out systematic measurement of elastic modulus of Terfenol-D under controlled thermal, magnetic, and mechanical loading conditions and showed dramatic change of modulus with the dc applied magnetic field. Because the magnetostrictive materials, especially Terfenol-Ds, are brittle in tension (tensile strength ~ 28 MPa, compressive strength ~ 700 Mpa), they are normally placed under a mechanical compressive prestress. Also, a prestress improves the magnetic state of the material and hence the magnetomechanical coupling. However, a large compressive prestress can overpower the elastic deflections caused by magnetostriction. Under dynamic conditions the performance of magnetostrictive material is affected by eddy currents that produce magnetic flux opposite to externally applied magnetic field (skin effect). Pratt et al.[204] exploited the nonlinear transduction of nonbiased Terfenol-D actuators to design an autoparametric vibration absorber.

Overall, there is a general lack of detailed database for magnetostrictive actuators for a wide range of test conditions.

More in-depth investigations are needed to understand the behavior of magnetostrictive materials under a wide range of controlled operating conditions. For modeling, the least well-defined component is magnetic state of magnetostrictive core, which is function of operating conditions. It is important to develop reliable modeling of magnetization using either micromagnetic representation of material or Preisach model or ferromagnetic hysteresis model. There is a need to develop a comprehensive three-dimensional constitutive model of magnetostrictive materials that include nonlinear thermal effects, magnetization saturation, eddy current losses, prestress, hysteretic behaviors, and dynamic effects and then systematically validate with test data.

B. Electrostrictives

Materials such as relaxor ferroelectrics undergo strain when an electric field is applied. Under this category of materials, lead magnesium niobate (PMN) alloys have a sufficiently large dielectric permittivity that helps to generate significant polarization and hence strains. In the absence of electric field, small electric domains are randomly oriented in these materials. With the application of electric field, these domains rotate, resulting in strain. The variation of strain with electric field is quadratic (independent of polarity of field) (Fig. 49). At a sufficiently high field, the induced strain gets saturated. Unlike piezoelectrics, uncharged electrostrictives are isotropic and are not poled. With an application of field, the materials get instantly polarized and become anisotropic. For example, the transverse material stiffness of PMN-PT decreases by about 20% as the electric field becomes 1300 V/mm. On the removal of field, the materials become depolarized. An electric field produces an extensional strain in the direction of field and contraction in the transverse direction. If the field is reversed, the domains reverse direction, but it again induces an extensional strain in the direction of field (thickness direction). To produce an oscillatory (bidirectional) strain, it becomes necessary to apply a bias dc field. Hence, electrostrictives are used as actuator in a wide range of applications.[205,206] The maximum strain is of the order of 0.1%. Because no permanent polarization is needed for electrostrictives, these are not subjected to electric ageing. They are characterized by very low hysteresis (less than 1%) but are very sensitive to surrounding temperature.[207]

In the absence of an electric field, the material is not polarized. As a result, an application of stress does not change the electric field. Hence, electrostrictives are not normally used as sensors. Because these materials are very sensitive to temperature (thermal environment), most applications of electrostrictives are focused to underwater operations or in vivo, ranging from ultrasonic motors to medical probes. Because of the nonhysteretic nature of this material, it is used in micropositioners. Superior characteristics are obtained when PMN is doped with lead titanate (PT) in low ratio such as 0.9PMN-0.1PT (Ref. 208).

The constitutive relations for electrostrictive material at constant temperature is[209] as follows.

Converse:

$$\varepsilon_{ij} = S_{ijkl}\sigma_{kl} + m_{pqij}E_pE_q$$

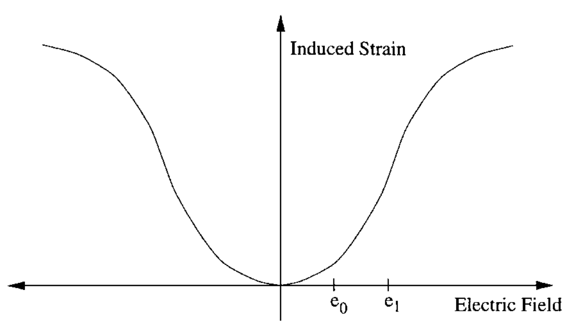

Fig. 49 Strain-electric field distribution for an electrostrictive element.

Direct:

$$D_j = e^T_{jn}E_n + 2m_{jnkl}E_n\sigma_{kl}$$

where D is electric displacement, S is material compliance, E is electric field, m is electrostrictive-coupling parameter similar to piezoelectric coefficient d, and e^T is dielectric permittivity. A factor of two is needed in the electromechanical coupling in the charge equation caused by stress, and this factor is not needed in the strain equation caused by the field. These equations contain moderate nonlinear terms and are valid for low fields (less than 300 V/mm).

Expanding the converse relation,

$$\begin{Bmatrix} \varepsilon_1 \\ \varepsilon_2 \\ \varepsilon_3 \\ \gamma_{23} \\ \gamma_{31} \\ \gamma_{12} \end{Bmatrix} = \begin{bmatrix} m_{33} & m_{31} & m_{31} \\ m_{31} & m_{33} & m_{31} \\ m_{31} & m_{31} & m_{33} \\ 0 & 0 & 0 \\ 0 & 0 & 0 \\ 0 & 0 & 0 \end{bmatrix} \begin{Bmatrix} E_1^2 \\ E_2^2 \\ E_3^2 \end{Bmatrix}$$

The electrostrictive coefficients depend upon the field. Let us say only voltage is applied to top and bottom of electrostrictive surfaces:

$$\varepsilon_1 = \varepsilon_2 = \varepsilon_3 = m_{33}(V/t_c)^2$$

The strain per field is $2m_{33}(V/t_c)$.

Electrostrictives exhibit variable dielectric characteristics with strain (decrease with strain) resulting in a nonquadratic variation of strain with field. On the other hand, the electrostrictive materials show very low hysteresis and creep characteristics. Unlike piezoelectric materials, the performance of electristrictives does not degrade with time. Because their capacitance is high (an order of magnitude more than piezoceramics), internal heating is low.

Fripp and Hagood[210] presented a comprehensive set of constitutive equations for electrostrictive materials and developed a dynamic analysis for an electromechanical system with distributed electrostrictive couplings. A Raleigh–Ritz analysis was formulated for a cantilevered beam actuated with surface-bonded electrostrictive wafers and satisfactorily validated it for static and dynamic response with experimental test data. Hom and Shankar[211,212] presented a fully coupled, two-dimensional, quasistatic finite element analysis for electroceramics and applied it to electrostrictive stack actuators. This formulation incorporates the effect of body forces of dielectric origin, but ignores the body moments of dielectric origin. Recently, Pablo and Petitjean[208] carried out stress free electric behavior (in transverse direction) of electrostrictive patches experimentally at a macrolevel for a range of excitation fields and frequencies and temperatures. Piquette and Forsythe[213] covered nonlinear modeling of PMN materials. Most of the existing studies are quite restrictive is scope and applications.

More detailed investigations are required to understand the performance of these actuators under a wide range of operating conditions. Simplified constitutive models of materials need to be developed covering a range of fields, strains, and temperatures and validated with experimental data obtained under controlled test environments.

VII. Applications

Applications of smart-structures technology to various physical systems are focused to actively control vibration, performance, noise, and stability. Applications range from space systems to fixed-wing and rotary-wing aircraft, automotive, civil structures, marine systems, machine tools, and medical devices. Early applications of smart-structures technology were focused to space systems to actively control vibration of large space structures[31] as well as for precision pointing in space (telescope, mirrors, etc.[214]) The scope and potential of smart-structures applications for aeronautical systems are expanding. Embedded or surface-bonded smart material actuators on an airplane wing or helicopter blade can induce alteration of twist/camber of airfoil (shape change), which, in turn, can cause variation of lift distribution and might help to control static and dynamic aeroelastic problems. For fixed-wing aircraft, applications cover active control of flutter,[215–219] static divergence,[220,221]

Table 7 Comparative test evaluation of commercially available piezostack actuators[232]

Part/material no.	Operating voltage, V	Maximum strain, μ strain	Block force (BF), lb	Normalized block force, ksi	Strain-force index	Energy density, ft-lb-slug
MM 8M (70018)	360	254	128	1.05	0.133	1.27
MM 5H (70023-1)	200	449	101	0.83	0.180	1.80
MM 4S (70023-2)	360	497	143	1.17	0.291	2.78
PI P-804.10	100	1035	1133	7.31	3.783	36.72
PI PAH-018.102	1000	1358	1505	9.71	6.593	62.95
XI RE0410L	100	468	95	5.16	1.207	11.52
XI PZ0410L	100	910	70	3.58	1.629	15.55
EDO 100P-1 (98)	800	838	154	2.00	0.838	8.00
EDO 100P-1 (69)	800	472	50	0.66	0.156	1.49
SU 15C (H5D)	150	940	266	7.48	3.516	33.57
SU 15C (5D)	150	1110	274	7.70	4.274	40.80

panel flutter,[222] performance enhancement,[223] and interior structure-borne noise.[224] Compared to fixed-wing aircraft, helicopters appear to show the most potential for a major payoff with the application of smart-structures technology. Given the broad scope of smart-structures applications, developments in the field of rotorcraft are highlighted in this section. Although most of current applications are focused on the minimization of helicopter vibration, there are other potential applications such as interior/exterior noise reduction, aerodynamic performance enhancement including stall alleviation, aeromechanical stability augmentation, rotor tracking, handling qualities improvement, rotor head health monitoring, and rotor primary controls implementation (swashplateless rotors) (see review paper[30]). For aerospace systems two types of actuation concepts have been incorporated. One approach uses active materials directly, surface-bonded or embedded, to actively twist or camber control of lifting surface. Another approach actively controls auxiliary lifting devices such as leading-/trailing-edge flaps using smart material actuators. Currently, a major barrier is the limited stroke of smart actuators, requiring a large amplification.

A. Stroke Amplification

For most applications there is a need for compact, moderate force, moderate bandwidth, and large displacement actuators. Most actuators, in particular piezoceramic actuators, are low force and low stroke devices. Typically, piezoceramic sheet actuators generate free displacements from 1 to 5 μm and block forces from 2 to 20 lb (1 lb = 453.6 g) and frequencies up to 20 kHz. Individual piezoelectric sheet actuators can be combined in series to obtain higher actuation displacement. The actuation force is however unaffected, and also, there is a limit on increasing the length of thin sheet actuators (buckling constraint). Another approach to increase the actuation displacement is by building piezoelectric bimorphs. A bimorph or bending actuator consists of two or more even layers of piezoelectric sheets bonded on either side of a thin metallic shim (main load carrying member). By applying an opposite potential to top and bottom sheets, a pure bending actuation is generated. In a cantilevered arrangement the tip displacement can be used for actuation of a system. With piezobimorph one can obtain displacements from 5 to 10 μm and forces up to 0.5 lb. Using more layers can increase the actuation force, but the displacement is reduced. To increase actuation force, multilayered actuators such as piezostacks can be used. However, the stroke of piezostacks is quite small. A key challenge is to amplify the stroke of these actuators. Large mechanical amplification using a compact leverage system often leads to substantial losses at hinges and slippage at knife edges. Replacing mechanical hinges with flexure can overcome some of these problems, but requires large effort and experience to perfect such systems. Also, the actuation efficiency is reduced. To amplify the stroke of piezodevices, specially shaped actuators are being built. Typical examples include reduced and internally biased oxide wafers (RAINBOW) actuators, thin-layer composite unimorph ferroelectric driver and sensor (THUNDER) actuators, Moonie actuators, and C-block actuators. RAINBOW are dome-shaped actuators that are built by bonding piezoceramic layer and a chemical reduced layer (acts like a shim).[225] The piezoelectric layer is on the convex side, and an electric field changes the curvature of the actuator. The projected free displacements are of the order of 1000 μm, forces up to 100 lb, and actuation frequency up to 10 KHz. By stacking RAINBOWs in a clamshell configuration, it is possible to obtain higher stroke.[226,227] THUNDER actuator is a curved shaped device composed of a metallic layer bonded to a prestressed piezoelectric layer.[228] Displacement is achieved via the induced d_{31} contraction. A cantilevered 1×0.5 in. actuator can generate the displacement of 10 mils and a block force of 8 lb. The Moonie actuator consists of metal-ceramic composite, composed of a piezoelectric ceramic disk sandwiched between two metal end caps. The end caps act as stroke amplifiers of lateral displacement of the PZT sheet.[229] C-block actuators are multilayered arched bimorph piezoelectric actuators, and a large axial displacement can be achieved using a series arrangement of C-actuators.[230,231] So far, most of these specially shaped actuators have not been exploited into challenging applications. Many of these actuators are in their early state of development and lack rigorous modeling and database.

For many practical applications it is necessary to develop large strokes. To increase actuation force, multilayered piezostack actuators are used. These consist of a large number of thin piezoelectric sheets stacked in a series arrangement, separated by electrodes that make use of induced strain in thickness direction (d_{33} actuation). These devices induce small free displacements but much larger actuation force than sheet actuators. Nominal performance of piezostack actuators range in free displacement from 15 to 25 μm, block forces up to 1000 lb, and frequencies up to 20 kHz. Combined with suitable amplification mechanism, piezostacks have been used in a wide range of applications. There have been several studies to characterize the electromechanical behavior of peieostacks.[232–235] For example, Lee[232] evaluated the characteristics of 11 different stack actuators including maximum free strain, maximum block force, operating voltage, and energy density (Table 7). These actuators were tested systematically using specially built test apparatus under different field levels, operating frequencies, and preloads.

To increase the stroke of piezostack actuators, some form of amplification mechanism is needed. Current amplification mechanisms can be divided into two types: fluidic and mechanical. Typically, fluidic approaches use two cylinders of different diameters to obtain desired amplification of stroke. Although fluid amplifiers might provide higher amplification than mechanical devices, they suffer from fluid losses, weight penalty, and complexity of system.[236,237] So far, there has been limited success with these devices. Mechanical amplification can be categorized into two types: rigid lever/frame amplifiers[238–241] and elastic flextensional amplifiers.[242,243] These amplification devices trade force with displacement, but have a detrimental effect on power transfer efficiency and energy density.[244,245] Several single-stage mechanical amplification devices that include lever-fulcrum mechanism (Fig. 50) and triangular frame mechanism have been built to actuate a trailing-edge flap of a rotor blade. In comparison to fluidic devices, these provide simple, lightweight, and efficient amplification systems. However, they suffer from the degradation of performance caused by losses (stiffness and power) especially with high amplification factor. From the stiffness point of view, the triangle frame system is normally more efficient than the lever-fulcrum system because its structural members experience mostly extensional loads in contrast to bending loads for lever-fulcrum amplifiers (Table 8). However, the stiffness of the lever-fulcrum can be maintained at much higher value but with

Table 8 Comparison of mechanical amplification concepts[246]

Concept	Lever-fulcrum	Triangle frame
Amplification factor	<10	<10
Existing actuators	Physik instruments Boeing biaxial actuator UM leverage amplification UM L-arm amplification UM L-L amplification	SatCon flap actuator MIT X-Frame actuator
Scaling up	Constant lever ratio	Constant lever ratio
Special features	Design flexibility	Small chordwise size
Disadvantage	Elastic deformation caused by bending	Lateral vibration of piezostacks
Design enhancements	Multiple-stage amplification	Different frame material

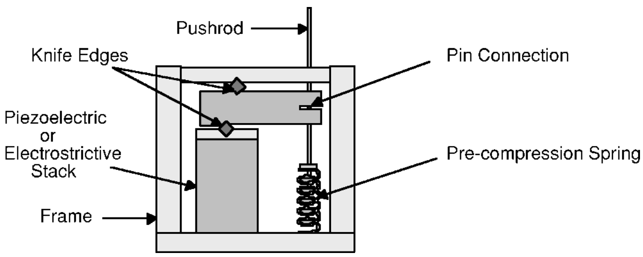

Fig. 50 Leverage amplification.

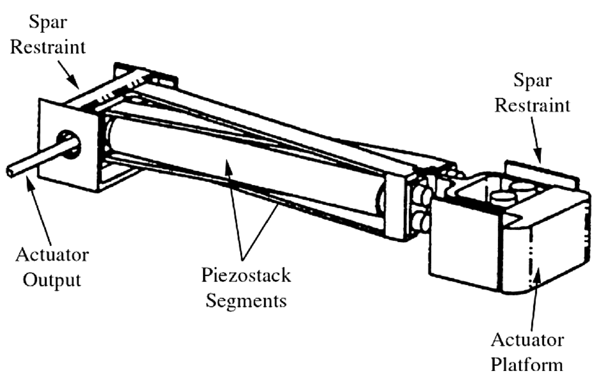

Fig. 51 X-Frame actuator schematic.[244]

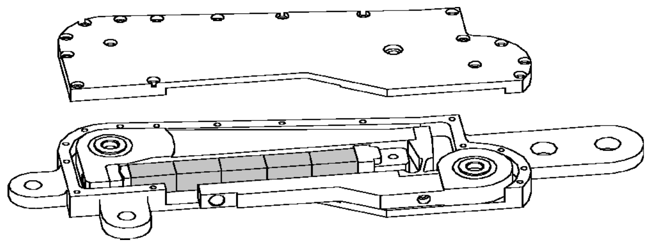

Actuator layout

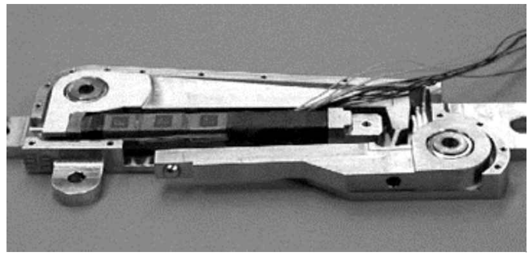

Fabricated actuator

Fig. 52 L-L amplification mechanism.[232]

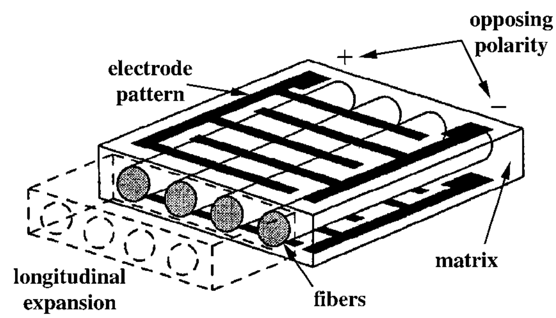

Fig. 53 Active piezofiber composites.

a weight penalty. For design refinements including scale-ups, the lever-fulcrum appears superior to the triangle frame system (free from geometrical constraints). To achieve higher amplification factors (say, over 10), multistage amplification is incorporated such as in L-L amplification mechanism.[246] It is a combination of lever-fulcrums and elastic linkages. The stroke of piezostacks is amplified by an inner lever with a low amplification factor (<6) and then amplified again by the outer lever. Two lever-fulcrums are connected in series using an elastic linkage that also provides returning force as well as piezostack preload. To achieve bidirectional functionality, it becomes necessary to build dual-stage amplifiers, respectively implemented in full-scale X-frame actuator (Fig. 51) and L-L actuator (Fig. 52). There are other flextensional amplification devices, such as oval-shaped actuators, Moonies, and oysters,[232] that might be more beneficial in specific applications. A typical stroke amplification factor of about five is achieved by sacrificing the load-carrying capacity.

To overcome losses with pin-jointed amplification mechanism, flexure hinges or fully complaint mechanisms are used. Often, ad-hoc design procedures are used to develop these devices. As a result, the final design might not be optimal. Frecker and Canfied[247] formulated a systematic topology optimization approach to the design of complaint mechanical amplifiers for piezoceramic stack actuators. In this approach, any direction of force and motion transmission from the active material can be chosen. This methodology appears to show potential to build devices with precise motions.[248,249]

For actuation of trailing-edge flaps of wings/rotor blades and other application, it is necessary to convert the linear displacement into angular displacement. A mechanical conversion can significantly reduce the effectiveness of the device. Bothwell et al.[250] used extension-torsion coupling of a thin-walled composite tube to convert linear motion of magnetostrictive actuator into torsional motion to actuate a trailing-edge flap. This device appears less meritorious because of low actuation efficiency. Bernhard and Chopra[251] used bending-torsion coupling of composite beam in conjunction with surface-bonded piezoelectric elements and voltage phase to convert bending into twisting to actuate blade tip. This concept appears promising for scaled rotor models. Giurgiutiu and Rogers[234] used the twist-warping concept of the thin-walled open tube to convert linear motion of PZT stacks into rotary motion. This device suffers from low actuation efficiency and low load-carrying capability.

One can achieve a large induced strain in the d_{15} shear mode. For example, for PZT-5H, d_{31}, d_{33}, and d_{15} are -274, $+593$, and $+741$ pm/V. However, it is extremely difficult to build a practical actuator in this mode. Recently, a segmented torsional tube actuator operating in the d_{15} mode was developed and tested.[252,253] There are two major drawbacks with this actuator. It requires high voltage (several kilovolts), and it requires special conductors to apply field. One revolutionary development in piezoceramics has been the emergence of piezofibers in the form of active plies by Hagood and his group (Fig. 53).[254–256] The piezofibers are actuated in the d_{33} mode using interdigitated electrodes. The piezo active fibers have been used successfully in the development of active twist rotor.[257–261]

There are other potential high-stroke actuators that need further investigation to examine their projected amplifications.[232,262]

B. Actuator Performance

looseness-1Irrespective of amplification mechanism, the actuator output energy is less then the available active material strain energy because of several different losses. Consider a piezostack of length l_c with external spring load K_e (Fig. 54). The support structure is assumed as rigid. The stack is characterized with two important parameters: maximum free displacement u_{free} (or Λl_c) and maximum block force F_{bl}.

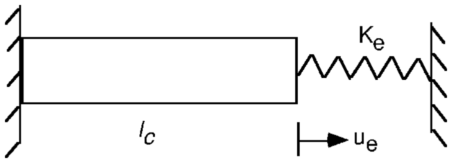

Fig. 54 Rigid support.

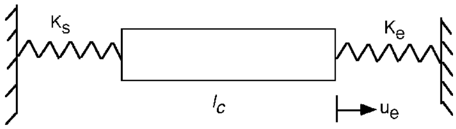

Fig. 55 Flexible support.

The elastic deflection is

$$u_e = u_{\text{free}} - (k_e u_e / E_c A_c) l_c$$

where $E_c A_c$ is extensional stiffness of stack actuator. Rewriting

$$u_e = \frac{u_{\text{free}}}{1 + k_e l_c / E_c A_c}$$

Defining stiffness ratio r as

$$r = \frac{k_e l_c}{E_c A_c} = \frac{\text{external stiffness}}{\text{internal actuator stiffness}}$$

Output energy U_0 is

$$\begin{aligned} U_0 &= \tfrac{1}{2} K_e u_e^2 \\ &= [r/(1+r)^2]\left[\tfrac{1}{2}(E_c A_c / l_c) u_{\text{free}}^2\right] \\ &= [r/(1+r)^2] U_{\max} \end{aligned}$$

where $U_{\max}$ represents the maximum strain energy possible from an actuator. Actuator efficiency η is defined as

$$\eta = U_0 / U_{\max} = r/(1+r)^2$$

where $r = 0$ represents a free condition and actuator efficiency is zero. The parameter r approaching infinity represents a blocked condition, and again the actuator efficiency is zero. Maximum efficiency is achieved with $\eta = 1$, which represents the matched stiffness condition (external stiffness equals actuator stiffness). For this case a maximum output energy is achieved, and actuator efficiency η becomes equal to $\frac{1}{4}$ (Ref. 236).

Let us next consider an elastic support structure with stiffness K_s (Fig. 55).

The elastic deflection is

$$u_e = u_{\text{free}} - (k_e u_e / E_c A_c) l_c - K_e u_e / K_s$$

Rewriting results in

$$u_e = u_{\text{free}} / (1 + k_e l_c / E_c A_c + K_e / K_s)$$

Let us define support stiffness ratio r_s:

$$r_s = \frac{k_s l_c}{E_c A_c} = \frac{\text{support stiffness}}{\text{actuator stiffness}}$$

Thus, elastic deflection becomes

$$u_e = u_{\text{free}} / [1 + r(1 + 1/r_s)]$$

Output energy is

$$\begin{aligned} U_0 &= \tfrac{1}{2} K_e u_e^2 \\ &= \left\{ r \big/ [1 + r(1 + 1/r_s)]^2 \right\} U_{\max} \end{aligned}$$

Actuator efficiency is

$$\eta = r \big/ [1 + r(1 + 1/r_s)]^2$$

Optimum actuation efficiency is achieved by setting $\mathrm{d}\eta/\mathrm{d}r = 0$, which results in

$$\eta_{\text{opt}} = \tfrac{1}{4}[r/(1 + r_s)]$$

Now the actuation efficiency depends on both output stiffness ratio r and support stiffness r_s. The $r_s = 10$ represents a case where the support stiffness is 10 times the actuator stiffness, and it is quite close to the rigid support case. For a flexible support case (say, $r_s = 1$) there is not only reduction of actuator efficiency, but there is also reduction of r at which maximum efficiency takes place. For this case there is a reduction of maximum output energy by 50%. It is clear that now half of the available energy is dissipated by the support system. To improve the actuation efficiency, it is important to increase the stiffness of supporting structure, which in turn increases the weight of the system. Another important and practical index of efficiency should be to consider the mass of supporting and active structures. Let us define active material energy density ratio as

$$\eta_{\text{mass}} = (U_0 / U_{\max})(M_{\text{act}} / M_{\text{tot}})$$

where M_{act} is the mass of actuator and M_{tot} is the total mass of structure including frame, supporting structure, and active systems. This efficiency helps to evaluate different actuation mechanisms, especially under static conditions.

C. Leverage Amplification

A leverage system is used to amplify the actuator stroke (Fig. 56). Let us imagine that the output displacement at point B is u_e and external load is represented by a linear spring of stiffness constant K_e.

The effective displacement at point A is

$$u_i = u_{\text{free}} - F l_c / E_c A_c$$

where $E_c A_c$ is the axial stiffness of actuator and F is the actuation force at point A. The external deflection at point B is

$$\begin{aligned} u_e &= u_i (l_2 / l_1) \\ &= (l_2/l_1)[u_{\text{free}} - (K_e l_c / E_c A_c)(l_2/l_1) u_e] \end{aligned}$$

Let us define the leverage amplification by G

$$G = l_2 / l_1$$

and stiffness ratio by r

$$r = K_e l_c / E_c A_c$$

The output energy U_0 is

$$\begin{aligned} U_0 &= \tfrac{1}{2} K_e u_e^2 \\ &= \tfrac{1}{2}[K_e/(E_c A_c / l_c)][G^2/(1 + G^2 r)^2](E_c A_c / l_c) u_{\text{free}}^2 \end{aligned}$$

The actuation energy efficiency is

$$\begin{aligned} \eta &= \frac{\tfrac{1}{2} K_e u_e^2}{\tfrac{1}{2}(E_c A_c / l_c) u_{\text{free}}^2} \\ &= \frac{r G^2}{(1 + r G^2)^2} \end{aligned}$$

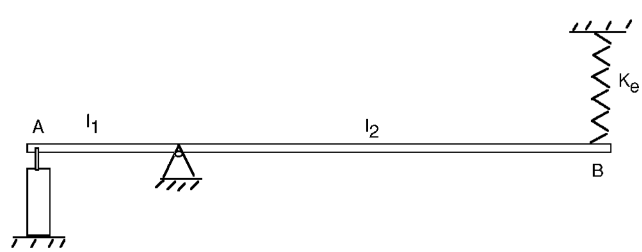

Fig. 56 Leverage amplification.

The actuation energy efficiency depends upon stiffness ratio r and leverage amplification ratio G. An optimal value is obtained by setting $d\eta/dr = 0$, which results in

$$r_{\text{opt}} = 1/G^2, \qquad \eta_{\text{opt}} = \tfrac{1}{4}$$

The maximum value of energy efficiency can be $\frac{1}{4}$. Because G is greater than 1, the maximum energy transfer occurs when the output stiffness is lower than actuator stiffness. For $G = 1$ (no stroke amplification) r_{opt} becomes equal to 1.0 (matched stiffness condition). The optimal value of r decreases rapidly as G increases.

To cover the effect of mass, the active material energy density ratio is defined as

$$\eta_{\text{mass}} = \frac{U_0}{U_{\max}}\frac{M_{\text{act}}}{M_{\text{tot}}}, \qquad \eta_{\text{mass}} = \frac{rG^2}{(1+rG^2)^2}\frac{M_{\text{act}}}{M_{\text{tot}}}$$

D. Comparison of Actuators

There is a wide variation of characteristics among different smart material actuators. Hence, it becomes important to make a comparative evaluation of their characteristics. Many applications require moderate force and large displacement at low frequencies (say less than 100 Hz). Stroke amplification devices trade force with displacement; however, energy per cycle remains constant. If the actuator is operating at the same frequency, the total work per cycle might not be sufficient for a specific application. One way to increase the power output of the actuation device is to operate it at a higher frequency than the operation frequency and harness more energy per cycle. However, this requires frequency rectification to achieve the desired actuator output frequency independent of piezodrive frequency. Thus, the amount of work from an actuator is maximized through impedance matching with load, whereas the power is maximized by increasing its frequency. Devices like inchworm motors, ultrasonic motors, micropulse actuators, and piezohydraulic pump are all based on this principle. The piezohydraulic pump appears to show the most potential among these devices and is discussed next.

There have been attempts to develop hybrid hydraulic actuation systems to amplify the stroke of piezostack actuators.[263–265] It is a stepwise actuation concept to provide moderately large force and stoke. Typically, it consists of two parts: a pump driven by piezostack actuators that pumps fluid from a low-pressure accumulator to a high-pressure accumulator and an output hydraulic actuator driven by Whetstone bridge network of valves that use the pressure differential created in the accumulators. The high-frequency energy of the piezoelectric stack is exploited by using valves. Sirohi and Chopra[266,267] built a prototype pump driven by two piezostack actuators (Fig. 57). The stack displaces a piston of diameter 1 in. (25.4 mm), which is bonded to a thin steel diaphragm that provides a leakproof seal and a restoring spring force. Two passive ball-type check valves were installed on the pumping head to direct flow to and from high-capacity accumulators. The piezostacks were actuated at frequencies of 10–250 Hz by a sinusoidal voltage of amplitude 50 V. The results showed that the differential pressure created between accumulators increases with actuation frequency and reaches the maximum at 150 Hz. Beyond this frequency the pressure differential falls. A maximum temperature of 55°C was measured on the piezostack. There are two major challenges with the successful development of this device, operation of control valves at high frequencies, and temperature control of piezostack at high fields and frequencies.

E. Piezoactuation Power Reduction

The piezoelectric and electrostrictive actuators exhibit highly capacitive electrical characteristics. If a sinusoidal voltage is applied to an ideal capacitor, the charge during the positive half-cycle of excitation equals the discharge during the negative half-cycle, and hence the net energy dissipation in one cycle is zero. For a nonideal capacitor (capacitor and resistance in series) there is a net energy dissipation by the resistance as a result of ohmic heating. As a result, a typical amplifier requires a large heat sink. This power is called active power:

$$P_{\text{active}} = V \times I \times \cos\phi \text{ W}$$

where V is voltage, I is the current drawn in amperes, ϕ is the phase lag of current with respect to voltage, and $\cos\phi$ is called the power factor of the circuit. To make the most efficient use of power supply, the power factor should be close to unity. The size and weight of the amplifier are determined by the amount of reactive power it generates. The power factor correction is achieved by adding an inductance in the circuit. This can be achieved in two different ways: in series and in parallel with the capacitance (Fig. 58).

The net impedance of the series configuration is

$$\bar{Z}_{\text{total}} = R + \frac{j(\omega^2 LC - 1)}{\omega C}$$

and the impedance of the parallel configuration is

$$\bar{Z}_{\text{total}} = R + \frac{j\omega L}{1 - \omega^2 LC}$$

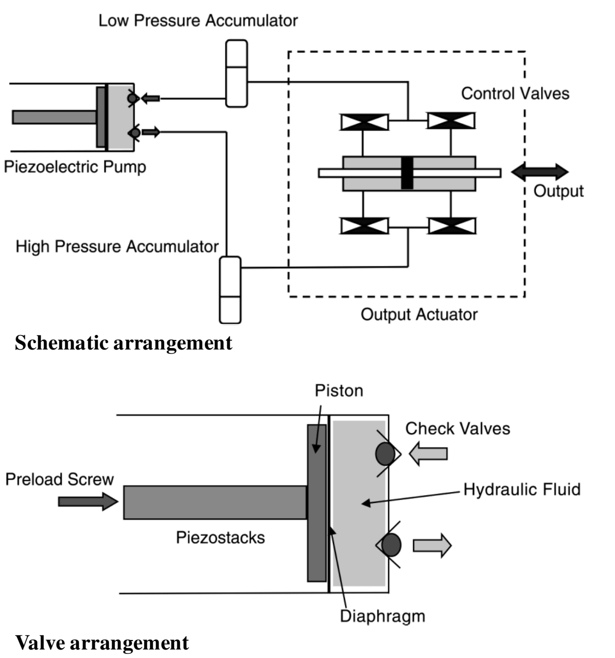

Fig. 57 Actuation schematic of piezoceramic pump.

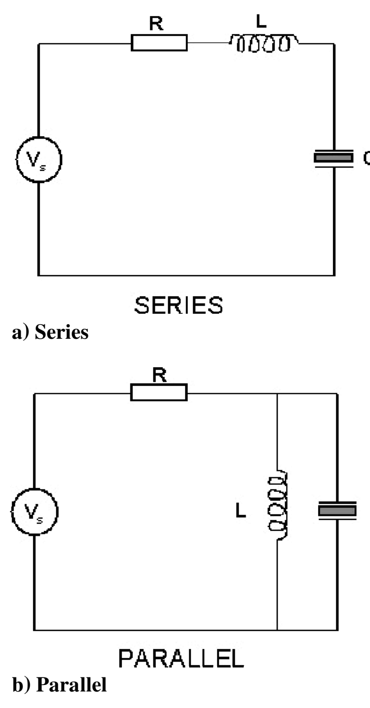

Fig. 58 Series and parallel resonant circuits.

where ω is frequency of excitation. The resonant frequency is defined as

$$\omega_0 = 1\big/\sqrt{LC}$$

At the resonant frequency, the impedance of series circuit becomes purely resistive, and the power factor equals unity. At this condition energy is continuously transferred between the inductor (energy storage as a magnetic field) and capacitor (energy storage as an electric field). The only energy dissipation is through the resistive losses. In a parallel circuit, the impedance approaches infinity at the resonant condition; there is no voltage drop across the resistor. The voltage across the actuator is the same as the power supply voltage, and the net current drawn from the power supply is nearly zero. This appears more attractive because the power supply can be quite compact.

In reality, the piezoelectric actuator is a nonideal capacitance and can be modeled as an ideal capacitor in series with a resistor. Normally, the resistance for a PZT actuator is function of excitation frequency and decreases with higher frequency.[268] Even though the resistance is negligible as compared to the impedance of capacitor, it has a significant effect on system performance.

Following the parallel circuit for a nonideal capacitor and inductor, its performance is evaluated. As shown in Ref. 268, to make the impedance of this circuit totally resistive, the frequency has to be ω_{01}:

$$\omega_{01} = \frac{L - R_l^2 C}{\left(L - R_c^2 C\right) LC}$$

Note that the capacitance of a typical PZT sheet actuator (size $2 \times 1 \times 0.010$ in.) ($50.8 \times 25.4 \times 0.254$ mm) is of the order of 150 nF, whereas the capacitance of a typical piezostack actuator is of the order of 7 mF. There are three possible cases to achieve this condition. For a general case of $R_l \neq 0$, $R_c \neq 0$, there is a maximum allowable value of R_l:

$$R_l \leq 1/2C\omega_0$$

The required value of inductance increases rapidly for the low value of actuator capacitance and excitation frequency. In practice, it is difficult to obtain physical inductance in the range of tens of henries. Physical inductance of such a magnitude tends to be bulky and heavy and makes it impractical to integrate in a smart system. Such inductors also tend to have a high value of resistance. Further, the requirement of inductance changes with frequency and as a result requires continuous tuning of the circuit. To overcome these problems, the concept of pseudoinductance is introduced.

Pseudoinductance is an active inductor created using an operational amplifier. It is compact, and an inductance value of the order of 100 H can be achieved. The amplifier changes the phase of the current flowing through the circuit so that the equivalent impedance is inductive. Also, the value of inductance can be easily adjusted by changing the values of the capacitance or the resistance in the circuit using a potentiometer (Fig. 59). The major disadvantage of pseudoinductance is that the power amplifier requires another power supply (dc) for its functioning. However, it should be noted that the reduction of the ac power requirement generally will result in a lower overall power and weight of the combined reduced ac power supply and the pseudoinductance dc power supply. Sirohi and Chopra[268] implemented a pseudoinductance system by connecting it parallel to a stack actuator. Figure 60 shows test results of power saving obtained by connecting a 100-H pseudoinductor in parallel with a

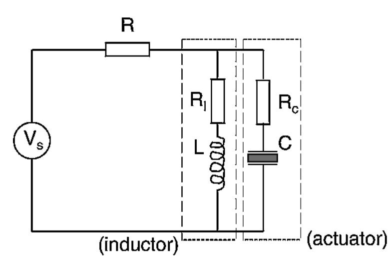

Fig. 59 Nonideal resonant drive circuit with pseudoinductor.

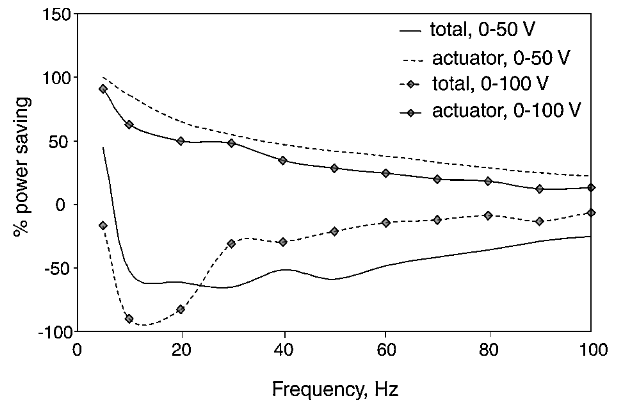

Fig. 60 Power savings obtained by continuous tuning, for a 7uF actuator.[268]

stack actuator of capacitance 7 mF by continuously tuning the circuit. Two different excitation voltages are shown: 0–50 and 0–100 V, for which the circuit supply voltages are 75 and 125 V_{dc}, respectively. A current saving of 70% has been obtained under a normal operating condition at 20 Hz. The power saving decreases with frequency. At higher frequencies and excitation fields, although the actuator power saving is still significant, the overall power saving might become negative.

Another approach to save actuation power is to use switching amplifiers.[269–271] Simulations have shown enormous potential of weight saving with this scheme.

F. Rotorcraft Applications

More than any other system, the structural, mechanical, and aerodynamic complexity and the interdisciplinary nature of rotorcraft offer numerous opportunities for the application of smart-structures technologies with the potential for substantial payoffs in system effectiveness. Compared to fixed-wing aircraft, helicopters suffer from severe vibration and fatigue loads, more susceptibility to aeromechanical instability, excessive noise levels, poor flight stability characteristics, and weak aerodynamic performance. The primary source for all of these problems is the main rotor, which operates in an unsteady and complex aerodynamic environment leading to stalled and reversed flow on the retreating side of the disk, transonic flow on the advancing blade tips, highly yawed flow on the front and rear part of the disk, and blade-vortex interactions in certain flight conditions. Currently, considerable research is focused on the application of smart-structures technology to rotor systems to improve their performance and effectiveness. Three types of smart-rotor concepts are under development: leading- and trailing-edge flaps actuated with smart material actuators, controllable camber/twist blades with embedded piezoelectric elements/fibers, and active blade tips actuated with tailored smart actuators. The performance of these actuation systems degrades rapidly at high rotational speeds because of large centrifugal force, dynamic pressure, and frictional moments. For flap actuation, actuators range from piezobimorphs, piezostacks, and piezoelectric/magnetostrictive-induced composite coupled systems. These concepts have been demonstrated on scaled rotor models such as Froude and Mach scaled (Fig. 61) and are currently being incorporated in full-scale rotor systems. Most smart material actuators are moderate force and extremely small stroke devices, and hence some form of mechanical/fluidic/hybrid amplification of stroke is needed to achieve practicable flap deflections. Because of compactness and weight considerations, the stroke amplification mechanism and high-energy density actuators have been key barriers for application to rotor blades.

Koratkar and Chopra[272–274] built 6-ft-diam (1.83-m-diam) dynamically scaled rotor models with trailing-edge flaps actuated with multilayered piezobimorphs. Initially Froude-scaled rotor models were built and successfully tested in a vacuum chamber and on a hover tower, and finally, Mach-scaled rotor models were demonstrated in closed-loop testing in the wind tunnel. The flaps spanned about 10% of rotor radius and were centered at 75% of blade length and showed over ±5-deg deflection at 4/rev excitation using 3:1 ac

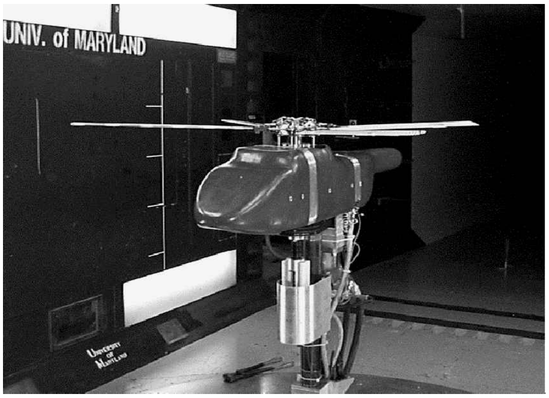

a) Piezobimorph-actuated flap: 6-ft-diam rotor model test in Glenn L. Martin wind tunnel; successfully tested in both open- and closed-Loop studies

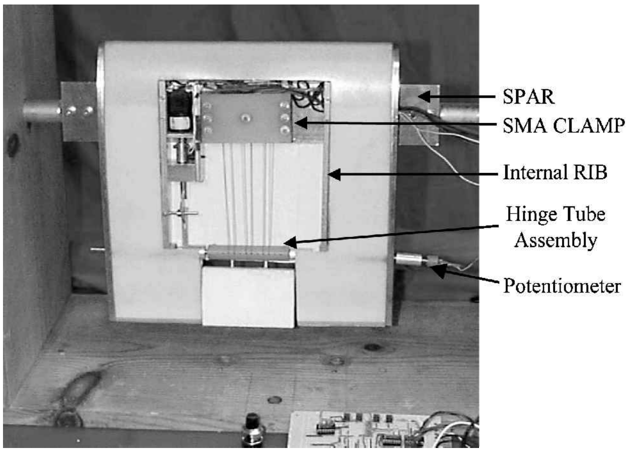

b) Blade-tab-actuated with shape memory alloys actuator, wing section tested in open-jet wind tunnel; produced tab deflections of over 20 deg

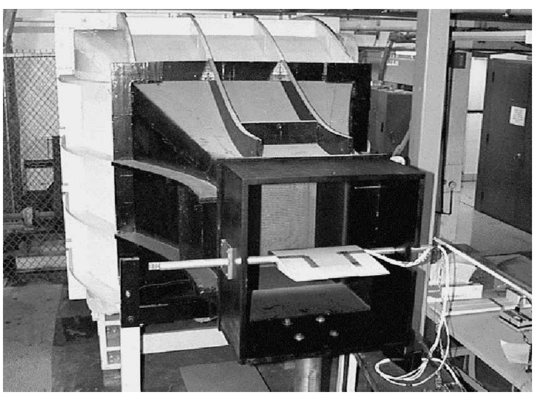

c) Piezostacks-actuated flap: full-scale wing section model tested in open-jet wind tunnel; produced ± 6-deg flap deflection

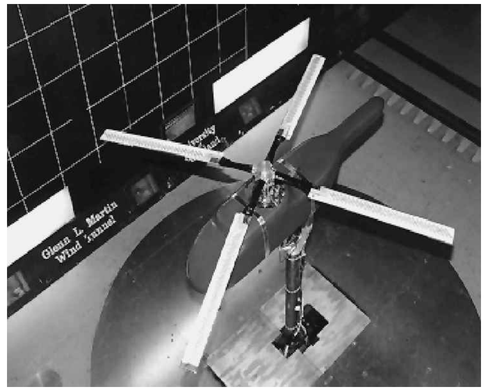

d) Active twist blade with embedded piezoactuators 6-ft-diam rotor test in Glenn L. Martin wind tunnel; produced ± 0.5-deg blade twist up to 5/rev excitation

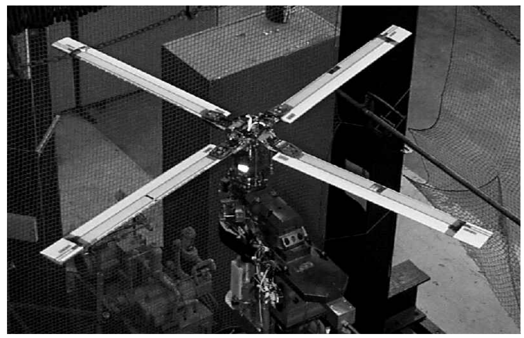

e) Smart tip rotor model (diam 6 ft) on hover stand, actuated with composite bending-torsion coupling and piezos; produced ± 2 deg tip deflections up to 5/rev

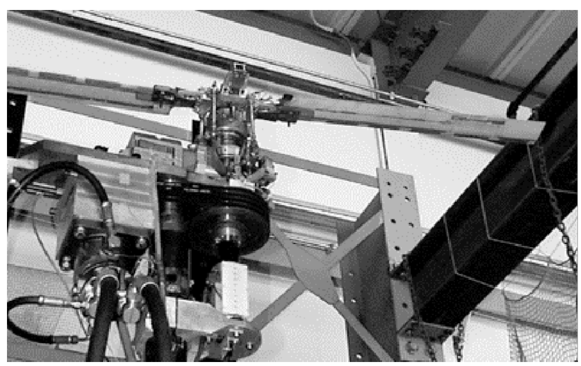

f) Froude-scale rotor model (6 ft diam) on hover tower with piezobimorph-actuated flaps

Fig. 61 Smart rotor development at Alfred Gessow Rotorcraft Center.

bias at an rpm of 2150. Using a neural-network-based adaptive feedback controller, individual blade control resulted in over 80% reduction in vibratory hub loads in the Glenn L. Martin wind tunnel. A Froude-scaled rotor model was also tested successfully in an open-loop investigation by Fulton and Ormiston.[275]

Lee[232] and Lee and Chopra[238,246,276] built a model of blade section of length 12 in. and chord 12 in. (1 in. = 25.4 mm) with trailing-edge flap (span 4 in. and chord 3 in.) actuated with piezostacks in conjunction with double-lever (L-L) amplification mechanism. The model was tested in a vacuum chamber to simulate the full-scale centrifugal field (600 g) and showed a desired stroke-amplification factor of about 20 at all rotor harmonics (up to six). The model was tested in an open-jet wind tunnel and successfully demonstrated flap performance of about ± 10 deg at 120 ft/s. To improve bidirectional performance of this actuation device, a dual L-L amplification system was built and successfully tested in vacuum chamber and in wind tunnel. This new actuation system showed a significant improvement in flap performance at different operating conditions.[276] Straub et al.[277] are building a full-scale smart rotor system for the MD-900 Explorer (five-bladed, 34-ft-diam) with piezostack actuated flaps to actively control its vibration and noise. To amplify the stroke of piezostacks, a biaxial X-frame mechanism is incorporated. The system will be tested in both open- and closed-loop flight investigations. Hall and Prechtl[278] built $\frac{1}{6}$th Mach-scale rotor model with trailing-edge flaps actuated with X-frame actuators and successfully tested on a hover stand. Flap deflections of ± 2.4 deg were achieved. Also, Janker et al.[242] developed a novel piezostack-based flexural actuator for actuation of trailing-edge flaps.

Bernhard and Chopra[279–281] built 6-ft-diam Mach-scaled smart active blade-tip (10%) rotor actuated with piezoinduced bending-torsion coupled composite beam. A novel spanwise variation in ply layup of the composite beam and phasing of surface-mounted piezoceramic actuators is used to convert the bending-torsion coupled beam into a pure twist actuator. At 2000 rpm in hover, blade-tip pitch deflections of 1.7–2.9 deg were achieved at the first four harmonics (for an excitation of 125 V_{rms}). The associated changes in blade lift corresponded to an aerodynamic thrust authority up to 30%. This concept appears promising as an auxiliary device for partial control of noise and vibration.

Chen and Chopra[282,283] built a 6-ft-diam Froude-scaled rotor model with controllable twist blades. For this concept banks of specially shaped (large aspect ratio) multilayered piezoceramic elements were embedded at ±45 deg relative to blade axis respectively over the top and bottom surfaces; an in-phase activation resulted in pure twist in the blade. The model was successfully tested on a hover stand and in the Glenn L. Martin wind tunnel. A tip twist of the order of ±0.4 deg at 4/rev was obtained in both hover and forward flight ($\mu = 0.33$) that amounted to over 10% rotor thrust authority. Although the oscillatory twist amplitudes attained in the forward flight experiments were less than the target value (1 deg of tip twist for complete vibration suppression), it showed the potential for partial vibration suppression. Rogers and Hagood[257,258] and Derham and Hagood[259] built a controllable-twist Mach-scaled rotor by embedding active fiber composite (AFC) and tested on a hover stand. Even though it did not achieve the projected tip twist of ±2 deg, it showed enormous potential for full-scale rotor applications. Cesnik et al.[284] and Cesnik and Shin[285] further improved this technology and successfully tested a Mach-scaled rotor model with embedded active fibers in the transonic dynamics wind tunnel in both open-loop and closed-loop investigations. They have also refined analytical tools related to this rotor system.

Shape memory alloys (SMA) show enormous potential in providing large induced strains (up to 6%), but are limited to low-frequency (less than 1 Hz) applications such as tab adjustment for rotor tracking. Epps and Chopra,[286,287] systematically investigated the development of an SMA-actuated trailing-edge tab for in-flight blade tracking. They built a model of blade section of span and chord of 12 in. with a tab of span 4 in. and chord 2.4 in. actuated with two to five nitinol wires of diameter 0.015 in. respectively both on top and bottom surfaces. To lock the tab at a desired angle (in power-off condition), a gear-locking mechanism consisting of spur gears, pulling solenoid, and pawl was built. A displacement feedback controller was developed to fine tune the tab deflection in about 10 s. This wing section was tested in the open-jet wind tunnel, and tab deflections of the order of 20 deg were obtained at a speed of 120 ft/s. This concept appears promising for full-scale rotor tracking. Recently, Singh and Chopra[288] improved this design and successfully tested it in the wind tunnel for a repeatable open-loop and closed-loop performance.

There are other potential applications of smart-structures technology to rotary-wing systems that might result in enormous payoff in terms of performance improvement and cost saving. These include external noise suppression,[289] internal noise suppression,[290] primary rotor controls,[291,292] performance enhancement including dynamic stall delay,[293] active transmission mounts,[294,295] and active/passive damping augmentation.[296–298]

VIII. Summary

The summary of the state of the art as presented in the paper together with recommendations for future work are as follows:

A. Development of Large Stroke Smart Actuators

At this time most of the commercially available smart material actuators (such as piezoceramics and magnetostrictors) are low stroke and low force devices. For most applications there is a need for compact, moderate force (about 100 lb), moderate bandwidth (about 100 Hz), and large displacement (in millimeters) actuators. A key challenge is to amplify the stroke of existing actuators by trading force with displacement. Large mechanical amplification using a compact leverage system often leads to substantial losses at hinges and slippage at knife edges. The goal should be to increase displacement capability of smart materials actuators by 300–500% and/or build efficient stroke-amplification devices. Even though there are new revolutionary smart materials such as single crystal piezoceramics and magnetic shape memory alloys are emerging, their commercial viability and applications are at an embryonic stage.

B. Database for Smart Materials Characteristics

For design development of smart structures, it is essential to have a reliable database of characteristics of smart materials. At this time such a database for a wide range of test conditions is not available. Thus, there is need to develop a reliable database of smart material characteristics through extensive testing of engineering specimens (standardized at macrolevel). For example, electromechanical-thermal fatigue characteristics that are key to product reliability are lacking and need focused effort.

C. Piezoelectric Strain Sensors

Piezoelectric sensors have enormous potential to measure signals with high noise levels; however, their calibration factors for a wide range of operating conditions and configurations are not available. Hence, it is important to establish sensitivity of these sensors for different sensor size, temperature, bond layer, and strain level.

D. Beam Modeling

Because the local strain distribution near a piezoactuator is two-dimensional, it is important to refine one-dimensional beam models that capture this effect. Simple models for beams with actuators not aligned with the beam axis are inadequate and should be improved. Because the bond layer plays an important role in the induced strain transfer from actuator to beam, higher-order shear deformation theory should be used to examine this effect and also to establish the limits of widely used simple beam theories. Beam analyses need to be refined to include nonlinear piezocharacteristics, piezoelectric-mechanical couplings, and layerwise shear variations. Validation studies should be expanded to cover coupled composite beams with surface-mounted or embedded actuators. Modeling of active composite plies that use AFC/MFC type fibers need carefully scrutiny and systematic validations.

E. Plate Modeling

There is a general lack of validation studies with experimental data or with detailed analyses. Most plate models assume a perfect bond condition that is too restrictive. There is a need to develop detailed three-dimensional finite element analyses or higher-order shear deformation formulations including nonlinear actuation strain and piezoelectric-mechanical couplings to check the limitations of existing laminated plate analyses (such as CLPT) as well as to understand the diffusion of actuation strain. Validation studies with experimental test data should be expanded to cover a range of composite coupled plate configurations including active fiber composite plies.

F. Shape Memory Alloys

Systematic validation of constitutive models of SMA for different temperatures and strains (extensional and shear) is not readily available. Building of composite structures with embedded SMAs is still a challenge and needs a focused effort. Analysis of structures with embedded SMA has so far shown mixed success in terms of correlation of predicted results with measured data. Refined analyses using higher-order shear deformation theory or detailed three-dimensional finite element analysis should be developed to investigate the actuation mechanism as well as the structural integrity of system. To exploit the potential of SMA to various applications, it is important to refine and simplify analyses and carry out systematic validations. Most current constitutive models are developed for uniaxial quasisteady loading and require reformulations and extensions to cover torsional and three-dimensional stress conditions for both steady and transient thermal and mechanical loadings. Innovations are needed to increase frequency response of SMA actuators. Exploitation of SMA to augment structural damping needs further examination.

G. Magnetostrictives and Electrostrictives

At this time most of the smart-structures studies are focused on piezoelectric and SMA actuators. Simplified constitutive relations for magnetostrictive and electrostrictive actuators are not readily available. To exploit these actuators for some special applications, it is important to develop simplified constitutive relations and validate them with experimental data. Detailed measured nonlinear electromechanical/magnetomechanical characteristics of electostrictives and magnetostrictives are not readily available and should obtained for a wide range of load conditions.

H. Application to Realistic Systems

Currently, this emerging technology is applied to models/simulations that are often unrealistic. For a proper assessment of this technology, it is necessary to apply it to realistic structures. Major barriers are actuator stroke, unavailability of robust distributed parameter control strategies, and nonexistent mathematical modeling of the smart system. The objective should be to build and test dynamically scaled models and evaluate performance of actuators and feedback control algorithms under different operating conditions. Using these test data, validate comprehensive analyses and then carry out multidisciplinary optimization studies to develop a smart actuation system.

I. Expand Smart-Structures Applications to Improve Performance and Minimize Acoustics

Currently, most applications of smart-structures technology to aeronautical systems such as wings and rotors are focused on vibration minimization. There is an enormous payoff to exploit this technology to improve system performance, primary controls implementation, and minimize external/internal noise. It is necessary to build dynamically scaled models and test them in different operating conditions. Key barriers are large bandwidth/large stroke actuators, reliable active noise control analyses, robust acoustic sensors, well-defined objectives, and unavailability of distributed parameters control algorithms. The objective should be to build and test dynamically scaled models and evaluate performance of smart actuators and feedback controllers under different flight conditions. Using these test data, validate comprehensive analyses and then carry out multidisciplinary optimization studies to develop a smart-structures system to simultaneously increase system performance and minimize noise and vibration. The challenge is to replace servoactuators with smart actuators for primary controls in a cost-effective manner and with no degradation in product reliability.

J. Smart-Structures Application to Increase Damping

There are systems that are inherently low damped and require some form of damping augmentation. For example, to overcome aeromechanical instability of helicopter rotors, they are installed with either complex mechanical dampers or expensive elastomeric dampers. To reduce the maintenance and procurement cost substantially, there is a potential application of smart-structures technology to augment rotor damping. Hybrid active/passive constrained layer damping in conjunction with electrorheological and magnetorheological fluid dampers as well as shape control devices (such as flaps) can be used to augment blade lag mode damping. Current barriers are reliable analytical models, test data to cover a wide range of operating conditions, and limited stroke of actuators. Road maps should be established to develop and validate different analytical elements of damping augmentation, as well as to apply these to dynamically scaled models and evaluate their performance under different operating conditions.

K. Structural Health Monitoring of Systems

Aerospace systems are highly susceptible to damage because of severe vibratory and fatigue loads. The problem is addressed by frequent inspection of damage-sensitive parts and, if required, replacement of such parts. This contributes to higher operating and maintenance costs. Health monitoring of aerospace systems offer the potential to lower operating costs and enhance flight reliability. At this time there have been only limited experimental studies on this topic, and analytical tools are primitive. Major barriers are unavailability of robust sensors, reliable system identification algorithms, proper analog/digital filters, and data multiplexing and wireless transmission. Keeping in view the future goal to reduce maintenance costs of aerospace systems by at least 25–50%, there is a need of focused fundamental research activities related to health monitoring of aerospace and other systems using smart sensors.

L. Revolutionary Smart Materials

Recently, there have been some exciting developments in smart materials such as the emergence of magnetic shape memory alloys, single crystal piezoceramics, and piezoelectric and electrostrictive polymeric actuator materials that have a stroke of an order of magnitude larger than current piezoceramics. These materials require careful scrutiny by researchers. There is every potential that these revolutionary materials might open up many new frontiers of applications and result in "quantum-jump" in system performance and reliability and dramatic reduction in acquisition and operating costs. That will be the dawn of smart materials.

Acknowledgments

Most of these research activities were supported by the U.S. Army Research Office under Grants URI: DAAL 03-92-G-0121 and MURI: DAAH-04-96-10334 with Gary Anderson and Tom Doligalski as Technical Monitors. The author acknowledges many useful discussions and enthusiastic input from Friedrich Straub, Boeing, Mesa, Arizona; Yung Yu, National Rotorcraft Technology Center; Alfred Gessow, Norman Wereley, Darryll Pines, and V. T. Nagaraj, University of Maryland; and many graduate students (Peter Chen, Andy Bernhard, Nikhil Koratkar, Jeanette Epps, Taeoh Lee, Jayant Sirohi, Harsha Prahlad, Mike Spencer, and Judah Milgram).

References

[1]Banks, H. T., Smith, R. C., and Wang, Y., *Smart Material Structures Modeling, Estimation and Control*, Wiley, New York, 1996.

[2]Cady, W. G., *Piezoelectricity*, Dover, New York, 1964.

[3]Clark, R. L., Saunders, W. R., and Gibbs, G. P., *Adaptive Structures Dynamics and Control*, Wiley, New York, 1998.

[4]Culshaw, B., *Smart Structures and Materials*, Artech House Optoelectronics Library, Boston, 1996.

[5]Dorey, A. P., and Moore, J. H., *Advances in Actuators*, Inst. of Physics Publishing, London, 1995.

[6]Duerig, T. W., Melton, K. N., Stokel, D., and Wayman, C. M., *Engineering Aspects of Shape Memory Alloys*, Butterworths, London, 1990.

[7]Duerig, T. W., and Zadno, G. R., "An Engineer's Perspective of Pseudoelasticity," *Engineering Aspects of Shape Memory Alloys*, Butterworths, London, 1990.

[8]Fremond, M., and Miyazaki, S., *Shape Memory Alloys*, Springer-Verlag, New York, 1996.

[9]Funakubo, H., *Shape Memory Alloys*, Gordon and Breach, New York, 1987.

[10]Gandhi, M. V., and Thompson, B. S., *Smart Materials and Structures*, Chapman and Hall, London, 1992.

[11]Hodgson, D. E., *Using Shape Memory Alloys*, Shape Memory Applications, Inc., Santa Clara, CA, 1988.

[12]Ikeda, T., *Fundamentals of Piezoelectricity*, Oxford Univ. Press, Oxford, 1990.

[13]Lines, M. E., and Glass, A. M., *Principles and Applications of Ferroelectrics and Related Materials*, Oxford Univ. Press, Oxford, 1977.

[14]Jaffe, B., Cook, W. R., and Jaffe, H., *Piezoelectric Ceramics*, Academic Press, New York, 1971.

[15]Mason, W. P., *Piezoelectric Crystals and their Applications to Ultrasonics*, Plenum, New York, 1950.

[16]Perkins, J., *Shape Memory Effects in Alloys*, Plenum, New York, 1976.

[17]Premont, A., *Vibration Control of Active Structures: An Introduction*, Kluwer Academic, Norwell, MA, 1997.

[18]Shields, J. P., *Basic Piezoelectricity*, Foulsham-Sams, Bucks, England, U.K., 1996.

[19]Srinivasan, A. V., and McFarland, D. M., *Smart Structures Analysis and Design*, Cambridge Univ. Press, Cambridge, England, U.K., 2000.

[20]Tiersten, H. F., *Linear Piezoelectric Plate Vibrations*, Plenum, New York, 1950.

[21]Tzou, H. S., and Anderson, G. L. (eds.), *Intelligent Structural Systems*, Kluwer Academic, Norwell, MA, 1992.

[22]Tzou, H. S., *Piezoelectric Shells Distributed Sensing and Control Continua*, Kluwer Academic, Norwell, MA, 1993.

[23]Uchino, K., *Piezoelectric Devices and Ultrasonic Motors*, Kluwer Academic, Norwell, MA, 1997.

[24]Ueha, S., Tomikawa, Y., Kurosawa, M., and Nakamura, N., *Ultrasonic Motors Theory and Applications*, Clarendon, Oxford, 1993.

[25]Wayman, C. M., and Duerig, T. W., "An Introduction to Martensite and Shape Memory," *Engineering Aspects of Shape Memory Alloys*, Butterworths, London, 1990.

[26]Benjeddou, A., "Advances in Piezoelectric Finite Element Modeling of Adaptive Structural Elements: A Survey," *Computers and Structures*, Vol. 76, No. 4, 2000, pp. 347–363.

[27]Birman, V., "Review of Mechanics of Shape Memory Alloy Structures," *Applied Mechanics Reviews*, Vol. 50, No. 11, 1997, pp. 629–645.

[28]Chee, C. Y. K., Tong, L., and Steven, G. P., "A Review on the Modeling of Piezoelectric Sensors and Actuators Incorporated in Intelligent Structures," *Journal of Intelligent Material Systems and Structures*, Vol. 9, No. 1, 1998, pp. 3–19.

[29]Chopra, I., "State-of-the-Art of Smart Structues and Integrated Systems," *Proceedings of the Society of Photo-Optical Instrumentation Engineers 3th Annual Symposium on Smart Structures and Materials*, Vol. 2717, Society of Photo-Optical Instrumentation Engineers (International Society for Optical Engineering), Bellingham, WA, 1996.

[30]Chopra, I., "Status of Application of Smart Structures Technology to Rotorcraft Systems," *Journal of the American Helicopter Society*, Vol. 45, No. 4, 2000, pp. 228–252.

[31]Crawley, E., "Intelligent Structures for Aerospace: A Technology Overview and Assessment," *AIAA Journal*, Vol. 32, No. 8, 1994, pp. 1689–1699.

[32]Cross, L. E., "Ferroelectric Ceramics: Materials and Application Issues," *Ceramic Transanctions*, Vol. 68, No. 1, 1996, pp. 15–30.

[33]Domeci, M. C., "Recent Progress in the Dynamic Applications of Piezoelectric Crystals," *Shock and Vibration Digest*, Vol. 20, No. 2, 1988, pp. 3–20.

[34]Garg, D. P., Zikry, M. A., and Anderson, G. L., "Current and Potential Future Research Activities in Adaptive Structures: An ARO Perspective," *Smart Materials and Structures*, Vol. 10, No. 4, 2001, pp. 610–623.

[35]Giurgiutu, V., "Review of Smart-Materials Actuation Solutions for Aeroelastic and Vibration Control," *Journal of Intelligent Material Systems and Structures*, Vol. 11, No. 7, 2000, pp. 525–544.

[36]Loewy, R. G., "Recent Developments in Smart Structures with Aeronautical Applications," *Proceedings of 37th Israel Annual Conference in Aerospace Sciences*, Technion–Israel Inst. of Technology, Haifa, Israel, 1997.

[37]Niezrecki, C., Brei, D., Balakrishnan, S., and Moskalik, A., "Piezoelectric Actuation: State of the Art," *Shock and Vibration Digest*, Vol. 33, No. 4, 2001, pp. 269–280.

[38]Sunar, M., and Rao, S. S., "Recent Advances in Sensing and Control of Flexible Structures via Piezoelectric Materials Technology," *Applied Mechanics Reviews*, Vol. 52, No. 1, 1999, pp. 1–16.

[39]Strehlow, H., and Rapp, H., "Smart Materials for Helicopter Rotor Active Control," AGARD/SMP Specialist's Meeting on Smart Structures for Aircraft and Spacecraft, Oct. 1992.

[40]Takagi, T., "Present State and Future of the Intelligent Materials and Systems in Japan," *Journal of Intelligent Material Systems and Structures*, Vol. 10, No. 7, 1999, pp. 575–581.

[41]Wada, B. K., "Adaptive Structures—An Overview," *Journal of Spacecraft and Rockets*, Vol. 27, No. 3, 1990, pp. 330–337.

[42]Giurgiutiu, V., Rogers, C. A., and Chaudhary, Z., "Energy-Based Comparison of Solid-State Induced-Strain Actuators," *Journal of Intelligent Material Systems and Structures*, Vol. 7, No. 1, 1996, pp. 4–14.

[43]Near, C. D., "Piezoelectric Actuator Technology," *Proceedings of the Society of Photo-Optical Instrumentation Engineer's 3rd Annual Symposium on Smart Structures and Materials*, Vol. 2717, Society of Photo-Optical Instrumentation Engineers (International Society for Optical Engineering), Bellingham, WA, 1996, pp. 246–258.

[44]Li, S., Cao, W., and Cross, L. E., "The Extrinsic Nature of Nonlinear Behavior Observed in Lead Zirconate Titanate Ferroelectric Ceramic," *Journal of Applied Physics*, Vol. 69, No. 10, 1991, pp. 7219–7224.

[45]"Inst. of Electrical and Electronics Engineers Standard on Piezoelectricity," Std. 176, ANSI/IEEE, 1987.

[46]*Morgon Matroc Inc. Piezoceramic Databook*, Morgan Matroc Electroceramic Div., Bedford, OH, 1993.

[47]Kreuger, H. H. A., "Effect of High Static Stress on the Piezoelectric Properties of Transducer Materials," *Journal of the Acoustical Society of America*, Vol. 43, No. 3, 1967, pp. 636–645.

[48]Sirohi, J., and Chopra, I., "Fundamental Behavior of Piezoceramic Sheet Actuators," *Journal of Intelligent Material Systems and Structures*, Vol. 11, No. 1, 2000, pp. 47–61.

[49]Ghandi, K., and Hagood, N. W., "Nonlinear Modeling and Characterization Techniques for Phase Transitions in Electro-Mechanically Coupled Devices," Dept. of Aeronautics and Astronautics, AMSL 98-1, Massachusetts Inst. of Technology, Cambridge, MA, May 1998.

[50]Lynch, C. S., "On the Development of Multiaxial Phenomenological Constitutive Laws for Ferroelectric Ceramics," *Journal of Intelligent Material Systems and Structures*, Vol. 9, No. 7, 1998, pp. 555–563.

[51]Durr, J. K., Herold-Schmidt, U., Zaglauer, H. W., and Arendts, F. J., "On the Integration of Piezoceramic Actuators in Composite Structures for Aerospace Applications," *Journal of Intelligent Material Systems and Structures*, Vol. 10, No. 11, 1999, pp. 880–889.

[52]Warkentin, D. J., and Crawley, E. F., "Embedded Electronics for Intelligent Structures," *Proceedings of the 32th AIAA/ASME/ASCE/AHS/ASC Structures, Structural Dynamics, and Materials Conference*, AIAA, Washington, DC, 1991.

[53]Hagood, N. W., Kindel, R., Ghandi, K., and Gaudenzi, P., "Improving Transverse Actuation of Piezoceramics Using Interdigitated Surface Electrodes," *Proceedings of the Society of Photo-Optical Instrumentation Engineers' Symposium on Smart Structures and Intelligent Systems*, Vol. 1917, Society of Photo-Optical Instrumentation Engineers (International Society for Optical Engineering), Bellingham, WA, 1993.

[54]Bent, A. A., and Hagood, N. W., "Piezoelectric Fiber Composites with Interdigitated Electrodes," *Journal of Intelligent Material Systems and Structures*, Vol. 8, No. 11, 1997, pp. 903–919.

[55]Yoshikawa, S., Farrell, M., Warkentin, D., Jacques, R., and Saarmaa, E., "Monolithic Piezoelectric Actuators and Vibration Dampers with Interdigitated Electrodes," *Proceedings of the Society of Photo-Optical Instrumentation Engineers' 6th Annual Symposium on Smart Structures and Materials*, Vol. 3668, Society of Photo-Optical Instrumentation Engineers (International Society for Optical Engineering), Bellingham, WA, 1999, pp. 575–585.

[56]Wilkie, K. W., Bryant, R. G., High, J. W., Fox, R. L., Hellbaum, R. F., Jalink, A., and Mirick, P. H., "Low-Cost Piezocomposite Actuator Structural Control Applications," *Proceedings of the Society of Photo-Optical Instrumentation Engineers' 7th Annual Symposium on Smart Structures and Materials*, Vol. 3668, Society of Photo-Optical Instrumentation Engineers (International Society for Optical Engineering), Bellingham, WA, 1999.

[57]Ha, S. K., Keilers, C., and Chang, F. K., "Finite Element Analysis of Composite Structures Containing Distributed Piezoceramic Sensors and Actuators," *AIAA Journal*, Vol. 30, No. 3, 1992, pp. 772–780.

[58]Hagood, N. W., and Anderson, E. H., "Simultaneous Sensing and Actuation Using Piezoelectric Materials," Society of Photo-Optical Instrumentation Engineers, SPIE 1543, July 1991.

[59]Ghiringhelli, G. L., Masarati, P., and Mantegazza, P., "Characterization of Anisotropic, Non-Homogeneous Beam Sections with Embedded Piezo-Electric Materials," *Journal of Intelligent Material Systems and Structures*, Vol. 8, No. 10, 1997, pp. 842–858.

[60]Mukherjee, B. K., Ren, W., Liu, S. F., Masys, A. J., and Yang, G., "Non-Linear Properties of Piezoelectric Ceramics," *Proceedings of the 2001 Society of Photo-Optical Instrumentation Engineers' North American Symposium on Smart Structures and Materials*, Society of Photo-Optical Instrumentation Engineers (International Society for Optical Engineering), Bellingham, WA, 2001.

[61]Yang, G., Liu, S. F., Ren, W., and Mukherjee, B. K., "Effects of Uniaxial Stress on the Piezoelectric, Dielectric, and Mechanical Properties of Lead Zirconate Titanate Piezoceramics," *Ferroelectrics*, Vol. 262, No. 1–4, 2001, pp. 207–212.

[62]Ren, W., Masys, A. J., Yang, G., and Mukherjee, B. K., "The Field and Frequency Dependence of the Strain and Polarisation in Piezoelectric and Electrostrictive Ceramics," *Ferroelectrics*, Vol. 261, No. 1–4, 2001, pp. 27–32.

[63]Gerson, R., Burlage, S. R., and Berlincourt, D., "Dynamic Tensile Stress of a Ferroelectric Ceramic," *Journal of the Acoustical Society of America*, Vol. 42, No. 3, 1967, pp. 583–591.

[64]Brown, R. F., "Effect of Two-Dimensional Mechanical Stress on the Dielectric Properties of Poles Ceramic Barium Titanate an d Lead Zirconate Titanate," *Canadian Journal of Physics*, Vol. 39, No. 5, 1961, pp. 741–753.

[65]Freiman, S. W., and White, G. S., "Intelligent Ceramic Materials: Issues of Brittle Fracture," *Journal of Intelligent Material Systems and Structures*, Vol. 6, No. 1, 1995, pp. 49–54.

[66]Wang, D., and Carman, G. P., "Combined Electrical and Mechanical Fatigue of Piezoelectric Ceramics Undergoing Polarization Switching for Large Displacement Actuation," *Proceedings of the Society of Photo-Optical Instrumentation Engineers' 5th Annual Symposium on Smart Structures and Materials*, Society of Photo-Optical Instrumentation Engineers (International Society for Optical Engineering), Bellingham, WA, 1998, pp. 210–223.

[67]Glazounov, A. E., Zhang, Q. M., and Kim, C., "Torsional Actuator and Stepper Motor Based on Piezoelectric d_{15} Shear Response," *Journal of Intelligent Material Systems and Structures*, Vol. 11, No. 6, 2000, pp. 456–468.

[68]Kim, J., and Kang, B., "Performance Test and Improvement of Piezoelectric Torsional Actuators," *Smart Materials and Structures*, Vol. 10, No. 4, 2001, pp. 750–757.

[69]Bailey, A., and Hubbard, J. E., "Distributed Piezoelectric-Polymer Active Vibration Control of a Cantilevered Beam," *Journal of Guidance, Control, and Dynamics*, Vol. 8, No. 5, 1985, pp. 605–611.

[70]Hanagud, S., Obal, M. W., and Calise, A. J., "Optimal Vibration Control by the Use of Piezoelectric Sensors and Actuators," *Journal of Guidance, Control, and Dynamics*, Vol. 15, No. 5, 1992, pp. 1199–1206.

[71]Dosch, J. J., Inman, D. J., and Garcia, E., "A Self-Sensing Actuator for Collocated Control," *Journal of Intelligent Material Systems and Structures*, Vol. 3, No. 1, 1992, pp. 166–185.

[72]Inman, D. J., Dosch, J. J., and Garcia, E., "A Self-Sensing Piezoelectric Actuator for Collocated Controls," *Journal of Intelligent Material Systems and Structures*, Vol. 3, No. 1, 1992, pp. 166–185.

[73]Anderson, E. H., and Hagood, N. W., "Simultaneous Piezoelectric Sensing/Actuation: Analysis and Application to Controlled Structures," *Journal of Sound and Vibration*, Vol. 174, No. 5, 1994, pp. 617–639.

[74]Qui, J., and Tani, J., "Vibration Control of a Cylindrical Shell Using Distributed Piezoelectric Sensors and Actuators," *Journal of Intelligent Material Systems and Structures*, Vol. 6, No. 4, 1995, pp. 474–481.

[75]Lee, C. K., and O'Sullivan, T., "Piezoelectric Strain Rate Gages," *Journal of the Acoustical Society of America*, Vol. 90, No. 2, 1991, pp. 945–953.

[76]Samuel, P., and Pines, D., "Health Monitoring/Damage Detection of a Rotorcraft Planetary Geartrain Using Piezoelectric Sensors," *Proceedings of the Society of Photo-Optical Instrumentation Engineers' 4th Annual Symposium on Smart Structures and Materials*, Vol. 3041, Society of Photo-Optical Instrumentation Engineers (International Society for Optical Engineering), Bellingham, WA, 1997, pp. 44–53.

[77]Giurgiutiu, V., and Zagrai, A. N., "Characterization of Piezoelectric Wafer Active Sensors," *Journal of Intelligent Material Systems and Structures*, Vol. 11, No. 12, 2000, pp. 959–976.

[78]Sirohi, J., and Chopra, I., "Fundamental Understanding of Piezoelectric Sensors," *Journal of Intelligent Material Systems and Structures*, Vol. 11, No. 4, 2000, pp. 246–257.

[79]Pines, D. J., and Von Flotow, A. H., "Specially Convolving Wave Propagation Sensors for Structural Control-Part.I: Analytical Development of One-Dimensional Structures," *Journal of Intelligent Material Systems and Structures*, Vol. 8, No. 11, 1997, pp. 929–952.

[80]Pines, D. J., and Von Flotow, A. H., "Specially Convolving Wave Propagation Sensors for Structural Control-Part.II: Experimental Verification Using PVDF Sensors," *Journal of Intelligent Material Systems and Structures*, Vol. 8, No. 12, 1997, pp. 1059–1072.

[81]Crawley, E., and de Luis, J., "Use of Piezoceramic Actuators as Elements of Intelligent Structures," *AIAA Journal*, Vol. 25, No. 10, 1987, pp. 1373–1385.

[82]Crawley, E., and Anderson, E., "Detailed Models of Piezoceramic Actuation of Beams," *Journal of Intelligent Material Systems and Structures*, Vol. 1, No. 1, 1990, pp. 4–25.

[83]Park, C., Walz, C., and Chopra, I., "Bending and Torsion Models of Beams with Induced-Strain Actuators," *Smart Material and Structures*, Vol. 5, No. 1, 1996, pp. 98–113.

[84]Park, C., and Chopra, I., "Modeling Piezoceramic Actuation of Beams in Torsion," *AIAA Journal*, Vol. 34, No. 12, 1996, pp. 2582–2589.

[85]Banks, H. T., and Zhang, Y., "Computational Methods for Curved Beam with Piezoelectric Patched," *Journal of Intelligent Material Systems and Structures*, Vol. 8, No. 3, 1997, pp. 260–278.

[86]Ghiringhelli, G. L., Masarati, P., and Mantegazza, P., "Characterization of Anisotropic Non-Homogeneous Beam Sections with Embedded Piezoelectric Materials," *Journal of Intelligent Material Systems and Structures*, Vol. 8, No. 10, 1997, pp. 842–858.

[87]Trindade, M. A., Bengeddou, A., and Ohayon, "Parametric Analysis of the Vibration Control of Sandwich Beams Through Shear-Based Piezoelectric Actuation," *Journal of Intelligent Material Systems and Structures*, Vol. 10, No. 5, 1999, pp. 377–385.

[88]Benjeddou, A., Trindade, M. A., and Ohayon, R., "A Unified Beam Finite Element Model for Extension and Shear Piezoelectric Actuation Mechanisms," *Journal of Intelligent Material Systems and Structures*, Vol. 8, No. 12, 1997, pp. 1012–1025.

[89]Benjeddou, A., Trindade, M. A., and Ohayon, R., "New Shear Actuated Smart Structures Beam Finite Element," *AIAA Journal*, Vol. 37, No. 3, 1999, pp. 378–402.

[90]Zhang, X. D., and Sun, C. T., "Formulation of an Adaptive Sandwich Beam," *Smart Materials and Structures*, Vol. 5, No. 6, 1996, pp. 814–823.

[91]Cai, D., and Gao, Y., "Shear Control and Analytical Solutions for 2-D Smart Beam Theory," *Journal of Intelligent Material Systems and Structures*, Vol. 9, No. 3, 1998, pp. 182–188.

[92]Chen, P. C., and Chopra, I., "Hover Testing of Smart Rotor with Induced-Strain Actuation of Blade Twist," *AIAA Journal*, Vol. 35, No. 1, 1997, pp. 6–16.

[93]Im, S., and Atluri, S. N., "Effects of Piezo Actuator on a Finitely Deformed Beam Subjected to General Loading," *AIAA Journal*, Vol. 27, No. 12, 1989, pp. 1801–1807.

[94]Hagood, N. W., Chung, W. H., and Flotow, A. V., "Modeling of Piezoelectric Actuator Dynamics for Active Structural Control," *Journal of Intelligent Material Systems and Structures*, Vol. 1, No. 3, 1990, pp. 327–354.

[95]Jung, S. N., Nagaraj, V. T., and Chopra, I., "Assessment of Composite Rotor Blade Modeling Techniques," *Journal of the American Helicopter Society*, Vol. 44, No. 3, 1999, pp. 188–205.

[96]Jung, S. N., Nagaraj, V. T., and Chopra, I., "Refined Structural Model for Thin- and Thick-Walled Composite Rotor Blades," *AIAA Journal*, Vol. 40, No. 1, 2002, pp. 105–116.

[97]Bauchau, O. A., and Hong, C. H., "Nonlinear Composite Beam Theory," *Journal of Applied Mechanics*, Vol. 55, No. 2, 1988, pp. 156–163.

[98]Cesnik, C. E. S., and Hodges, D. S., "VABS: A New Concept for Composite Rotor Blade Cross-Sectional Modeling," *Journal of the American Helicopter Society*, Vol. 42, No. 1, 1997, pp. 27–38.

[99]Smith, E. C., and Chopra, I., "Formulation and Evaluation of an Analytical Model for Composite Box-Beams," *Journal of the American Helicopter Society*, Vol. 36, No. 3, 1991, pp. 23–35.

[100]Stemple, A. D., and Lee, S. W., "Finite Element Model for Composite Beams of Arbitrary Cross-Sectional Warping," *AIAA Journal*, Vol. 26, No. 12, 1988, pp. 1512–1520.

[101]Librescu, L., Meirovitch, L., and Song, O., "Integrated Structural Tailoring and Adaptive Materials Control for Advanced Aircraft Wings," *Journal of Aircraft*, Vol. 33, No. 1, 1996, pp. 203–213.

[102]Chandra, R., and Chopra, I., "Structural Modeling of Composite Beams with Induced Strain Actuation," *AIAA Journal*, Vol. 31, No. 9, 1993, pp. 1692–1701.

[103]Kaiser, C., "Piezothermoelastic Behavior of Thin-Walled Composite Beams with Elastic Couplings," *Proceedings of AIAA/ASME/ASCE/AHS/ASC 42nd Structures, Structural Dynamics, and Materials Conference*, AIAA, Reston, VA, 2001.

[104]Cesnik, C. E. S., and Shin, S. J., "On the Modeling of Integrally Actuated Helicopter Blades," *International Journal of Solids and Structures*, Vol. 38, No. 10, 2001, pp. 1765–1789.

[105]Shin, S. J., and Cesnik, C. E. S., "Integral Twist Actuation of Helicopter Rotor Blades for Vibration Reduction," Dept. of Aeronautics and Astronautics, AMSL 01-07, Massachusetts Inst. of Technology, Cambridge, MA, Aug. 2001.

[106]Bernhard, A. P. F., and Chopra, I., "Analysis of Bending-Torsion Coupled Actuator for a Smart Rotor with Active Blade Tips," *Smart Material and Structures*, Vol. 10, No. 1, 2001, pp. 35–52.

[107]Raja, S., Rohwer, K., and Rose, M., "Piezothermoelastic Modeling and Active Vibration Control of Laminated Composite Beams," *Journal of Intelligent Material Systems and Structures*, Vol. 10, No. 11, 1999, pp. 890–899.

[108]Shen, M. H., "A New Modeling Technique for the Piezoelectric Actuated Beams," *Computers and Structures*, Vol. 57, No. 3, 1995, pp. 361–366.

[109]Reddy, J. N., "A Generalization of Two-Dimensional Theories of Laminated Composite Plates," *Communications in Applied Numerical Methods*, Vol. 173, No. 3, 1987, pp. 173–180.

[110]Robbins, D. H., and Reddy, J. N., "Analysis of Piezoelectrically Actuated Beams Using a Layer-Wise Displacement Theory," *Computer and Structures*, Vol. 41, No. 2, 1991, pp. 265–279.

[111]Saravanos, D. A., and Heyliger, P. R., "Coupled Layerwise Analysis of Composite Beams with Embedded Piezoelectric Sensors and Actuators," *Journal of Intelligent Material Systems and Structures*, Vol. 6, No. 3, 1995, pp. 350–363.

[112]Crawley, E. F., and Lazarus, K. B., "Induced Strain Actuation of Isotropic and Anisotropic Plates," *AIAA Journal*, Vol. 23, No. 6, 1991, pp. 944–951.

[113]Hong, C. H., and Chopra, I., "Modeling and Validation of Induced Strain Actuation of Composite Coupled Plates," *AIAA Journal*, Vol. 37, No. 3, 1999, pp. 372–377.

[114]Lee, C. K., "Theory of Laminated Piezoelectric Plates for the Design of Distributed Sensors/Actuators: Part I: Governing Equations and Reciprocal Relationships," *Journal of Acoustical Society of America*, Vol. 87, No. 3, 1990, pp. 1144–1158.

[115]Lee, C. K., "Piezoelectric Laminates: Theory and Experiment for Distributed Sensors and Actuators," *Intelligent Structural Systems*, edited by H. S. Tzou and G. L. Anderson, Kluwer Academic, Norwell, MA, 1992, pp. 75–168.

[116]Wang, B. T., and Rogers, C. A., "Laminate Plate Theory for Spatially Distributed Induced Strain Actuators," *Journal of Composite Materials*, Vol. 25, No. 4, 1991, pp. 433–452.

[117]Heyliger, P., "Exact Soluations for Simply Supported Laminated Piezoelectric Plates," *Journal of Applied Mechanics*, Vol. 64, No. 2, 1997, pp. 299–306.

[118]Gopinathan, S. V., Varadan, V. V., and Varadan, V. K., "A Review and Critique of Theories for Piezoelectric Laminates," *Smart Materials and Structures*, Vol. 9, No. 1, 2000, pp. 24–48.

[119]Wang, J., and Yang, J., "Higher-Order Theories of Piezoelectric Plates and Applications," *Applied Mechanics Reviews*, Vol. 53, No. 1, 2000, pp. 87–99.

[120]Rahmoune, M., Benjeddou, A., Ohayon, R., and Osmont, D., "New Thin Piezoelectric Plate Models," *Journal of Intelligent Material Systems and Structures*, Vol. 9, No. 12, 1998, pp. 1017–1029.

[121]Yu, Y. Y., "Some Recent Advances in Linear and Nonlinear Dynamical Modeling of Elastic and Piezoelectric Plates," *Journal of Intelligent Meterial Systems and Structures*, Vol. 6, No. 2, 1995, pp. 237–254.

[122]Bisegna, P., and Maceri, F., "A Consistent Theory of Thin Piezoelectric Plates," *Journal of Intelligent Material Systems and Structures*, Vol. 7, No. 4, 1996, pp. 372–389.

[123]Bisegna, P., and Carusa, G., "Mindlin-Type Finite Elements for Piezoelectric Sandwich Plates," *Journal of Intelligent Material Systems and Structures*, Vol. 11, No. 1, 2000, pp. 14–25.

[124]Carrera, E., "An Improved Reissner-Mindlin Type Model for the Electromechanical Analysis of Multilayered Plates Including Piezo-Layers," *Journal of Intelligent Material Systems and Structures*, Vol. 8, No. 3, 1997, pp. 232–248.

[125]Reddy, J. N., "A Simple Higher-Order Theory for Laminated Composite Plates," *Journal of Applied Mechanics*, Vol. 51, No. 4, 1984, pp. 745–752.

[126]Nosier, A., Kapania, R. K., and Reddy, J. N., "Free Vibration Analysis of Laminated Plates Using a Layerwise Theory," *AIAA Journal*, Vol. 31, No. 12, 1993, pp. 2335–2346.

[127]Reddy, J. N., "A Generalization of Two-Dimensional Theories of Laminated Composite Plates," *Communications in Applied Numerical Methods*, Vol. 3, No. 3, 1987, pp. 173–180.

[128]Sun, C. T., and Whitney, J. M., "Theories for the Dynamic Response of Laminated Plates," *AIAA Journal*, Vol. 11, No. 2, 1973, pp. 178–183.

[129]Mitchell, J. A., and Reddy, J. N., "A Refined Hybrid Plate Theory for Composite Laminates of Piezoelectric Laminae," *International Journal of Solids and Structures*, Vol. 32, No. 16, 1995, pp. 2345–2367.

[130]Robbins, D. H., and Reddy, J. N., "An Efficient Computational Model for the Stress Analysis of Smart Plate Structures," *Smart Materials and Structures*, Vol. 5, No. 3, 1996, pp. 353–360.

[131]Chattopadhyay, A., Li, J., and Gu, H., "Coupled Thermo-Piezoelectric-Mechanical Model for Smart Composite Laminate," *AIAA Journal*, Vol. 37, No. 12, 1999, pp. 1633–1638.

[132]Zhou, X., Chattopadhyay, A., and Gu, H., "Dynamic Response of Smart Composites Using a Coupled Thermo-Piezoelectric-Mechanical Model," *AIAA Journal*, Vol. 38, No. 10, 2000, pp. 1939–1948.

[133]Vel, S. S., and Batra, R. C., "Three-Dimensional Analytical Solution for Hybrid Multilayered Piezoelectric Plates," *Journal of Applied Mechanics*, Vol. 67, No. 3, 2000, pp. 558–567.

[134]Yang, J. S., and Batra, R. C., "Mixed Variational Principles in Nonlinear Piezoelectricity," *International Journal of Nonlinear Mechanics*, Vol. 30, No. 5, 1995, pp. 719–726.

[135]Batra, R. C., and Vidoli, S., "Higher-Order Piezoelectric Plate Theory Derived from a Three-Dimensional Variational Principle," *AIAA Journal*, Vol. 40, No. 1, 2002, pp. 91–104.

[136]Ha, S. K., Kellers, C., and Chang, F. K., "Finite Element Analysis of Composite Structures Containing Piezoceramic Sensors and Actuators," *AIAA Journal*, Vol. 32, No. 3, 1992, pp. 772–780.

[137]Buehler, W. J., Wiley, R. C., and Wang, F. E., "Nickel-Based Alloys," U.S. Patent 3,174,851,23, March 1965.

[138]Tanaka, K., "A Thermomechanical Sketch of Shape Memory Effect: One-Dimensional Tensile Behavior," *Res. Mechanica*, Vol. 18, No. 3, 1986, pp. 251–263.

[139]Liang, C., and Rogers, C. A. , "One-Dimensional Thermomechanical Constitutive Relations for Shape Memory Material," *Journal of Intelligent Material Systems and Structures*, Vol. 1, No. 2, 1990, pp. 207–234.

[140]Brinson, L. C., "One-Dimensional Constitutive Behavior of Shape Memory Alloy Constitutive Models," *Journal of Intelligent Material Systems and Structures*, Vol. 1, No. 2, 1990, pp. 207–234.

[141]Boyd, J. G., and Lagoudas, D. C., "A Thermodynamic Constitutive Model for the Shape Memory Materials Part I. The Monolithic Shape Memory Alloys," *International Journal of Plasticity*, Vol. 12, No. 6, 1996, pp. 805–842.

[142]Boyd, J. G., and Lagoudas, D. C., "A Thermodynamic Constitutive Model for the Shape Memory Materials Part II. The SMA Composite Material," *International Journal of Plasticity*, Vol. 12, No. 7, 1996, pp. 843–873.

[143]Ivshin, Y., and Pence, T. J., "A Thermo Mechanical Model for One Variant Shape Memory Material," *Journal of Intelligent Material Systems and Structures*, Vol. 5, No. 4, 1994, pp. 455–473.

[144]Graesser, E. J., and Cozzarelli, F. A., "A Proposed Three-Dimensional Model Constitutive Model for Shape Memory Material," *Journal of Intelligent Material Systems and Structures*, Vol. 5, No. 1, 1994, pp. 78–89.

[145]Sun, Q. P., and Hwang, K. C., "Micromechanics Modeling for the Constitutive Behavior of Polycrystalline Shape Memory Alloys-1. Derivation of General Relations," *Journal of Mechanical Physics Solids*, Vol. 41, No. 1, 1993, pp. 1–17.

[146]Matsuzaki, Y., Naito, H., Ikeda, T., and Funami, K., "Thermo-Mechanical Behavior Associated with Pseudoelastic Transformation of Shape Memory Alloys," *Smart Materials and Structures*, Vol. 10, No. 5, 2001, pp. 884–892.

[147]Barrett, D. J., "A One-Dimensional Constitutive Model for Shape Memory Alloys," *Journal of Intelligent Material Systems and Structures*, Vol. 6, No. 3, 1995, pp. 329–337.

[148]Brinson, L. C., and Huang, M., "Simplification and Comparisons of Shape Memory Alloy Constitutive Models," *Journal of Intelligent Material Systems and Structures*, Vol. 7, No. 1, 1996, pp. 108–114.

[149]Tobushi, H., Lin, P. H., Tanaka, K., Lexcellent, C., and Ikai, A., "Deformation Properties of TiNi Shape Memory Alloy," *Journal of Physique IV*, Vol. 5, C2, 1995, pp. 409, 410.

[150]Lin, P., Tobushi, H., Ikai, A., and Tanake, K., "Deformation Properties Associated with the Martensitic and R-Phase Transformations in TiNi Shape Memory Alloy," *Journal of Applied Biomechanics*, Vol. 10, No. 2, 1995, pp. 1–11.

[151]Tanaka, K., Nishimura, F., Matsui, H., Tobushi, H., and Lin, P. H., "Phenomenological Analysis of Plateaus on Stress-Strain Hysteresis in TiNi Shape Memory Alloy Wires," *Mechanics of Materials, An International Journal*, Vol. 24, No. 1, 1996, pp. 19–30.

[152]Tobushi, H., Yamada, S., Hachisuka, T., Ikai, A., and Tanaka, K., "Thermomechanical Properties due Martensitic and R-Phase Transformations of TiNi Shape Memory Alloy Subjected to Cyclic Loadings," *Smart Materials and Structures*, Vol. 5, No. 6, 1996, pp. 788–795.

[153]Sittner, P., Stalmans, R., and Tokuda, M., "An Algorithm for Prediction of the Hysteresis Responses of Shape Memory Alloys," *Smart Materials and Structures*, Vol. 9, No. 4, 2000, pp. 452–465.

[154]Naito, H., Matsuzaki, Y., and Ikeda, T., "A Unified Model of Thermomechanical Behavior of Shape Memory Alloys," Society of Photo-Optical Instrumentation Engineers, Vol. 4333, Society of Photo-Optical Instrumentation Engineers (International Society for Optical Engineering), Bellingham, WA, 2001, pp. 291–313.

[155]Prahlad, H., and Chopra, I., "Experimental Characterization of Ni-Ti Shape Memory Alloy Wires Under Uniaxial Loading Conditions," *Journal of Intelligent Material Systems and Structures*, Vol. 11, No. 4, 2000, pp. 272–282.

[156]Epps, J., and Chopra, I., "Comparative Evaluation of Shape Memory Alloy Constitutive Models with Experimental Test Data," *Proceedings of AIAA/ASME/ASCE/AHS/ASC 38th Structures, Structural Dynamics, and Materials Conference and Adaptive Structures Forum*, AIAA, Reston, VA, 1997.

[157]Bo, Z., and Lagoudas, D. C., "Comparison of Different Thermo Mechanical Models for Shape Memory Alloys," *Adaptive Structures and Composite Materials: Analysis and Applications: American Society of Mechanical Engineers Symposium*, Vol. 54, 1994, pp. 9–19.

[158]Prahlad, H., and Chopra, I., "Comparative Evaluation of Shape Memory Alloy Constitutive Models with Experimental Data," *Journal of Intelligent Material Systems and Structures*, Vol. 12, No. 6, 2001, pp. 386–396.

[159]Faulkner, M. G., Amairaj, J. J., and Battaacharyya, A., "Experimental Determination of Thermal and Electrical Propeties of Ni-Ti Shape Memory Wires," *Smart Materials and Structures*, Vol. 9, No. 5, 2000, pp. 632–639.

[160]Mikuriya, S., Nakahara, T., Tobushi, H., and Watanabe, H., "The Estimation of Temperature Rise in Low-Cycle Fatigue of TiNi Shape-Memory Alloy," *JSME International Journal*, Series A, Vol. 43, No. 2, 2000, pp. 166–172.

[161]Tobushi, H., Nakahara, T., Shimeno, Y., and Hashimoto, T., "Low-Cycle Fatigue of TiNi Shape Memory Alloy and Formulation of Fatigue Life," *Journal of Engineering Materials and Technology*, Vol. 122, No. 2, 2000, pp. 186–191.

[162]Prahlad, H., and Chopra, I., "Development of a Strain-Rate Dependant Model for Uniaxial Loading of SMA Wires," *12th International Conference on Adaptive Structures and Technologies*, CRC Press, Boca Raton, FL, 2001.

[163]Shaw, J. A., "Thermo-Mechanical Model for 1-D Shape Memory Alloys Wire with Propagating Instabilities," *International Journal of Solids and Structures*, Vol. 139, No. 5, 2002, pp. 1275–1305.

[164]Lexcellent, C., and Rejzner, J., "Modeling of the Strain Rate Effect, Creep and Relaxation of a Ni-Ti Shape Memory Alloy Under Tension (Compression)-Torsional Proportional Loading in the Pseudoelastic Range," *Smart Materials and Structures*, Vol. 9, No. 5, 2000, pp. 613–621.

[165]Potapov, P. L., and Silva, P. D., "Time Response of Shape Memory Alloy Actuators," *Journal of Intelligent Material Systems and Structures*, Vol. 11, No. 2, 2000, pp. 125–134.

[166]Davidson, F. M., Liang, C., and Lobitz, D., "Investigation of Torsional Shape Memory Alloy Actuators," *Proceedings of the Society of Photo-Optical Instrumentation Engineers' Symposium on Smart Structures and Materials, Smart Structures and Integrated Systems*, Vol. 2717, Society of Photo-Optical Instrumentation Engineers (International Society for Optical Engineering), Bellingham, WA, 1996, pp. 672–682.

[167]Keefe, A. C., and Carman, G. P., "Thermo-Mechanical Characterization of Shape Memory Alloy Torque Tube Actuators," *Smart Materials and Structures*, Vol. 9, No. 5, 2000, pp. 665–672.

[168]Prahlad, H., and Chopra, I., "Characterization of SMA Torsional Actuators for Variable Twist Tilt Rotor (VTTR) Blades," *Proceedings of AIAA/ASME/ASCE/AHS/ASC 43rd Structures, Structural Dynamics, and Materials Conference and 10th Adaptive Structures Forum*, AIAA, Reston, VA, 2002.

[169]Thomson, P., Balas, G. J., and Leo, P. H., "Pseudoelastic Hystersis of Shape Memory Wires for Passive Structural Damping: Theory and Experiments," *Society of Photo-Optical Instrumentation Engineers*, Vol. 1917, Society of Photo-Optical Instrumentation Engineers (International Society for Optical Engineering), Bellingham, WA, 1993.

[170]Wolons, D., Gandhi, F., and Malovrh, B., "Experimental Investigation of the Pseudoelastic Hysteresis Damping Characteristics of Shape Memory Alloy Wires," *Journal of Intelligent Material Systems and Structures*, Vol. 9, No. 2, 1998, pp. 116–126.

[171]Malovrh, B., and Gandhi, F., "Mechanism-Based Phenomenological Models for the Pseudoelastic Hystersis Behavior of Shape Memory Alloys," *Journal of Intelligent Material Systems and Structures*, Vol. 12, No. 1, 2001, pp. 21–30.

[172]Lammering, R., and Schmidt, I., "Experimental Investigations on the Damping Capacity of NiTi Components," *Smart Materials and Structures*, Vol. 10, No. 5, 2001, pp. 853–859.

[173]Ju, D. Y., and Shimamoto, A., "Damping Property of Expoxy Matrix Composite Beams with Embedded Shape Memory Alloy Fibers," *Journal of Intelligent Material Systems and Structures*, Vol. 10, No. 7, 1999, pp. 514–520.

[174]Rogers, C. A., and Barker, D. K., "Experimental Studies of Active Strain Energy Tuning of Adaptive Composites," *Proceedings of AIAA/ASME/ASCE/AHS/ASC 31st Structures, Structural Dynamics, and Materials Conference*, AIAA, Washington, DC, 1990.

[175]Baz, A., Imam, K., and McCoy, J., "Active Vibration Control of Flexible Beams Using Shape Memory Actuators," *Journal of Sound and Vibration*, Vol. 140, No. 3, 1990, pp. 437–456.

[176]Baz, A., Ro, J., Mutua, M., and Gilheany, J., "Active Buckling Control of Nitinol-Reinforced Composite Beams," *Conference on Active Material and Adaptive Structures*, Society of Photo-Optical Instrumentation Engineers (International Society for Optical Engineering), Bellingham, WA, 1991, pp. 167–176.

[177]Brinson, L. C., Bekker, A., and Huang, M., "Deformation of Shape Memory Alloys due to Thermo-Induced Tramsformation," *Journal of Intelligent Material Systems and Structures*, Vol. 7, No. 1, 1996, pp. 97–107.

[178]Lagoudas, D. C., Moorthy, D., Quidwai, M. A., and Reddy, J. N., "Modeling of Thermomechnical Response of Active Laminates with SMA Strips Using Layerwise Finite Element Method," *Journal of Intelligent Material Systems and Structures*, Vol. 8, No. 6, 1997, pp. 476–488.

[179]Turner, T. L., "A New Thermoelastic Model for Analysis of Shape Memory Alloy Hybrid Composites," *Journal of Intelligent Material Systems and Structures*, Vol. 11, No. 5, 2000, pp. 382–394.

[180]Epps, J., and Chandra, R., "Shape Memory Actuation for Active Tuning of Composite Beams," Society of Photo-Optical Instrumentation Engineers (International Society for Optical Engineering), Bellingham, WA, Feb.–March 1995.

[181]Furuya, Y., "Design and Material Evaluation of Shape Memory Composites," *Journal of Intelligent Material Systems and Structures*, Vol. 7, No. 2, 1996, pp. 321–330.

[182]Birman, V., "Micromechanics of Composites with Shape Memory Alloy Fibers in Uniform Thermal Fields," *AIAA Journal*, Vol. 34, No. 9, 1996, pp. 1905–1912.

[183]Butler, J. L., "Application Manual for the Design of ETREMA Terfenol-D Magnetostrictive Transducers," ETREMA Products, Edge Technologies, Ames, IA, 1988.

[184]Butler, J. L., Butler, S. C., and Clark, A. E., "Unidirectional Magnetostrictive Piezoelectric Hybrid Transducer," *Journal of the Acoustical Society of America*, Vol. 88, No. 1, 1990, pp. 7–11.

[185]Engdahl, G., and Svensson, L., "Simulation of the Magnetostrictive Performance of Terfenol-D in Mechanical Devices," *Journal of Applied Physics*, Vol. 63, No. 8, 1988, pp. 3924–3926.

[186]Kvarnsjo, L., and Engdahl, G., "Nonlinear 2-D Transient Modeling of Terfenol-D Rods," *IEEE Transactions on Magnetics*, Vol. 27, No. 6, 1991, pp. 5349–5351.

[187]Claeyssen, F., Bossut, R., and Boucher, D., "Modeling and Characterization of Magnetostrictive Coupling," *Power Transducers for Sonics and Ultrasonics*, Springer-Verlag, 1991, pp. 132–151.

[188]Carman, G. P., and Mitrovic, M., "Nonlinear Constitutive Relations for Magnetostrictive Materials with Applications to 1-D Problems," *Journal of Intelligent Material Systems and Structures*, Vol. 6, No. 5, 1995, pp. 673–683.

[189]Hom, C., and Shankar, N., "A Finite Element Method for Electrostrictive Ceramic Devices," *International Journal for Solids and Structures*, Vol. 33, No. 12, 1995, pp. 1757–1779.

[190]Duenas, T. A., Hsu, L., and Carman, G. P., "Magnetostrictive Composite Material Systems Analytical/Experimental," Symp. Advances Smart Materials-Fundamentals Applications, Materials Research Society Symposium Proceeding 459, 1996.

[191]Dapino, M. J., Smith, R., Faidley, L. E., and Flatau, A. B., "A Coupled Structural Magnetic Strain and Stress Model for Magnetostrictive Transducers," *Journal of Intelligent Material Systems and Structures*, Vol. 11, No. 2, 2000, pp. 135–152.

[192]Anjanappa, M., and Bi, J., "A Theoretical and Experiment Study of Magnetostrictive Mini-Actuators," *Smart Materials and Structures*, Vol. 3, No. 1, 1994, pp. 83–91.

[193]Anjanapp, M., and Wu, Y., "Magnetostrictive Particulate Actuators Configuration, Modeling and Characterization," *Smart Structures and Materials*, Vol. 6, No. 3, 1997, pp. 393–402.

[194]Wu, Y., and Anjanappa, A., "Modeling of Embedded Magnetostrictive Particualte Actuators," *Proceedings of the 1996 Society of Photo-Optical Instrumentation Engineers Conference on Smart Structures and Materials*, Vol. 2717, Society of Photo-Optical Instrumentation Engineers (International Society for Optical Engineering), Bellingham, WA, 1996.

[195]Krishanmurthy, A. V., Anjanappa, M., and Wu, Y., "Use of Magnetostrictive Particle Actuators for Vibration Attenuation of Flexible Beams," *Journal of Sound and Vibration*, Vol. 206, No. 2, 1997, pp. 133–149.

[196]Flatau, A. B., Dapino, M. J., and Calkins, F. T., "Magnetostrictive Composites," *Comprehensive Composite Materials Handbook*, edited by A. Kelly and C. Zweben, Vol. 5, Elsevier, 2000, pp. 563–574.

[197]Kannan, K. S., "Galerkin Finite Element Scheme for Magnetostrictive Structures and Composites," Ph.D. Dissertation, Dept. of Mechanical Engineering, Univ. of Maryland, College Park, June 1997.

[198]Pradhan, S. C., Ng, T. Y., Lam, K. Y., and Reddy, J. N., "Control of Laminated Composite Plates Using Magnetostrictive Layers," *Smart Materials and Structures*, Vol. 10, No. 4, 2001, pp. 657–667.

[199]Calkins, F. T., Flatau, A. B., and Dapino, M. J., "Overview of Magnetostrictive Sensor Technology," *Proceedings of AIAA/ASME/ASCE/AHS/ASC Structures, Structural Dynamics, and Materials Conference*, AIAA, Reston, VA, 1999.

[200]Dapino, M. J., Calkins, F. T., and Flatau, A. B., "Magnetostrictive Devices," *Wiley Encyclopedia of Electrical and Electronics Engineering*, edited by J. G. Webster, Wiley, 1999, pp. 278–305.

[201]Flatau, A. B., Dapino, M. J., and Calkins, F. T., "High Bandwidth Tunability in a Smart Vibration Absorber," *Journal of Intelligent Material Systems and Structures*, Vol. 11, No. 12, 2000, pp. 923–929.

[202]Pratt, J., and Flatau, A. B., "Development and Analysis of a Self-Sensing Magnetostrictive Actuator Design," *Journal of Intelligent Material Systems and Structures*, Vol. 6, No. 5, 1995, pp. 639–648.

[203]Kellogg, R., and Flatau, A. B., "Experimental Investigation of Terfenol-D's Elastic Modulus," *Proceedings of the Society of Photo-Optical Instrumentation Engineers' Conference on Smart Structures and Materials*, Vol. 4327, Society of Photo-Optical Instrumentation Engineers (International Society for Optical Engineering), Bellingham, WA, 2001, pp. 541–549.

[204]Pratt, J. R., Oueini, S. C., and Nayfeh, A. H., "Terfenol-D Nonlinear Vibration Absorber," *Journal of Intelligent Material Systems and Structures*, Vol. 10, No. 1, 1999, pp. 29–35.

[205]Balckwood, G. H., and Ealey, M. A., "Electrostrictive Behavior in Lead Magnesium Niobate (PMN) Actuators, Part I: Material Properties," *Smart Materials and Structures*, Vol. 2, No. 2, 1993, pp. 124–133.

[206]Uchino, K., "Electrostrictive Actuators," *Ceramic Bulletin*, Vol. 65, 1986, pp. 647–652.

[207]Damjanovic, D., and Newnham, R. E., "Electrostrictive and Piezoelectric Materials for Actuator Applications," *Journal of Intelligent Material Systems and Structures*, Vol. 3, No. 2, 1992, pp. 190–208.

[208]Pablo, F., and Petitjean, B., "Characterization of 0.9PMN-0.1PT Patches of Active Vibration Control of Plate Host Structures," *Journal of Intelligent Material Systems and Structures*, Vol. 11, No. 11, 2000, pp. 857–867.

[209]Fripp, M., and Hagood, N., "Distributed Structural Actuation with Electrostrictives," *Journal of Sound and Vibration*, Vol. 203, No. 1, 1997, pp. 11–40.

[210]Fripp, M., and Hagood, N., "Comparison of Electrostrictive and Piezoceramic Actuators for Vibration Suppression," *Proceedings of the 1995 Society of Photo-Optical Instrumentation Engineers' Conference on Smart Structures and Materials*, Society of Photo-Optical Instrumentation Engineers (International Society for Optical Engineering), Bellingham, WA, 1995.

[211]Hom, C. L., and Shankar, N., "A Fully Coupled Constitutive Model for Electrostrictive Ceramic Materials," *Journal of Intelligent Material Systems and Structures*, Vol. 5, No. 6, 1994, pp. 795–801.

[212]Hom, C. L., and Shankar, N., "A Constitutive Model for Relaxor Ferroelectrics," *Proceedings of the 1999 Society of Photo-Optical Instrumentation Engineers' North American Symposium on Smart Structures and Materials*, Society of Photo-Optical Instrumentation Engineers (International Society for Optical Engineering), Bellingham, WA, 1999.

[213]Piquette, J. C., and Forsythe, S. E., "A Nonlinear Material Model of Lead Magnesium Niobate (PMN)," *Journal of the Acoustical Society of America*, Vol. 101, No. 1, 1997, pp. 289–296.

[214]Wada, B. K., Fanson, J. L., and Crawley, E. F., "Adaptive Structures," *Journal of Intelligent Material Systems and Structures*, Vol. 1, No. 2, 1990, pp. 157–174.

[215]Lin, C. Y., Crawley, E. F., and Heeg, J., "Open- and Closed-Loop Results of a Strain-Actuated Active Aeroelastic Wing," *Journal of Aircraft*, Vol. 33, No. 5, 1996, pp. 987–994.

[216]Kudva, J., Appa, K., Martin, C., Jardine, P., and Sendeckji, G., "Design, Fabrication and Testing of the DARPA/WL 'Smart Wing' Wind Tunnel Model," AIAA Paper 97-1198, April 1997.

[217]Kudva, J., Martin, C. A., Scherer, L. B., Jardine, A. P., McGovan, A. R., Lake, R. C., Sendeckji, G., and Sanders, B., "Overview of the DARPA/AFRL/NASA Smart Wing Program," *Proceedings of the 1999 Society of Photo-Optical Instrumentation Engineers' North American Symposium on Smart Structures and Materials*, Vol. 3674, Society of Photo-Optical Instrumentation Engineers (International Society for Optical Engineering), Bellingham, WA, 1999, pp. 230–248.

[218]Becker, J., and Schroder, W., "Advanced Aircraft Structures Program: An Overview," *Proceedings of the 1999 Society of Photo-Optical Instrumentation Engineers' North American Symposium on Smart Structures and Materials*, Vol. 3674, Society of Photo-Optical Instrumentation Engineers (International Society for Optical Engineering), Bellingham, WA, 1999, pp. 2–12.

[219]Durr, J. K., Herold-Schmidt, U., and Zaglauer, W., "On the Integration of Piezoceramic Actuators in Composite Structures for Aerospace Applications," *Journal of Intelligent Material Systems and Structures*, Vol. 10, No. 11, 1999, pp. 880–889.

[220]Ehlers, S. M., and Weisshaar, T. A., "Static Aeroelastic Control of an Adaptive Lifting Surface," *Journal of Aircraft*, Vol. 30, No. 4, 1993, pp. 534–540.

[221]Lazarus, K. B., Crawley, E. F., and Bohlmann, J. D., "Static Aeroelastic Control Using Strain Actuated Adaptive Structures," *Journal of Intelligent Material Systems and Structures*, Vol. 2, No. 3, 1991, pp. 386–410.

[222]Frampton, K. D., Clark, R. L., and Dowell, E. H., "Active Control of Panel Flutter with Piezoelectric Transducers," *Journal of Aircraft*, Vol. 33, No. 4, 1996, pp. 768–774.

[223]Bein, T., Hanselka, H., and Breitbach, E., "An Adaptive Spoiler to Control the Transonic Shock," *Smart Materials and Structures*, Vol. 9, No. 2, 2000, pp. 141–148.

[224]Fuller, C. R., Hansen, C. H., and Snyder, S. D., "Experiments on Active Control of Sound Radiation from a Panel Using a Piezoceramic Actuator," *Journal of the Acoustical Society of America*, Vol. 91, No. 6, 1992, pp. 3313–3320.

[225]Hooker, M. W., "Properties and Performance of RAINBOW Piezoelectric Actuator Stacks," *Proceedings of the Society of Photo-Optical Instrumentation Engineers' 4th Annual Symposium on Smart Structures and Materials, Industrial and Commercial Applications*, 1997, pp. 413-420.

[226]Li, G., Furman, E., and Haertling, G. H., "Fabrication and Properties PSZT Antiferroelectric Rainbow Actuators," *Ferroelectrics*, Vol. 188, No. 1–4, 1996, pp. 223–236.

[227]Li, G., Furman, E., and Haertling, G. H., "Finite Element Analysis of Rainbow Ceramics," *Journal of Intelligent Material Systems and Structures*, Vol. 8, No. 5, 1997, pp. 434–443.

[228]Mossi, K. M., and Bishop, R. P., "Characterization of Different Types of High-Performance THUNDER Actuators," *Proceedings of the Society of Photo-Optical Instrumentation Engineers' 6th Annual Symposium on Smart Structures and Materials, Smart Materials Technologies Conference*, Vol. 3675, Society of Photo-Optical Instrumentation Engineers (International Society for Optical Engineering), Bellingham, WA, 1999, pp. 43–52.

[229]Onitsuka, K., Dogan, A., Tressler, J. F., Xu, Q., Yoshikawa, S., and Newnham, R. E., "Metal-Ceramic Composite Transducer, The Moonie," *Journal of Intelligent Material Systems and Structures*, Vol. 6, No. 4, 1995, pp. 447–455.

[230]Moskalik, A., and Brei, D., "Parametric Investigation of the Deflection Performance of Serial Piezoelectric C-Block Acutaors," *Journal of Intelligent Material Systems and Structures*, Vol. 9, No. 3, 1998, pp. 223–231.

[231]Moskalik, A., and Brei, D., "Quasi-Static Behavior of Individual C-Block Piezoelectric Acuators," *Journal of Intelligent Material Systems and Structures*, Vol. 8, No. 7, 1997, pp. 571–587.

[232]Lee, T., "Design of High Displacement Smart Trailing Edge Flap Actuator Incorporating Dual-Stage Mechanical Stroke Amplifiers for Rotors," Ph.D. Dissertation, Dept. of Aerospace Engineering, Univ. of Maryland, College Park, Dec. 1999.

[233]Giurgiutiu, V., Rogers, C. A., and Chaudhary, Z., "Energy-Based Comparison of Solid State Induced-Strain Actuators," *Journal of Intelligent Material Systems and Structures*, Vol. 7, No. 1, 1996, pp. 4–14.

[234]Giurgiutiu, V., and Rogers, C. A., "Large Amplitude Rotary Induced-Strain (LARIS)," *Journal of Intelligent Material Systems and Structures*, Vol. 8, No. 1, 1997, pp. 41–50.

[235]Mitrovic, M., Carman, G. P., and Straub, F. K., "Electromechanical Characterization of Piezoelectric Stack Actuators," *Proceedings of the Society of Photo-Optical Instrumentation Engineers' 6th Annual Symposium on Smart Structures and Materials, Smart Materials Technologies Conference*, Vol. 3668, Society of Photo-Optical Instrumentation Engineers (International Society for Optical Engineering), Bellingham, WA, 1999, p. 589.

[236]Giurgiutiu, V., and Rogers, C. A., "Stiffness Issues in the Design of ISA Displacement Amplification Devices: Case Study of a Hydraulic Displacement Amplifier," *Proceedings of the Society of Photo-Optical Instrumentation Engineers' 2nd Annual Symposium on Smart Structures and Materials, Smart Materials Conference*, Vol. 2443, Society of Photo-Optical Instrumentation Engineers (International Society for Optical Engineering), Bellingham, WA, 1995.

[237]Garcia-Bonito, J., Brennan, M. J., Elliott, S. J., and Pinnington, R. J., "A Novel High-Displacement Piezoelectric Actuator for Active Vibration Control," *Smart Materials and Structures*, Vol. 7, No. 1, 1998, pp. 31–42.

[238]Lee, T., and Chopra, I., "Design of Peizostack-Driven Trailing-Edge Flap Actuator for Helicopter Rotors," *Smart Materials and Structures*, Vol. 10, No. 1, 2001, pp. 15–24.

[239]Prechtl, E. F., and Hall, S. R., "Design of a High Energy Discrete Servo-Flap Actuator for a Helicopter Rotor Control," *Proceedings of the 1997 Society of Photo-Optical Instrumentation Engineers' North American Symposium on Smart Structures and Materials*, Vol. 3041, Society of Photo-Optical Instrumentation Engineers (International Society for Optical Engineering), Bellingham, WA, 1997, pp. 158–182.

[240]Straub, F. K., "Active Flap Control for Vibration Reduction and Performance Improvement," *Proceedings of the 54th Annual Forum*, Vol. 1, American Helicopter Society, Alexandria, VA, 1998.

[241]Fenn, R. C., Downer, J. R., Bushko, D. A., Gohalekar, V., and Ham, N. D., "Terfenol-D Driven Flaps for Helicopter Vibration Reduction," *Smart Materials and Structures*, Vol. 5, No. 1, 1996, pp. 49–57.

[242]Janker, P., Kloppel, V., Hermle, F., Lorkowski, T., Storm, S., Christmann, M., and Wettemann, M., "Development and Evaluation of a Hybrid Piezoelectric Actuator for Advanced Flap Control Technology," 25th European Rotorcraft Forum, Rome, Sept. 1999.

[243]Xu, W., and King, T., "Flexural Hinges for Piezoelectric Displacement Amplifiers: Flexibility, Accuracy, and Stress Concentration," *Precision Engineering*, Vol. 19, No. 1, 1996, pp. 4–10.

[244]Prechtl, E. F., and Hall, S. R., "Design of a High Efficiency, Large Stroke, Electromechanical Actuator," *Smart Materials and Structures*, Vol. 8, No. 1, 1999, pp. 13–30.

[245]Paine, J. S. N., and Chaudhry, Z., "The Impact of Amplification on Energy Efficiency and Energy Density of Induced Strain Actuators," *Proceedings of ASME Aerospace Division*, AD-Vol. 52, American Society of Mechanical Engineers, 1996, pp. 511–516.

[246]Lee, T., and Chopra, I., "Design Issues of a High-Stroke, On-Blade Piezostack Actuator for Helicopter Rotor with Trailing-Edge Flaps," *Journal of Intelligent Material Systems and Structures*, Vol. 11, No. 5, 2000, pp. 328–342.

[247]Frecker, M., and Canfied, S., "Optimal Design and Experimental Validation of Compliant Mechanical Amplifiers for Piezoceramic Stack Actuators," *Journal of Intelligent Material Systems and Structures*, Vol. 11, No. 5, 2000, pp. 360–369.

[248]Frecker, M., Ananthsuresh, G. K., Nishiwaki, S., Kikuchi, N., and Kota, S., "Topological Synthesis of Complaint Mechanisms Using Multi-Criteria Optimization," *Journal of Mechanical Design*, Vol. 119, No. 2, 1997, pp. 238–245.

[249]Edinger, B., Frecker, M., and Gardner, J., "Dynamic Modeling of an Innovative Piezoelectric Actuator for Minimally Invasive Surgery," *Journal of Intelligent Material Systems and Structures*, Vol. 11, No. 10, 2000, pp. 765–770.

[250]Bothwell, C. M., Chandra, R., and Chopra, I., "Torsional Actuation with Extension-Torsional Composite Coupling and Magnetostrictive Actuators," *AIAA Journal*, Vol. 33, No. 4, 1995, pp. 723–729.

[251]Bernhard, A. P. F., and Chopra, I., "Hover Testing of Active Rotor Blade-Tips Using a Piezo-Induced Bending-Torsion Coupled Beams," *Journal of Intelligent Material Systems and Structures*, Vol. 9, No. 12, 1998, pp. 963–974.

[252]Glazounov, A. E., Zhang, Q. M., and Kim, C., "New Torsional Actuator Based on Shear Piezoelectric Response," *Proceedings of the Society of Photo-Optical Instrumentation Engineers' 5th Annual Symposium on Smart Structures and Materials, Smart Materials Conference*, Vol. 3044, Society of Photo-Optical Instrumentation Engineers (International Society for Optical Engineering), Bellingham, WA, 1998.

[253]Centolanza, L. R., Smith, E. C., and Morris, A., "Induced Shear Piezoelectric Actuators for Rotor Blade Trailing Edge Flaps and Active Tips," AIAA Paper 2001-1559, April 2001.

[254]Bent, A. A., and Hagood, N. W., "Anisotropic Actuation with Piezoelectric Fiber Composites," *Journal of Intelligent Material Systems and Structures*, Vol. 6, No. 3, 1995, pp. 338–349.

[255]Bent, A. A., and Hagood, N. W., "Piezoelectric Fiber Composites with Interdigitated Electrodes," *Journal of Intelligent Material Systems and Structures*, Vol. 8, No. 11, 1997, pp. 903–919.

[256]Hagood, N. W., and Pizzochero, A., "Residual Stiffness and Actuation Properties of Piezoelectric Composites: Theory and Experiment," *Journal of Intelligent Material Systems and Structures*, Vol. 8, No. 9, 1997, pp. 724–737.

[257]Rogers, J. P., and Hagood, N. W., "Preliminary Mach-Scale Hover Testing of an Integral Twist-Actuated Rotor Blade," *Proceedings of the 1997 Society of Photo-Optical Instrumentation Engineers' North American Symposium on Smart Structures and Materials*, Vol. 3041, Society of Photo-Optical Instrumentation Engineers (International Society for Optical Engineering), Bellingham, WA, 1997.

[258]Rogers, J. P., and Hagood, N. W., "Design and Manufacture of an Integral Twist-Actuated Rotor Blade," *Proceedings of the 38th AIAA/ASME/ASCE/AHS/ASC Structures, Structural Dynamics, and Materials Conference and Adaptive Structures Forum*, AIAA, Reston, VA, 1997.

[259]Derham, R. C., and Hagood, N. W., "Rotor Design Using Smart Materials to Actively Twist Blades," *Proceedings of the 52nd Annual Forum*, Vol. 2, American Helicopter Society, Alexandria, VA, 1996, pp. 1242–1252.

[260]Wilkie, K. W., Wilbur, M. L., Mirick, P. H., Cesnik, C. E. S., and Shin, S. J., "Aeroelastic Analysis of the NASA/Army/MIT Active Twist Rotor," *Proceedings of the 55th Annual Forum*, Vol. 2, American Helicopter Society, Alexandria, VA, 1999, pp. 533–544.

[261]Wikkie, W. K., Bryant, R. G., High, J. W., Fox, R. L., Hellbaum, R. F., Jalink, A., Little, B. D., and Mirick, P. H., "Low-Cost Piezocomposite Actuator for Structural Control Application," *Proceedings of the 2000 Society of Photo-Optical Instrumentation Engineers' North American Symposium on Smart Structures and Materials*, Vol. 3985, Society of Photo-Optical Instrumentation Engineers (International Society for Optical Engineering), Bellingham, WA, 2000.

[262]Pokines, B. J., and Garcia, E., "A Smart Material Microamplification Mechanism Fabricated Using LIGA," *Smart Materials and Structures*, Vol. 7, No. 1, 1998, pp. 105–112.

[263]Mauck, L. D., and Lynch, C. S., "Piezoelectric Hydraulic Pump Development," *Journal of Intelligent Material Systems and Structures*, Vol. 11, No. 10, 2000, pp. 758–764.

[264]Nasser, K., and Leo, D. J., "Efficiency of Frequency-Rectified Peizohydraulic and Piezopneumatic Actuation," *Journal of Intelligent Material Systems and Structures*, Vol. 11, No. 10, 2000, pp. 798–810.

[265]Roberts, D., Hagood, N., Carretero, H., Li, H., Mlcak, R., and Su, Y., "Piezoelectrically Driven Hydraulic Amplification Microvalve for High Pressure High Frequency Applications," *Proceedings of the 2000 Society of Photo-Optical Instrumentation Engineers' North American Symposium on Smart Structures and Materials*, Vol. 4327, Society of Photo-Optical Instrumentation Engineers (International Society for Optical Engineering), Bellingham, WA, 2000, pp. 366–380.

[266]Sirohi, J., and Chopra, I., "Development of a Compact Hybrid Actuator," *Proceedings of the 2001 Society of Photo-Optical Instrumentation Engineers' North American Symposium on Smart Structures and Materials, Smart Materials Technologies Conference*, Vol. 4327, Society of Photo-Optical Instrumentation Engineers (International Society for Optical Engineering), Bellingham, WA, 2001, pp. 401–412.

[267]Sirohi, J., and Chopra, I., "Design and Testing of a High-Pumping Frequency Piezoelectric-Hydraulic hybrid Actuator," *Proceedings of the 2002 Society of Photo-Optical Instrumentation Engineers' North American Symposium on Smart Structures and Materials*, Vol. 4701, Society of Photo-Optical Instrumentation Engineers (International Society for Optical Engineering), Bellingham, WA, 2002, pp. 552–569.

[268]Sirohi, J., and Chopra, I., "Actuator Power Reduction Using Tuned L-C Oscillator Circuits," *Journal of Intelligent Material Systems and Structures*, Vol. 12, No. 12, 2000, pp. 867–878.

[269]Clingman, J. D., "Drive Electronics for Large Piezoactuators," *Proceedings of the Society of Photo-Optical Instrumentation Engineers' 4th Annual Symposium on Smart Structures and Materials, Industrial Applications Conference*, Vol. 3044, Society of Photo-Optical Instrumentation Engineers (International Society for Optical Engineering), Bellingham, WA, 1997, pp. 459–467.

[270]Main, J. A., Garcia, E., and Newton, D. V., "Precision Position Control of Piezoelectric Actuators Using Charge Feedback," *Journal of Guidance, Control, and Dynamics*, Vol. 18, No. 5, 1995, pp. 1068–1073.

[271]Chandrasekaran, S., Linder, D. K., and Smith, R. C., "Optimized Design of Switching Amplifiers for Piezoelectric Actuators," *Journal of Intelligent Material Systems and Structures*, Vol. 11, No. 11, 2000, pp. 887–901.

[272]Koratkar, N. A., and Chopra, I., "Development of a Mach-Scaled Model with Piezoelectric Bender Actuated Trailing-Edge Flaps for Helicopter Individual Blade Control (IBC)," *AIAA Journal*, Vol. 38, No. 7, 2000, pp. 1113–1124.

[273]Koratkar, N. A., and Chopra, I., "Wind Tunnel Testing of a Mach-Scaled Rotor Model with Trailing-Edge Flaps," *Smart Materials and Structures*, Vol. 10, No. 1, 2001, pp. 1–14.

[274]Koratkar, N. A., and Chopra, I., "Wind Tunnel Testing of a Mach-Scaled Rotor Model with Trailing-Edge Flaps," *Proceedings of the 57th Annual Forum of the American Helicopter Society*, Vol. 2, American Helicopter Society, Alexandria, VA, 2001, pp. 1069–1099.

[275]Fulton, M., and Ormiston, R. A., "Small Scale Rotor Experiments with On-Blade Elevons to Reduce Blade Vibratory Loads in Forward Flight," *Journal of the American Helicopter Society*, Vol. 46, No. 2, 2001, pp. 96–106.

[276]Lee, T., and Chopra, I., "Wind Tunnel Test of Blade Sections with Piezoelectric Trailing-Edge Flap Mechanism," *Proceedings of the 57th Annual Forum of the American Helicopter Society*, Vol. 2, American Helicopter Society, Alexandria, VA, 2001, pp. 1912–1923.

[277]Straub, F. K., Ngo, H. T., Anand, V., and Domzalski, D. B., "Development of a Piezoelectric Actuator for Trailing-Edge Flap Control for Full Scale Rotor System," *Smart Materials and Structures*, Vol. 10, No. 1, 2001, pp. 25–34.

[278]Hall, S. R., and Prechtl, E. F., "Preliminary Testing of a Mach-Scaled Active Rotor Blade with a Trailing Edge Servo-Flap," *Proceedings of the 1999 Society of Photo-Optical Instrumentation Engineers' North American Symposium on Smart Structures and Materials*, Vol. 3668, Society of Photo-Optical Instrumentation Engineers (International Society for Optical Engineering), Bellingham, WA, 1999, pp. 14–21.

[279]Bernhard, A. P. F., and Chopra, I., "Trailing Edge Flap Activated by a Piezo-Induced Bending-Torsion Coupled Beam," *Journal of the American Helicopter Society*, Vol. 44, No. 1, 1999, pp. 3–15.

[280]Bernhard, A. P. F., and Chopra, I., "Analysis of a Bending-Torsion Coupled Actuator for a Smart Rotor with Active Blade Tips," *Smart Materials and Structures*, Vol. 10, No. 1, 2001, pp. 35–52.

[281]Bernhard, A. P. F., and Chopra, I., "Hover Test of an Active-Twist, Mach-Scale Rotor Using a Piezo-Induced Bending-Torsion Actuator Beam," National Specialists Meeting, American Helicopter Society, Alexandria, VA, Oct. 2000.

[282]Chen, P. C., and Chopra, I., "Wind Tunnel Test of a Smart Rotor with Individual Blade Twist Control," *Journal of Intelligent Material Systems and Structures*, Vol. 8, No. 5, 1997, pp. 414–425.

[283]Chen, P. C., and Chopra, I., "Hover Testing of Smart Rotor with Induced-Strain Actuation of Blade Twist," *AIAA Journal*, Vol. 35, No. 1, 1997, pp. 6–16.

[284]Cesnik, C. E. S., Shin, S. J., and Wilbur, M. L., "Dynamic Response of Active Twist Rotor Blades," *Smart Materials and Structures*, Vol. 10, No. 1, 2001, pp. 62–76.

[285]Shin, S. J., Cesnik, C. E. S., and Hall, S. R., "Control of Integral Twist-Actuated Helicopter Blades for vibration Reduction," *Proceedings of the 58th American Helicopter Society Annual Forum*, Vol. 2, American Helicopter Society, Alexandria, VA, 2002, pp. 2122–2134.

[286]Epps, J. J., and Chopra, I., "In-Flight Tracking of Helicopter Rotor Blades Using Shape Memory Alloy Actuators,"*Proceedings of the 56th American Helicopter Society Annual Forum*, Vol. 1, American Helicopter Society, Alexandria, VA, 2000, pp. 328–343.

[287]Epps, J. J., and Chopra, I., "In-Flight Tracking of Helicopter Rotor Blades Using Shape Memory Alloy Actuators," *Smart Materials and Structures*, Vol. 10, No. 1, 2001, pp. 104–111.

[288]Singh, K., and Chopra, I., "Design of an Improved Shape Memory Alloy Actuator for Rotor Blade Tracking," *Proceedings of the 2002 Society of Photo-Optical Instrumentation Engineers' North American Symposium on Smart Structures and Materials*, Vol. 4701, Society of Photo-Optical Instrumentation Engineers (International Society for Optical Engineering), Bellingham, WA, 2002, pp. 244–266.

[289]Chen, P. C., Baeder, J. D., Evans, R. A. D., and Niemczuk, J., "Blade-Vortex Interaction Noise Reduction with Active Twist Smart Rotor Technology," *Smart Materials and Structures*, Vol. 10, No. 1, 2001, pp. 77–85.

[290]Sampath, A., and Balachandran, B., "Active Control of Multiple Tones in an Enclosure," *Journal of the Acoustical Society of America*, Vol. 106, No. 1, 1999, pp. 211–225.

[291]Shen, J., and Chopra, I., "Actuation Requirements for a Swashplateless Helicopter Control System with Trailing-Edge Flaps," *Proceedings of the 43rd AIAA/ASME/ASCE/AHS/ASC Structures, Structural Dynamics and Materials Conference and Adaptive Structures Forum*, AIAA, Reston, VA, 2002.

[292]Shen, J., and Chopra, I., "A Parametric Design Study for a Swashplateless Helicopter Rotor with Trailing-Edge Flaps," *Proceedings of the 58th American Helicopter Society Annual Forum*, Vol. 2, American Helicopter Society, Alexandria, VA, 2002, pp. 2134–2148.

[293]Kube, R., and Kloppel, V., "On the Role of Prediction Tools for Adaptive Rotor System Developments," *Smart Materials and Structures*, Vol. 10, No. 1, 2001, pp. 137–144.

[294]Pelinescu, I., and Balachandran, B., "Analytical Study of Active Control of Wave Transmission Through Cylindrical Struts," *Smart Materials and Structures*, Vol. 10, No. 1, 2001, pp. 121–136.

[295]Mahapatra, D. R., Gopalkrishnan, S., and Balachandran, B., "Active Feedback Control of Multiple Waves in Helicopter Gearbox Support Struts," *Smart Materials and Structures*, Vol. 10, No. 5, 2001, pp. 1046–1058.

[296]Kamath, G. M., Wereley, N. W., and Jolly, M. R., "Characterization of Magnetorheological Helicopter Lag Dampers," *Journal of the American Helicopter Society*, Vol. 45, No. 4, 1999, pp. 234–248.

[297]Kim, S. J., and Yun, C. Y., "Performance Comparison Between Piezoelectric and Elastomeric Lag Damper on Ground Resonance Stability of Helicopter," *Journal of Intelligent Material Systems and Structures*, Vol. 12, No. 4, 2001, pp. 215–222.

[298]Konstanzer, P., Grohmann, B., and Kroplin, B., "Decentralized Vibration Control and Coupled Aeroservoelastic Simulation of Helicopter Rotor Blades with Adaptive Airfoils," *Journal of Intelligent Material Systems and Structures*, Vol. 12, No. 4, 2001, pp. 209–214.

A. M. Baz
Associate Editor